Black Titanium Dioxide:
Synthesis, Characterization and Applications

Yiran Li

A Thesis submitted

in partial fulfillment of the requirements for the degree of

Master of Science in Chemistry

Department of Chemistry and Biomolecular Sciences

Faculty of Science

Abstract

The exploration and application of nanomaterials have been attracting researchers' attention in recent decades. Nanocatalysts, as one of the very important classes of nanomaterials, have been developed for several generations. Nanotechnology makes light be possibly utilized in catalysis rather than only heat and allows multifunctional parts to be assembled in one catalyst. The TiO_2 (as the representative of hetero-photocatalyst) and iron-based magnetic catalysts (as multifunctional catalyst) will be discussed in detail in this thesis.

The first chapter will introduce the background of catalysts and nanomaterials. TiO_2, especially black TiO_2, will be mainly discussed in the aspects of properties, synthesis, and applications. Another part of the chapter will talk about the separation-friendly catalyst – magnetic heterogenous catalysts' synthesis and applications.

Chapter 2 focuses on the synthetic route we used and the characterization of black TiO_2 catalysts and magnetic catalysts. Both anatase and rutile black TiO_2 catalysts were successfully prepared originally from Degussa P25 using the ethanol reduction method. The re-whitening treatment was also examined on both black TiO_2 catalysts. All catalysts were characterized and compared by diffuse reflectance (DR), powder X-ray diffraction (XRD), and X-ray photoelectron spectroscope (XPS). Tauc plot results show that black TiO_2 has smaller band gap than white TiO_2. XPS revealed the existence of surface -OH species and Ti^{3+} in black TiO_2. Furthermore, these two characterization techniques and XRD all proved that the blackening and re-whitening treatment does not change the crystalline phase of the catalysts, and the blackening treatment is reversible. For magnetic catalysts, we synthesized magnetic Fe_2O_3, Fe_2O_3@TiO_2, copper/iron oxide magnetic TiO_2, and black magnetic catalysts. Other than diffuse reflectance spectroscopy, Raman spectroscopy, scanning electron microscopy, and energy-dispersive X-ray elemental mapping analysis were used for determining the light-absorption properties, composition, and morphology of all synthesized magnetic catalysts. In addition, the magnetic separation was also achieved by simply applying an external magnetic field.

Chapter 3 will discuss and compare the decarboxylation reaction activities of pristine, black, and re-whited TiO_2 catalysts. The reactions were carried under the UV, blue, red, green, and white light irradiation. Unfortunately, the reaction was found only working under UV-light irradiation. The best solvent was dioxane which may be due to the proton affinity of the oxygen atom in dioxane molecule, which facilitates the deprotonation of the carboxylic acid. The optimal catalyst amount was found as 10 mg per 5 mL reaction mixture, and the kinetic study shows that the reaction is a pseudo-first order reaction. It is a pity that the performance of black TiO_2 catalysts is worse than the pristine and re-whitened TiO_2.

Chapter 4 will talk about the sol-gel synthesized magnetic catalysts. These catalysts were used for aldehyde-alkyne-amine (A^3) coupling reaction. The reaction was tested by light irradiating or traditional heating, but only heating can make the reaction proceed. Results also show that the coupling reaction requires copper to finish. The best solvent was found as toluene and the optimal reaction time is 6 hours at 120℃. Sadly, the reactivity of copper/iron oxide magnetic TiO_2 decreases a lot after three reaction cycles because of the copper leaching problem.

Acknowledgements and Contributions

Firstly, I want and need to say thank you to my mother. Without your selfless love and boundless support, I would not exist or reach this far. Thank you mom and I love you!

I also would like to sincerely express my deepest appreciation to my mentor and supervisor, Dr. Juan Tito Scaiano. He is not only an extraordinary scientist who has made countless contributions to chemistry and train many great chemists, but also like a grandpa who shows his generous love to all his students. He guided my path in chemistry and expanded my sight of research. What he taught and provided to me is beyond what kindest words can be expressed. It is really a great honor and privilege having the opportunity of studying and working in his group.

Dr. Bowen Wang always provided his valuable suggestions and kind support in both my research and personal life. Dr. Anabel Lanterna also helped me resolve many chemistry problems whenever I sought for help. I really appreciate everything you did for me. Thank you so much.

Lastly, I also want to thank my colleagues, friends, and anyone who helped me in the university and personal life. It is a such fortune having you in my life. I will always remember and cherish the priceless bonds we have formed.

Table of Contents

List of Figures

List of Tables

List of Abbreviations

1,4-Dicyanobenzene	DCB
Acetonitrile	MeCN
Aldehyde-alkyne-amine	A^3
Anatase TiO_2	a-Ti
Binding energy	BE
Black TiO_2	b-Ti
Black anatase TiO_2	ba-Ti
Black magnetic $CuO@Fe_2O_3@TiO_2$	b-mCuFeTi
Black magnetic Fe_2O_3	b-mFe
Black magnetic $Fe_2O_3@TiO_2$	b-mFeTi
Black rutile TiO_2	br-Ti
Density of states	DOS
Dichloromethane	DCM
Diffuse reflectance	DR
Energy-dispersive X-ray	EDS
Fourier transform infrared	FT-IR
Gas chromatography–mass spectrometry	GC-MS
High-resolution	HR
High performance liquid chromatography	HPLC
Highest occupied molecular orbital	HOMO
Light-emitting diodes	LED
Light-emitting diodes illuminator	LEDi
Localized surface plasmon resonance	LSPR
Magnetic nanoparticles	MNPs
Magnetic $CuO@Fe_2O_3@ TiO_2$	mCuFeTi
Magnetic Fe_2O_3	mFe
Magnetic $Fe_2O_3@ TiO_2$	mFeTi
Methyl orange	MO
Nano-contrast agent	CMR

Nuclear magnetic resonance	NMR
Phenanthrene	Phen
Polytetrafluoroethylene	PTFE
Red-green-blue	RGB
Re-whited anatase TiO_2	wa-Ti
Re-whited rutile TiO_2	wr-Ti
Rutile TiO_2	r-Ti
Scanning electron microscopy	SEM
Single electron transfer	SET
Spin orbit splitting	ΔBE
Tetraethylorthosilicate	TEOS
Tetrahydrocannabinol	THC
Tetrahydrofuran	THF
Transmission electron microscopy	TEM
Ultra-violet	UV
X-ray diffraction	XRD
X-ray photoelectron spectroscope	XPS

Chapter 1
Introduction

1.1 Catalyst

Catalysts, as substances that can speed up a chemical reaction by altering reaction to a more energetically favorable pathway, have been used by humankind since the dawn of civilization[1]. The scope of catalysis is massive. It is wildly used in a variety of industries such as foods, petroleum, and chemical production. Many biological processes like metabolism and photosynthesis also require catalysts to proceed.

Catalysts can traditionally be classified as homogeneous catalysts, heterogeneous catalysts, and enzymes. Enzymes are out of the scope of this dissertation and they will not be discussed further. Whether the catalysts work in the same or different phase from where the reactants are the criteria of differentiating homogeneous catalysts from heterogeneous catalysts (Figure 1.1 (a) and (b))[2]. Sometimes the mechanism of catalysis can be more complicated. Figure 1.1 (c) shows that heterogeneous catalysts might leach out during the reaction and catalyze the reaction in a homogeneous way. Similarly, the homogeneous catalysts sometimes can firstly crystallize and then do the catalysis in a heterogeneous way (d). The most complicated one is shown in Figure 1.1 (e), the active catalytic species that leach out from heterogeneous catalyst do the catalysis, and then deposit back to catalyst surface after the reaction.

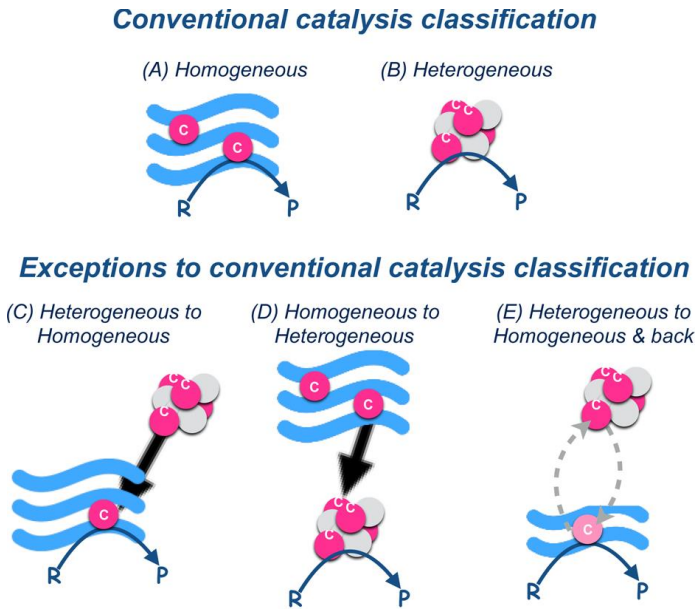

Figure 1.1. Five different catalysis classification[2]. Reprinted with permission from ref. 2.

Homogeneous catalysts have been studied for centuries and their mechanisms are well established. They are mostly atoms, ions, and molecules. For example, protons are used to catalyze broad types of chemical reactions such as Fischer-Speier esterification, aldol condensation, and halogenation of alkenes[3]. Some of the metal-ligand complex catalysts can even stereo-selectively catalyze reactions with high enantiomeric excess[4-7]. Homogeneous catalysts, as a solute in the reaction mixture, are able to interact with active species of the reaction relatively easily and freely, which facilitates the reaction control. But their disadvantages such as relatively low stability and time-consuming catalyst separation processes after reaction completion let scientists develop heterogeneous catalysts as alternative or even better catalysts.

Heterogeneous catalysts, in contrast, are normally solid, solid-supported, or insoluble matrices. MnO_2, one of the best catalysts for the degradation of hydrogen peroxide is an example. Since catalysts and reaction mixtures are in different phases, the post-reaction separation can be simply done by centrifugation, and then the catalysts are ready for the next reaction after cleaning or reactivation if needed[8, 9]. Those advantages of heterogeneous catalysts make them be used in fixed bed reactors, which are favored by the petroleum and chemical industries[10]. Despite of the good aspects, the regioselectivity and the mechanism study of heterogeneous catalysts are still a big challenge.

On the other hand, unlike the homogeneous catalysts, active components (sites) of heterogeneous catalysts locate on the surface of the catalyst. It means that the total surface area and specific surface area are crucial for the performance of a heterogeneous catalyst, which brings the hot topic, nanomaterials, into our consideration.

1.2 Nanomaterials

Nanomaterials are defined as the materials with sizes from 1 to 100 nanometer[11] (Figure 1.2). With the development of nanotechnology, the size range expands from few angstroms (clusters) to hundreds of nanometers, and the definition also applies to any material with any dimension fitting in the nano range (like nanowires)[12].

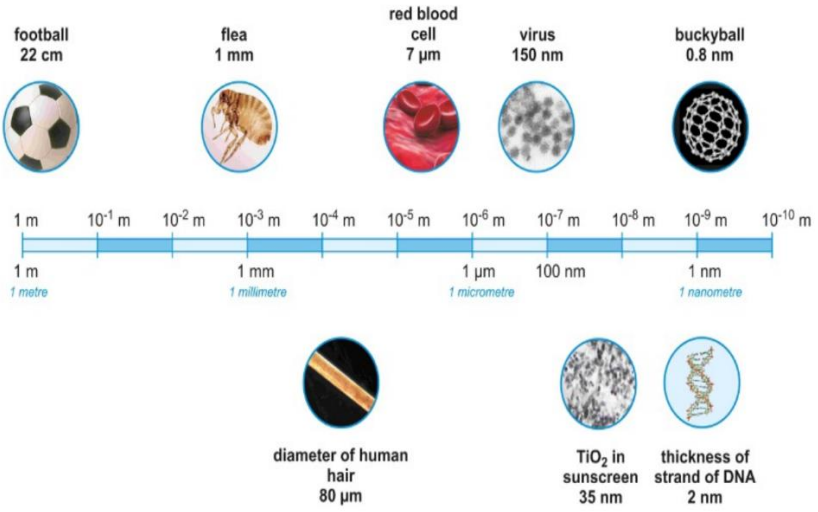

Figure 1.2. Different substances in the scale from 1 m to 1 Å. Reprinted with permission from The Essential Chemical Industry – online[13].

Nanomaterials have been used for hundreds of years without people realizing it. For example, medieval and renaissance pottery usually retains unique gold or bronze metallic glitter. This luster is caused by a metal film coated on the transparent surface of the glass window, which contains uniformly dispersed silver and copper nanoparticles. Similarly, colors in stained glasses used in cathedrals are from metals, metal salts, and metal oxides. The red color, particularly, is from colloidal gold nanoparticles (Figure 1.3). Nowadays, nanomaterials are used everywhere. One key material of making a new generation of rackets is graphene, which provides enhanced properties such as increasing around 30% in strength and decreasing up to 20% weight of rackets. Moreover, Gold

nanoparticles are also used in pregnancy test strips. Titanium dioxide nanoparticles are used to absorb ultra-violet (UV) light in sunscreens. And quantum dots are used to make high-resolution monitors.

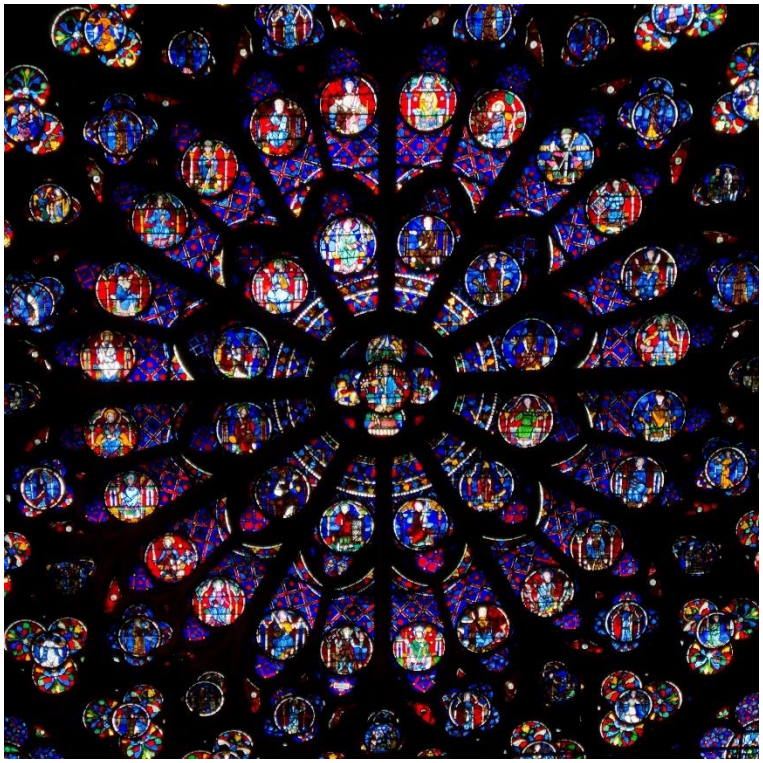

Figure 1.3. South Rose Window of Notre-Dame de Paris (Photographed by Carlos Delgado of Wikimedia, open license).

Talking about the differences between nanomaterials and bulk materials, the small sizes of nanomaterials make them have very different properties and usage from the bulk materials. Bulk materials have constant physical properties regardless of their sizes and shapes, but at the nanoscale, size- and shape-dependent properties are often observed. The color of colloidal silver nanoparticles can be yellow, orange, pink or green depending on the shape and size, which can be explained by localized surface plasmon resonance (LSPR)[14-16]. LSPR is out of the scope of this dissertation so it will not be discussed any further. Apart from color, the specific surface area of nanomaterials is significantly larger compared to the corresponding bulk materials. As illustrated in Figure 1.4[17], for a 1 cm^3 cube, surface area increases 10 folds after it is cut into all 1 mm^3 cubes. What is more, in 1 nm^3 cubes, the surface area rockets 10 million-fold. Moreover, as the decrease in size, the percentage of atoms localized at the surface of a nanoparticle is also exponentially

increased (Figure 1.5)[18], which means that more reactive sites can be found in nanomaterials than those in bulk ones. As the specific surface area and the ratio of superficial versus total atoms are two major factors for evaluating whether a material can be utilized as a catalyst. Hence nanomaterials have a great potential in the field of catalysis. In addition, electron (or quantum) confinement can also be observed in nanomaterials. Electron confinement effect is essentially the direct influence of the energy band structure due to changes in the atomic structure. In a bulk conductive material, electron energy levels are normally continuous (semiconductors are the exception). But in nano size, especially clusters (1~10 nm), due to decreasing of atom quantities, electron energy levels are discrete (more discrete for semiconductors). This effect allows semiconductors such as CdS to absorb different light with different sizes[19-21]. Also, for anatase TiO_2, when the size decreases to 2 nm, the band gap (the energy gap between conduction band and valence band in semiconductors) increases to 3.4 eV, which is higher than the band gap (3.2 eV) of bulk anatase TiO_2.

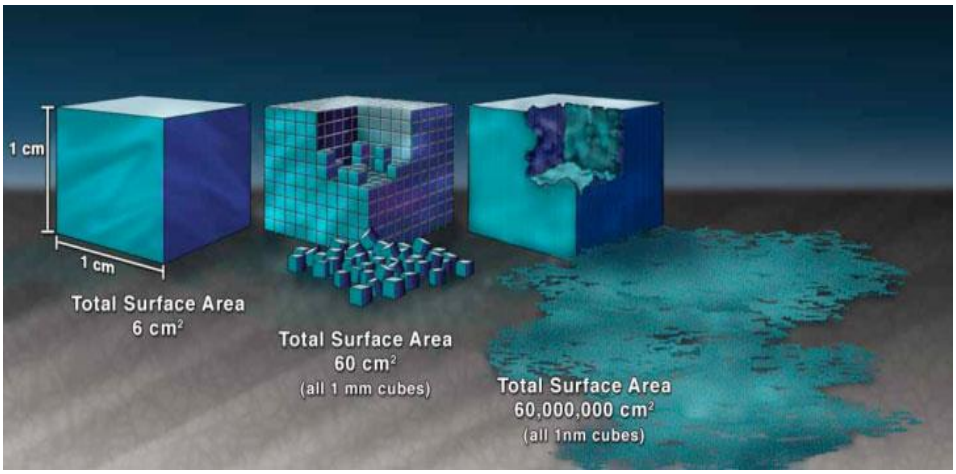

Figure 1.4. Illustration of the effect of the increased surface area provided by nanostructured materials[17]. Reprinted with permission from nano.gov.

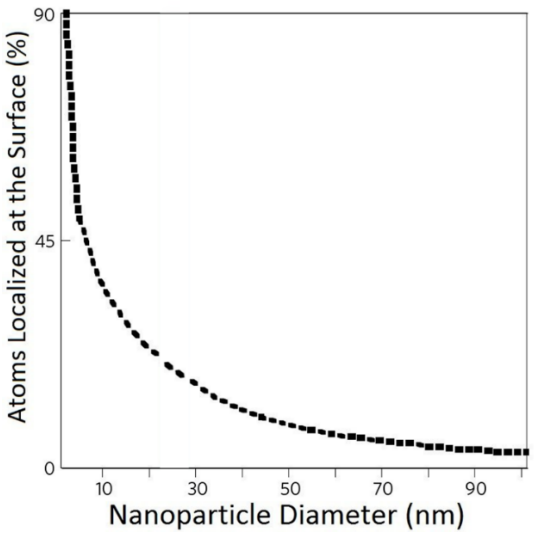

Figure 1.5. The percentage of atoms localized at the surface of a nanoparticle as a function of nanoparticle diameter for cubic shape with interatomic distance of 1.5 Å (redrawn from reference 18).

All these unique properties guarantee the bright future of application of nanomaterials. High specific surface area, high surface/total atom ratio, and tunable optical properties make nanomaterials act as potentially great catalysts. Among them, titanium dioxide is one of the most representative catalysts.

1.3 Titanium Dioxide

Titanium dioxide (TiO_2) is a white amphoteric powder with non-toxicity, great opacity, whiteness, and brightness, which makes it the best white pigment known today. Due to strong adhesion and chemical stability, titanium dioxide is widely applied in coatings, plastics, papermaking, printing inks, chemical fiber, rubber, cosmetics, and other industries. Its high melting point also makes it useful for making refractory glass, glaze, and enamel[22].

There are three main crystalline phases of TiO_2: rutile, anatase, and brookite. Rutile phase is most thermodynamically stable, and anatase phase can transform into rutile phase simply by heat, but not vice versa[23]. Both rutile and anatase phases can be easily synthesized and exhibit great catalytic properties. Meanwhile, brookite is less common in

all cases mainly due to its difficult synthesis[24]. Hence the dissertation will only talk about the rutile and anatase phases.

As shown in Figure 1.6, rutile (a) and anatase (b) TiO_2 crystal systems are both tetragonal[24]. But according to Wulff construction done by Ramamoorthy and Vanderbil[25], rutile is more thermodynamically stable than anatase thanks to containing low-energy (110) surface (Figure 1.7). Moreover, Mitsuhashi and his colleagues utilized high-temperature oxide melt solution calorimetry to determine the enthalpy change of anatase-to-rutile phase transition, which is -0.78 ± 0.2 kcal per mole. The negative enthalpy change further confirms that rutile is more stable than anatase[26]. Despite the stability of rutile TiO_2, anatase phase is widely recognized as a superior catalyst. This is because anatase has higher localized state density and smaller grain size, which allows anatase to provide carriers more efficiently as a result of limiting the energy loss caused by electron-hole recombination[27-29] comparing to its rutile counterparts. For example, Pt-doped anatase TiO_2 nanoparticles perform around 7 times better than Pt-doped rutile TiO_2 nanoparticles in hydrogen evolution using UV light[30].

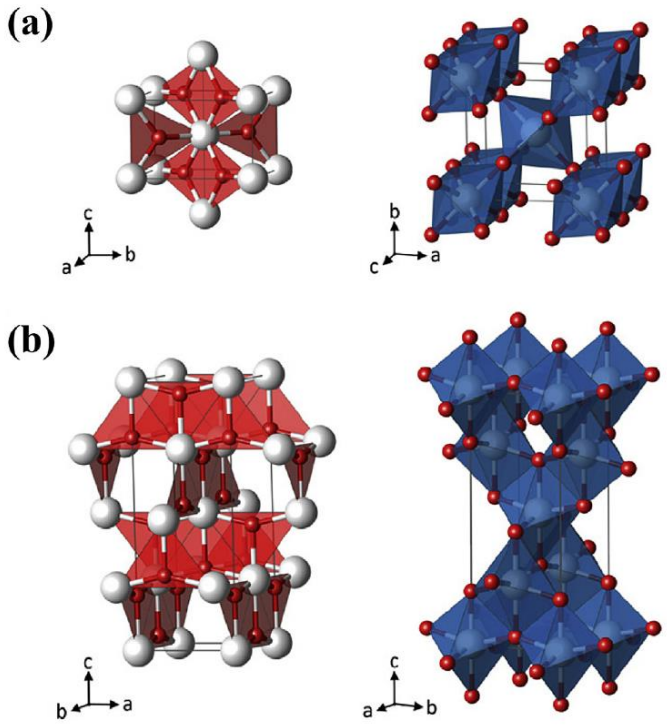

Figure 1.6. Planar Ti_3O building-block representation (left) and TiO_6 polyhedral (right) for the TiO_2 phases rutile (a) and anatase (b) (White balls represent titanium atoms and red balls represent oxygen atoms)[24]. Reprinted with permission from ref.24.

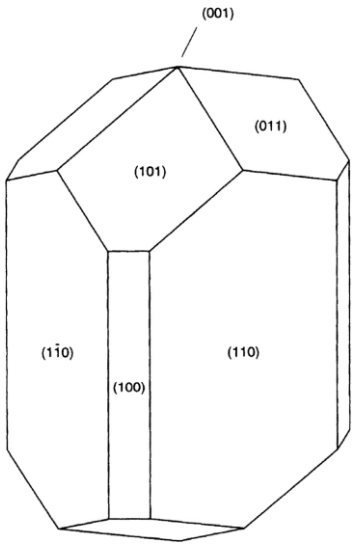

Figure 1.7. The equilibrium shape of macroscopic crystals of rutile TiO_2 by Wulff construction[25]. Reprinted with permission from ref.25.

Photocatalysts are the materials which absorb light to bring it to higher energy level and provide such energy to a reacting substance to make a chemical reaction occur, which means that the photocatalyst opens a path of doing reactions with light, not only with heat in the traditional ways. They provide the possibility of using sunlight directly as the energy source for reaction. TiO_2 nanoparticles, as one of the most representative photocatalysts, have an excellent light absorption in the UV region (Figure 1.8)[31]. That is the reason why TiO_2 nanoparticles are widely used in sunscreens. The uses for photocatalysis are restricted to the UV region of the solar spectrum, that is, about 90% of the visible region solar energy would be wasted when using regular TiO_2 (Figure 1.9)[32], which limits the application of TiO_2 nanoparticles as photocatalysts. To solve this problem, many approaches such as elemental doping[33, 34], metal decoration[35-39], and blackening treatment[40, 41] have been explored in the last two decades.

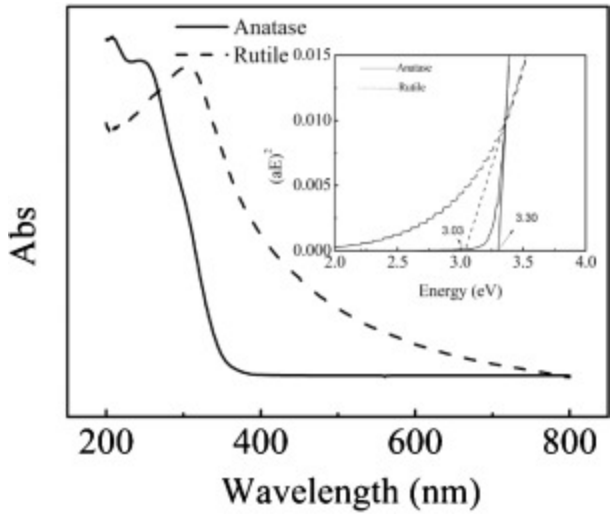

Figure 1.8. UV-vis diffuse reflectance spectra and Tauc plots (inset) of rutile and anatase TiO_2[31]. Reprinted with permission from ref. 31.

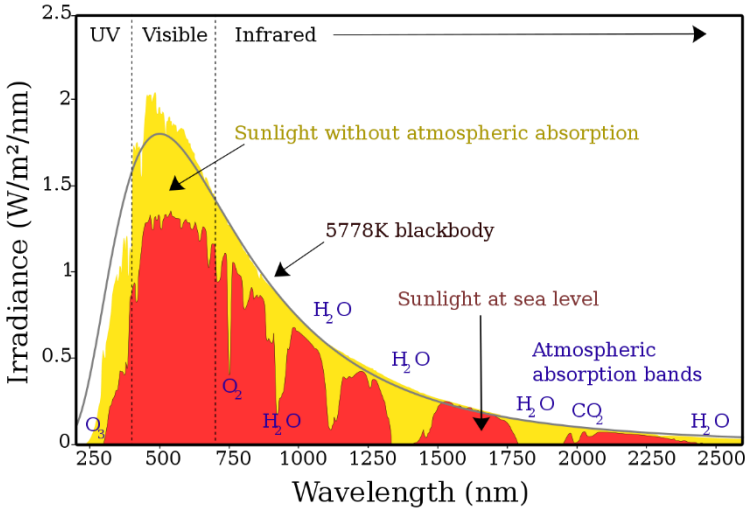

Figure 1.9. Spectrum of solar irradiation on earth[32]. Reprinted with permission from newport.com.

TiO_2 nanoparticles can be synthesized through methods such as deposition[42-44], sonochemical[45, 46], microwave-assist[47, 48], solvothermal[49, 50], and sol-gel methods[51-53]. Among all methods, solvothermal and sol-gel methods are the most popular for TiO_2 synthesis. P25, as a standard TiO_2 photocatalyst with diameter of 25 nm from Degussa Crop, is manufactured by flame hydrolysis[54].

The electrons on valence band of TiO_2 can be excited to the conduction band under light irradiation, while leaving holes at the valence band. The band gap in a certain TiO_2

nanoparticle is fixed and determines its optical properties. But it can be tuned by introducing second or third components into TiO_2 system.

Elemental doping changes the chemical nature and electronic structure of TiO_2. Enhancement of photocatalytic activity can be explained by narrowing the band gap and affecting electron-hole generation and separation capacity under illumination, which in turn will cause the red shift of light absorption[55] and longer hot electron (the electrons which are photoexcited) lifetime[56] respectively.

Noble metal or semi noble metal decoration is achieved by depositing corresponding metal or metal oxides onto P25. The heterostructure not only promotes the electron-hole separation, but also provides a new surface which is possibly more favorable for certain reactions. For example, Pt atoms on Pt-decorated P25 can attract hot electrons generated by photons. Meanwhile, Pt is known as an excellent metal for hydrogenation, which makes Pt-decorated P25 exhibit great activity in hydrogenation and hydrogen evolution reactions[57-59]. Apart from that, noble metals such as Ag[60], Au[61], Pd[62], and Pt[63] decoration can also allow the catalyst to extend the light absorption into the visible region.

Blackening treatment, as a relatively new method, only modifies the surface of TiO_2 nanoparticles, rather than introducing a second element into the system. The treatment consists of cooking TiO_2 nanoparticles under vacuum or a reducing environment, which may generate oxygen vacancies, Ti-H bonds, Ti^{3+} species, and/or hydroxyl groups on the surface resulting in the color change from white to yellow, blue, grey, or black[64]. Thus, black TiO_2 gains the ability of absorb both UV and visible light.

The modifications mentioned above expand the light absorption range into the visible, even near-infrared region. Black TiO_2, which is synthesized by a blackening treatment, will be specifically further discussed in this chapter.

1.4 Black Titanium Dioxide

TiO_2 with color other than white can be called black TiO_2. As blackening treatment is only changing the surface of the material, TiO_2 with different morphologies such as particles, plates, bars, and wire can be the candidates for black TiO_2. Lattice disorder resulting from the reason described in the previous section creates mid gap energy levels

between conduction band and valence band, which is the key of the unique optical and catalytical properties of black TiO_2.

1.4.1 Synthesis

There are many routes of synthesizing black TiO_2 such as hydrogenation, metal reduction, ascorbic acid reduction, $NaBH_4$ reduction, ethanol reduction etc.. All these methods will be introduced in this section.

1.4.1.1 Hydrogenation and Gas Treatment

Hydrogenation is the treatment involving hydrogen atmosphere at a certain temperature for various treating times. Hydrogen is a good reducing agent and used in many chemical reactions in alkene/alkyne reduction and the petroleum industry. In black TiO_2 synthesis, hydrogen can also reduce Ti^{4+} species on TiO_2 surface to Ti^{3+} and introduce oxygen vacancies. The gas treatment of TiO_2 mainly is in pure hydrogen, hydrogen/inert, or inert environment under different pressure.

Early in 1959, Cronzmeyer used hydrogen as reducing agent and successfully reduced rutile TiO_2 in several minutes at 600 – 800℃[65]. In 21 century, more controlled and better-designed methods have been established. Chen and his colleagues[40] heated TiO_2 at 200 °C in 2 MPa H_2 for 5 days to obtain black TiO_2. The photo, diffuse reflectance spectra, density of states (DOS), and high-resolution transmission electron microscopy (TEM) images before and after are shown in Figure 1.10. It is obvious that TiO_2 turned to totally black after the treatment. And from diffuse reflectance spectra, it proves that the black TiO_2 has the ability to absorb visible light. In Figure 1.10 (B), the DOS shows that the energy of highest occupied molecular orbital (HOMO) of valence band in TiO_2 is greatly expanded to the higher energy level, which dramatically decreases the band gap of black TiO_2, even the energy level of conduction band is also elevated. The highly crystalline structure of white TiO_2 can be seen in Figure 1.10 (C). But after hydrogenation treatment, surface disorder is achieved (Figure 1.10 (D)), and it is possibly due to the formation of Ti-H and Ti-O bonds, which is believed to be the reason why black TiO_2 has unique band gap and light absorption properties.

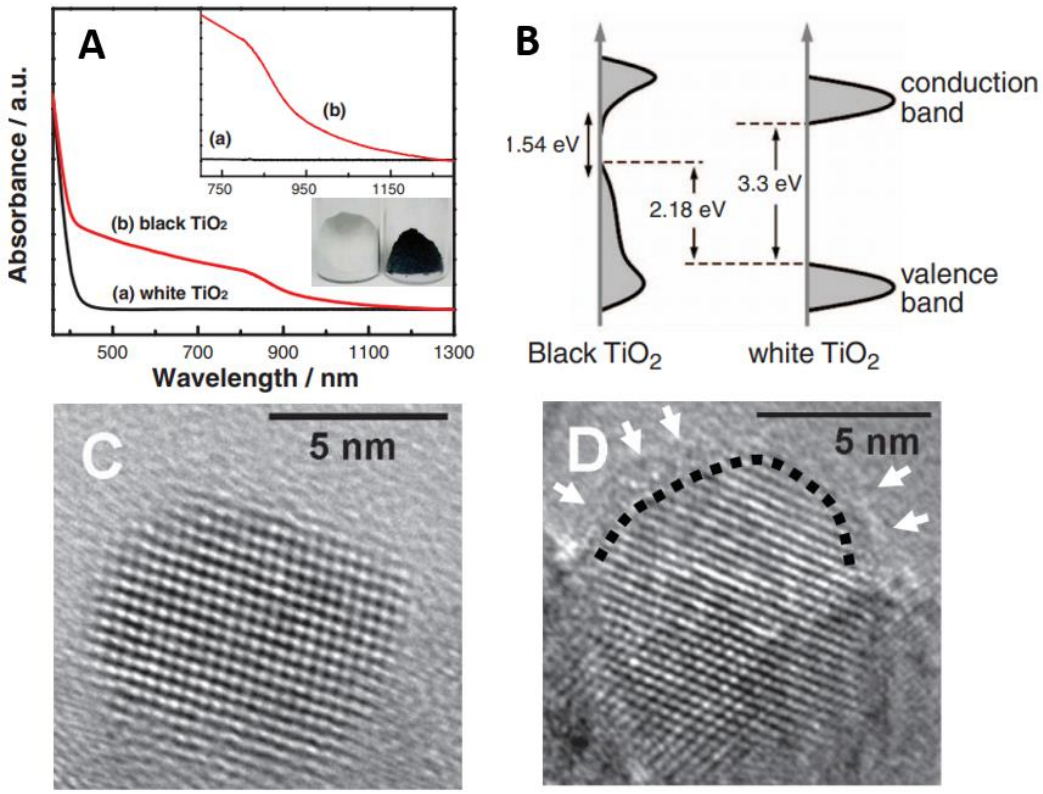

Figure 1.10. Diffuse reflectance spectra (Inset is the photo) (A), illustration of the density of states (B) of white and black TiO_2. (C) and (D) are high-resolution TEM images of TiO_2 before and after hydrogenation treatment, respectively[40]. Reproduced with permission from ref. 40.

Leshuk and colleagues studied the temperature influence in hydrogenation of TiO_2[66]. In their research, TiO_2 was treated in 2-MPa hydrogen for 1 day at 250, 350, and 450℃. Figure 1.11 (A) shows that higher temperature results in darker color. The corresponding Tauc plots also indicate that only higher temperature (450℃) can alter the band gap of their TiO_2 material.

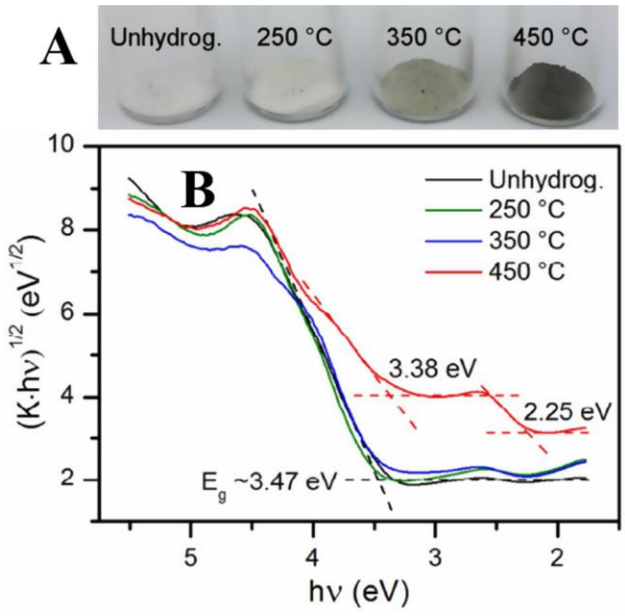

Figure 1.11. Photographs (A) of TiO_2 before and after hydrogenation treatment and corresponding Tauc plots (B)[66]. Reprinted with permission from ref. 66.

Lu and colleagues, on the other hand, did good research on the impact of treatment time for hydrogenation treatment of TiO_2[67]. They applied 3.5-MPa hydrogen on commercially available P25 at room temperature (15℃) for 0 to 20 days. The results are shown in Figure 1.12. At mild temperature, P25 needs at least 15 days to turn black and show visible-infrared light absorption ability.

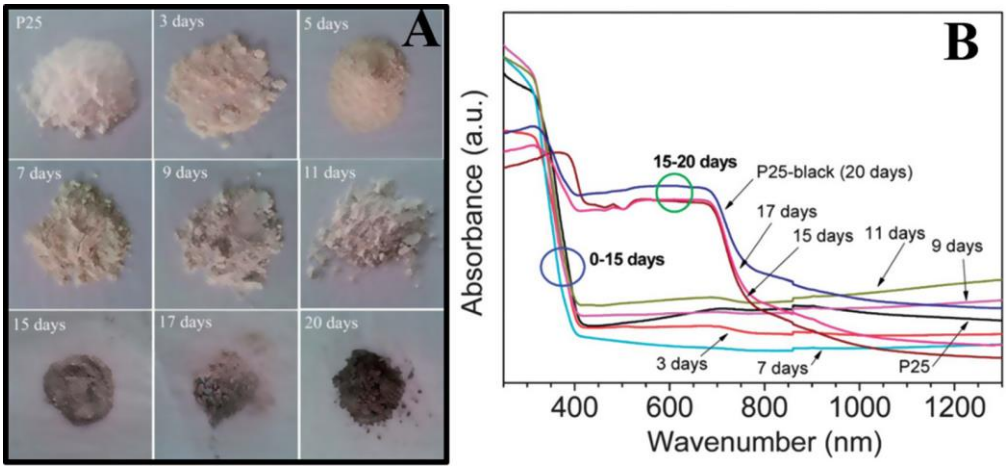

Figure 1.12. Photographs (A) of TiO_2 before and after hydrogenation treatment and corresponding diffuse reflectance spectra (B)[67]. Reprinted with permission from ref. 67.

In addition to pure hydrogen atmosphere, hydrogen/inert gas mixture and inert gas atmosphere are also well researched by many scientists. Lu et al. established a method of making black TiO_2 nanotube arrays in a tubular furnace at 500 °C for 1 hour with a 100 cm^3/min H_2/Ar (5:95) atmosphere[68]. Wei et al. reported a kind of black TiO_2 with high surface oxygen vacancy and Ti^{3+} concentration only by calcined white TiO2 in nitrogen alone[69].

1.4.1.2 Chemical Reduction

Unlike hydrogenation requires explosive gas – hydrogen and high-pressure containers, the chemical reduction treatment is facile and easy to use.

1.4.1.2.1 Metal Reduction

Inspired by the thermite reaction and forming Al-Ti alloy on TiO_2 by aluminum[70], Wang and his colleagues developed aluminum reduction treatment of making black TiO_2[71]. White TiO_2 and aluminum were first put separately in a two-zone tubular furnace. After vacuuming to 0.5 Pa, the Al chamber was heated to 800 °C first, and the TIO_2 was then heated to 300–600 °C for 6 or 20 hours. After reduction, the sample was calcined at 800 °C for 12 hours in Ar. Figure 1.13 shows a black color and broad UV-vis-infrared light absorption ability of black TiO_2. This method uses separate containers for reactants; thus, the product does not need to be purified. But the long 800 °C calcination can easily change the TiO_2 crystalline structure to rutile, which makes it impossible to make anatase black TiO_2 from this method. To prepare black TiO_2 in other crystalline phases, Zhu et al. synthesized black brookite TiO_2 from white brookite TiO_2 in a similar procedure as Wang's but without calcination[72]. Their results also show considerable amounts of lattice disorder and oxygen vacancy on the TiO_2 surface, as well as good broad-spectrum absorption.

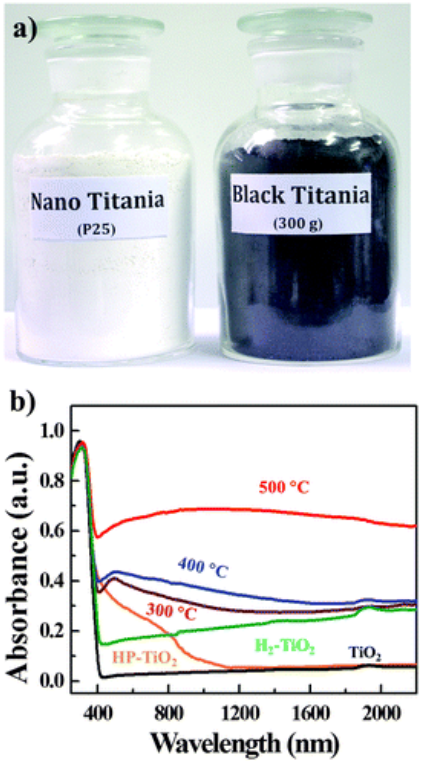

Figure 1.13. Photographs (a) of TiO_2 before and after aluminum reduction and corresponding diffuse reflectance spectra (b) (HP and H_2 are hydrogen treated references)[71]. Reprinted with permission from ref. 71.

Another metal, magnesium, was also used by Yu and colleagues for making black TiO_2[73]. Due to the relatively lower reductivity, magnesium reduction method needs to cooperate with H_2/Ar atmosphere to be finished.

1.4.1.2.2 Ascorbic Acid Reduction

Ascorbic acid, as known as vitamin C in daily life, is a good reductant in organic chemistry and living beings. Thanh-Dinh et al. used ascorbic acid solution to reduce carbon nano crystal-supported white TiO_2 in Teflon-lined stainless steel bomb at 180 °C for 24 h[74]. Muhammad and coworkers, on the other hand, used bottom-to-top method to achieve the same goal[75]. They mixed different concentrations of ascorbic acid and $TiCl_3$ aqueous solution, then adjust pH by NaOH solution and finally do hydrothermal reaction at 180 °C for 12 h to obtain the brown and black TiO_2.

1.4.1.2.3 $NaBH_4$ Reduction

Kang et al. made black TiO_2 by dipping white TiO_2 arrays into 0.1 M $NaBH_4$ solution for 40 min[76]. The black TiO_2 they synthesized has strong absorption in the visible-near infrared region. Tan and coworkers implemented another $NaBH_4$ reduction method using solid $NaBH_4$ other than its solution[64]. The white TiO_2 (anatase and rutile) was first ground thoroughly with $NaBH_4$ (4:1.5 w/w) powder. Then, the mixture was transferred in a crucible boat and place in a tubular furnace, heated from room temperature to 300–400 °C for 5-60 min under Ar. The results are exhibited in Figure 1.14. With the heating time and temperature increases, the color of black TiO_2 turns from grey, pale blue, dark blue to totally black. The corresponding DR spectra also follow the same trend and show stronger absorption in the visible region.

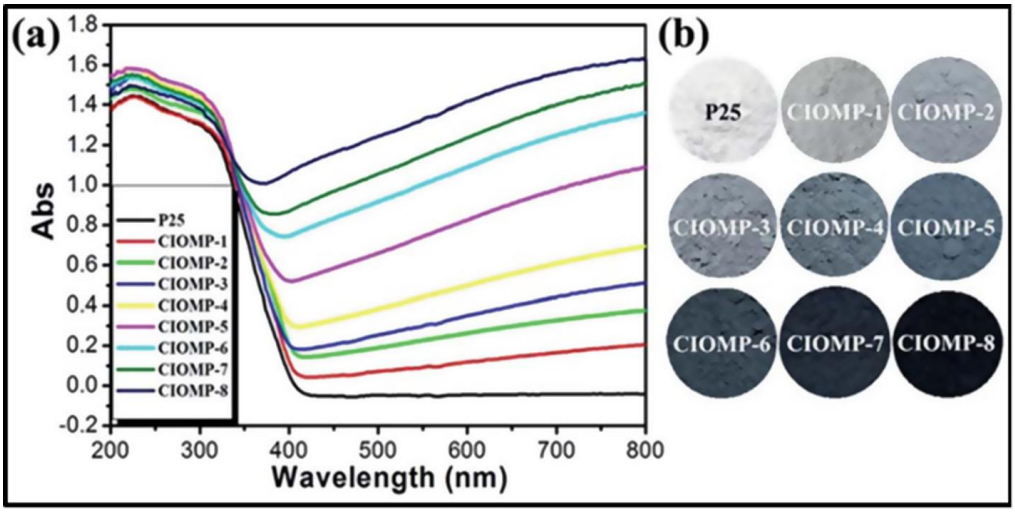

Figure 1.14. Diffuse reflectance spectra (a) and photographs (b) of relative TiO_2. CIOMP-1, treated at 300 °C for 5 min; CIOMP-2, 300 °C for 10 min; CIOMP-3, 300 °C for 20 min; CIOMP-4, 300 °C for 30 min; CIOMP-5, 300 °C for 40 min; CIOMP-6, 300 °C for 50 min; CIOMP-7, 300 °C for 120 min; CIOMP-8, 350 °C for 60 min[76]. Reprinted with permission from ref. 76.

1.4.1.2.4 Ethanol Reduction

Ethanol not only is the traditional solvent for organic solutions, but also acts as a reducing agent in organic synthesis. Here, Chen and colleagues established a very facile way of making black TiO_2 by heating TiO_2 ethanol suspension in a tubular furnace for 3 hours at 400 °C under Ar[77]. The obtained black TiO_2 does not require any purification as the gaseous by-product of the reaction diffuses in the reaction chamber along with the

reaction. Figure 1.15 (a) shows that ethanol-reduced black TiO_2 exhibits good visible light absorption ability and same absorption in UV region. Besides, the X-ray diffraction patterns (Figure 1.15 (b)) indicate that the treatment will not change the crystalline phase of TiO_2, which can potentially be applied in the black TiO_2 synthesis for other TiO_2 crystalline phases.

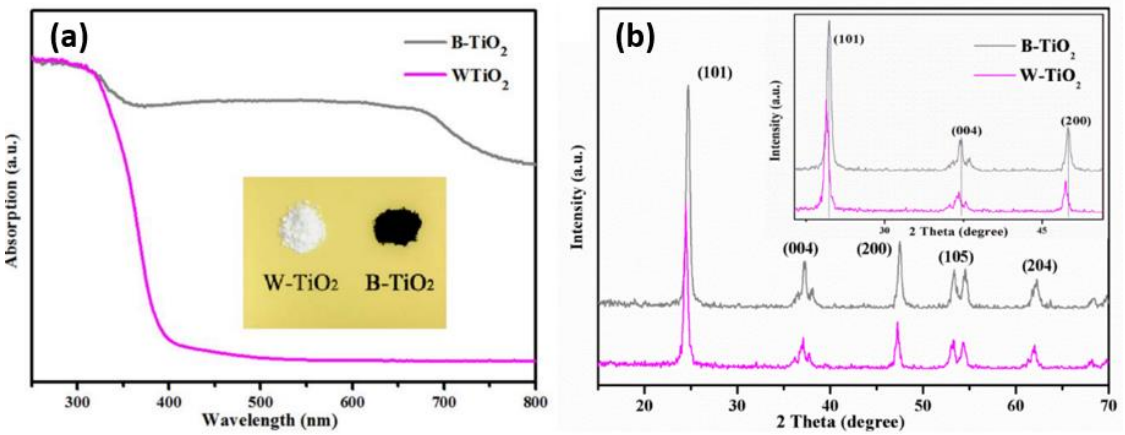

Figure 1.15. Diffuse reflectance spectra (a), photographs (inset), and XRD patterns (b) of white and black (anatase) TiO_2[77]. Reprinted with permission from ref. 77.

1.4.1.3 Other Methods

Other than all methods described above, electrochemical reduction[78], plasma reduction[79], laser irradiation[80], proton implantation, ultrasonication are also applied in production of black TiO_2 materials. A blue TiO_2 nanotube arrays were synthesized by electrochemical anodization and reduction by Yang and coworkers[78]. Yan et al performed a method using inductively coupled plasma power with H_2 flow to turn precursor TiO_2 into black at 390 °C for 3 hours[79]. Chen and colleagues prepared black TiO_2 nanospheres by pulsed-laser irradiation[80]. The white TiO_2 suspension was irradiated by a pulsed laser (λ = 355 nm, pulse duration = 8 ns, frequency = 10 Hz, power = 0.35 W, instantaneous power = 4.4 MW) for 5 to 120 minutes. Figure 1.16 shows that the TiO_2 turns to gray after min, and then becomes totally black after 120 min. The visible light absorption of TiO_2 also increases along the irradiation time extends.

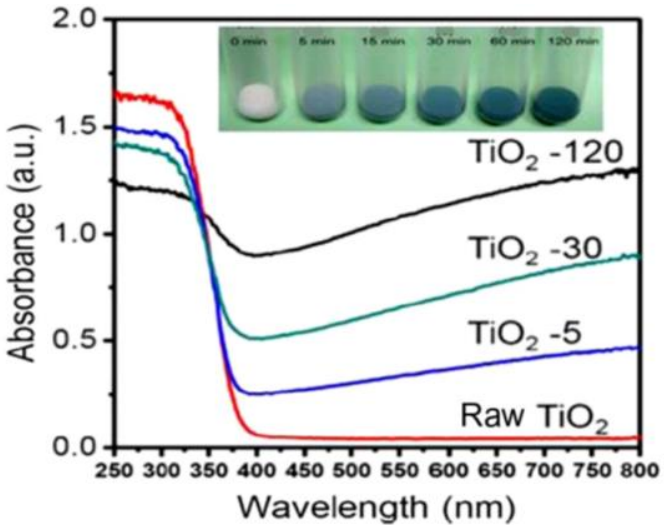

Figure 1.16. Diffuse reflectance spectra and photographs (inset) of white and black TiO_2[80]. Reprinted with permission from ref. 80.

1.4.2 Properties

The unique performance of black TiO_2 is attributed to its unique properties as followed: disordered surface, surface Ti-OH/Ti-H species, oxygen vacancy and Ti^{3+} species, and valence band edge.

1.4.2.1 Surface Disorder

As shown in TEM images in Figure 1.10 (C) and (D), a 1-2 nm disordered layer appeared after the blackening treatment of black TiO_2 that Chen and his colleagues synthesized. Similar disordered layers are also found in black TiO_2 material prepared by Wang[81], Tian[82], Cai[83], and many other researchers with different methods. This evidence approves the existence of disordered layer in black TiO_2 materials.

1.4.2.2 Surface Ti-OH/Ti-H Species

The existence of Ti-OH and Ti-H species can be observed by X-ray photoelectron spectroscopy (XPS). As shown in Figure 1.17, the Ti-OH peak was located at 530.9 eV in the O 1s XPS spectrum taken from Chen's black TiO_2[40]. Another technique to identify the existence of Ti-OH species is Fourier transform infrared (FT-IR) spectroscopy. Ti-OH can be revealed by comparing the magnitude of the intensity of -OH vibrational band[84]. The

appearance of Ti-H species sometimes can be seen in hydrogenated black TiO_2 materials. It can be approved by the shoulder peak at around 457.3 eV in the Ti 2p XPS spectrum[85].

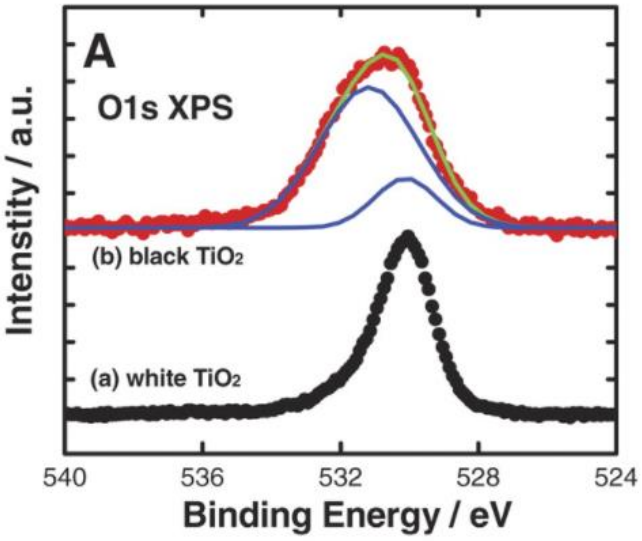

Figure 1.17. O 1s XPS spectra of the white and black TiO_2 nanocrystals[40]. Reprinted with permission from ref. 40.

1.4.2.3 Oxygen Vacancy and Ti^{3+} Species

Ti^{3+} species can be detected by Ti 2p XPS spectrum. For example (Figure 1.18), two small shoulder peaks near 458.0 eV and 462.2 eV found in Yuan's black TiO_2 nanobelts is from Ti^{3+}[86]. Oxygen vacancies cannot be determined by conventional XPS or TEM, its existence is normally approved by electron paramagnetic resonance (ESR) spectrometer. For example, oxygen vacancies were seen in ESR spectra of hydrogenated[87], Al reduced[86], and electrochemical reduced[88] black TiO_2 materials.

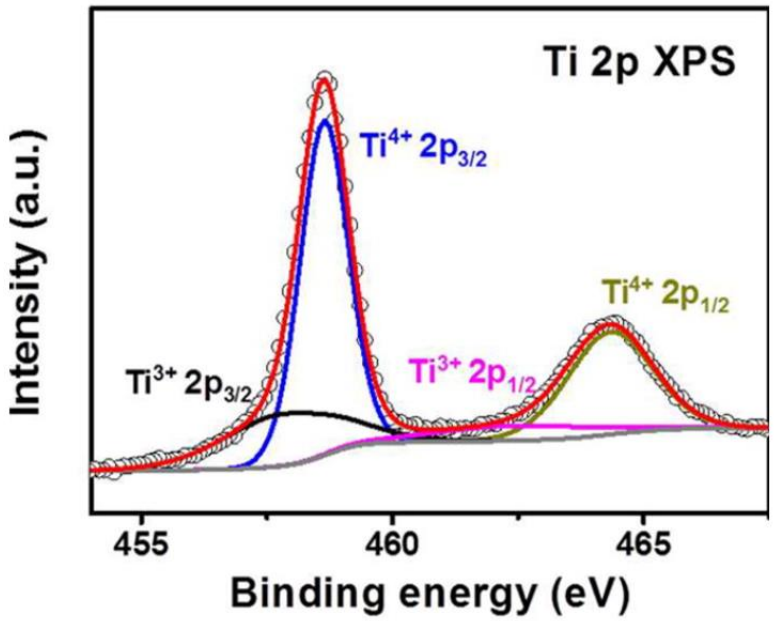

Figure 1.18. Ti 2p XPS spectra of the black TiO_2 nanobelts[86]. Reprinted with permission from ref. 86.

1.4.2.4 Valence Band Edge

The valence band shift of 2.18 eV can be easily seen in Figure 1.10 (B) in the black TiO_2 synthesized by Chen[40], which largely decreases the band gap of the black TiO_2. Similar phenomena can also be observed in the black TiO_2 material from other research groups[89-91].

1.4.3 Applications

Black TiO_2, as a new extension of TiO_2 materials, shows unique light absorption and surface properties, which provides a great potential in applying in many scenarios.

1.4.3.1 Photocatalytic Degradation of Organic Compounds

Developing efficient and cheap ways of purifying contaminated water is always a hot topic for chemists and environmental scientists. Regular white TiO_2, as a heterogeneous photocatalyst, has been thoroughly studied in organic compound degradation. It has excellent performance under UV light, but inert towards visible light. While black TiO_2 which absorbs the light in visible and even infrared region, has a bright future of utilizing artificial or natural solar light for degrading organic compound in water.

Zhou and colleagues synthesized a core-shell TiO_2@$TiO_{2-x}H_x$ catalyst by hydrogen plasma technique[81]. As shown in Figure 1.19, the core-shell black TiO_2 catalyst degrades 90% of methyl orange (MO) in 4 minutes under the irradiation of AM 1.5 solar power system, while the pristine TiO_2 catalyst needs 12 minutes to reach the same degradation ratio.

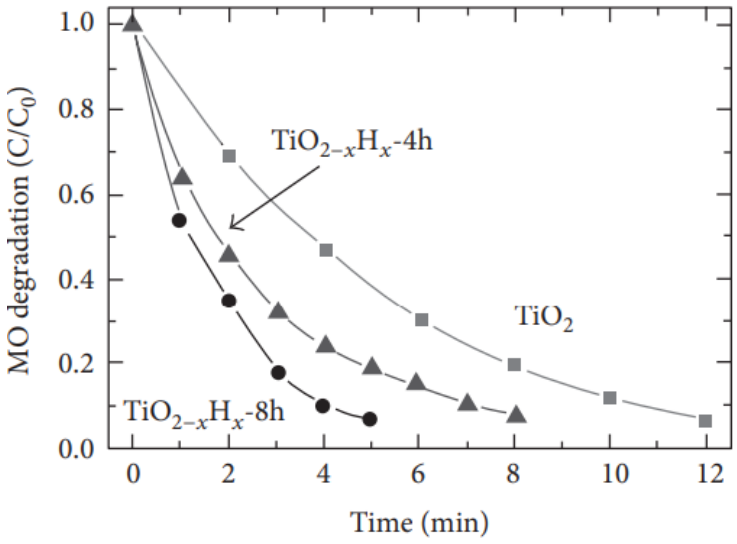

Figure 1.19. Solar-light driven photocatalytic decomposition of 0.1 M methyl orange (MO) over pristine TiO_2 and core-shell TiO_2@$TiO_{2-x}H_x$ catalysts[81]. Reprinted with permission from ref. 81.

Miao et al. reported a catalyst with black TiO_2/ TiO_2 homojunction, which performs better than both black and white TiO_2 alone[92]. The catalyst was synthesized by reacting ascorbic acid-reduce black TiO_2 with pristine white TiO_2 at strong basic condition at 180 °C for 12 hours. Diffuse reflectance spectra (Figure 1.20 (a)) shows that black TiO_2 has the best light absorption ability. But it is interesting that the best rhodamine B degradation performance comes from catalyst with black TiO_2/ TiO_2 homojunction (0.6g B/W-TiO_2) with the kinetic constant of 0.012 min^{-1}.

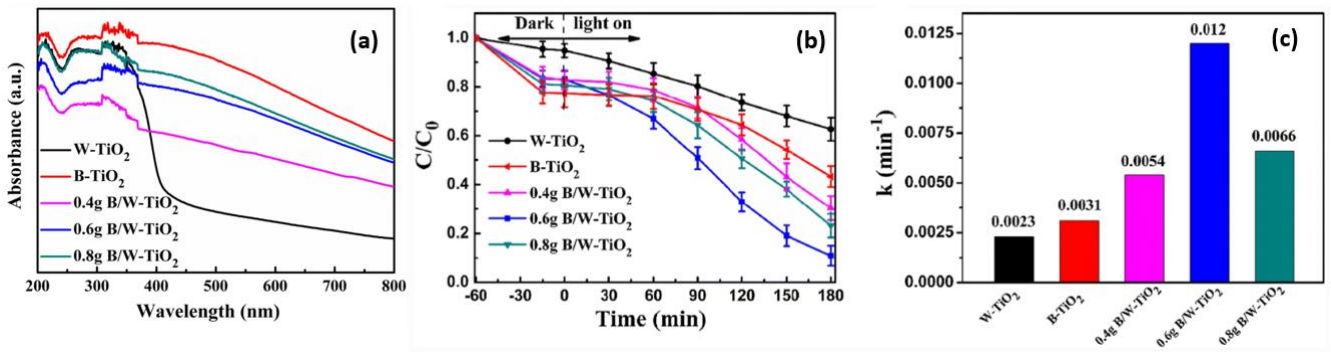

Figure 1.20. (a) Diffuse reflectance spectra of TiO_2 catalysts. Degradation curves (b) and corresponding kinetic constants of rhodamine B degradation (5mg/L, irradiated by 300 W Xenon lamp) by TiO_2 catalysts[92]. Reprinted with permission from ref. 92.

Some black TiO_2 catalyst also shows the activity of degrading organic solvents such as toluene and ethyl acetate. Bi and coworkers discovered that Al-reduced black TiO_2 has superior toluene and ethyl acetate degradation activity than white TiO_2[93]. As shown in Figure 1.21, black TiO_2 with higher treating temperature has better degradation activity for both toluene and ethyl acetate under both visible and full solar irradiation. What is surprising is that the white TiO_2 can also work under only visible light irradiation (black line in Figure 1.21 (b)), which is possibly due to the physical adsorption of organic molecules onto catalyst's surface.

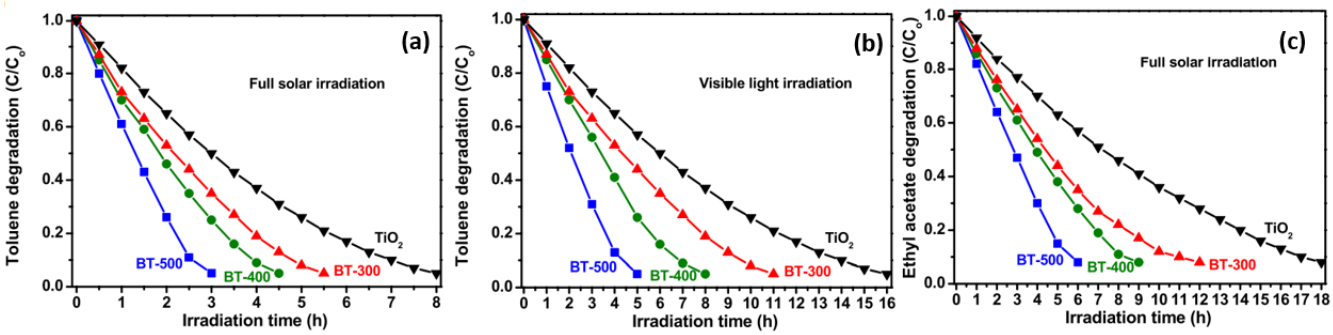

Figure 1.21. Toluene (50 mg/L) degradation by different TiO_2 catalysts under solar (a) and visible (b) irradiation. Ethyl acetate (50 mg/L) degradation by different TiO_2 catalysts under solar irradiation (c)[93]. 300 W Xe lamp is the irradiation source. Reprinted with permission from ref. 93.

1.4.3.2 Photocatalytic Water Splitting

Hydrogen gas is the cleanest fuel because it only generates water when it is consumed. Vice versa, water splitting is also the cleanest process of making hydrogen gas as oxygen is the only by-product. Due to the high redox potential and stability of water molecules, it is urgently needed to develop a method of splitting water other than the traditional electrochemical or thermal ways[94]. The usage of photon in water splitting has been researched for years. Photocatalytic TiO_2 such as regular white TiO_2 and new black TiO_2, are also widely evaluated.

Zhou's core-shell TiO_2@$TiO_{2-x}H_x$ catalyst performs not only better in methyl orange degradation, but also in hydrogen evolution[81]. The Pt-loaded core-shell TiO_2@$TiO_{2-x}H_x$ catalyst produces around 10 mmol h^{-1} g^{-1} H_2, while the Pt-loaded pristine TiO_2 only produces 0.8 mmol h^{-1} g^{-1} (Figure 1.22).

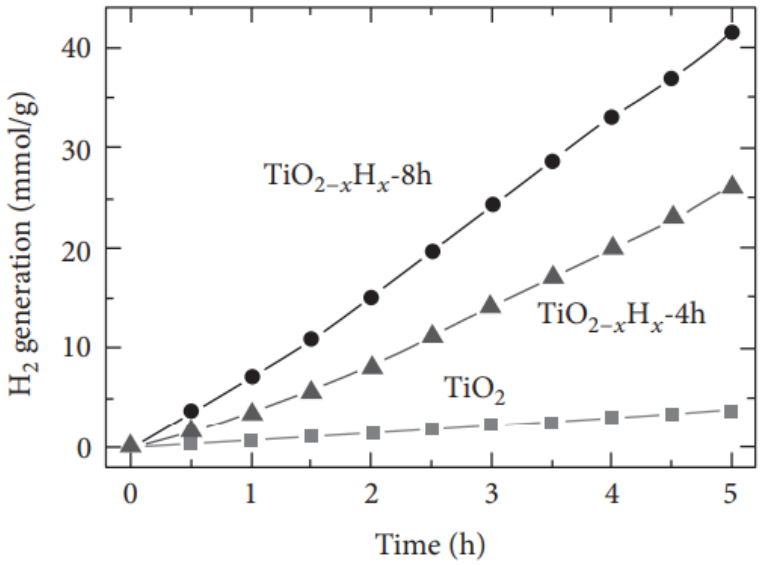

Figure 1.22. Solar-light driven photocatalytic hydrogen evolution (25% methanol solution) over pristine TiO_2 and core-shell TiO_2@$TiO_{2-x}H_x$ catalysts[81]. Reprinted with permission from ref. 81.

Liu et al. successfully synthesized black TiO_2 using air, H_2/Ar, Ar, and high-pressure H_2, and then compared their hydrogen evolution capabilities[95]. The results are shown in Figure 1.23, high pressure hydrogen-treated TiO_2 nanotubes (HP-H_2) gives almost 7 μmol h^{-1} g^{-1} H_2, while the lower temperature-treated one (Sci ref) performs as half

as HP-H_2 does. Other three different black TiO_2 catalysts only evolute a small amount of hydrogen under open circuit condition.

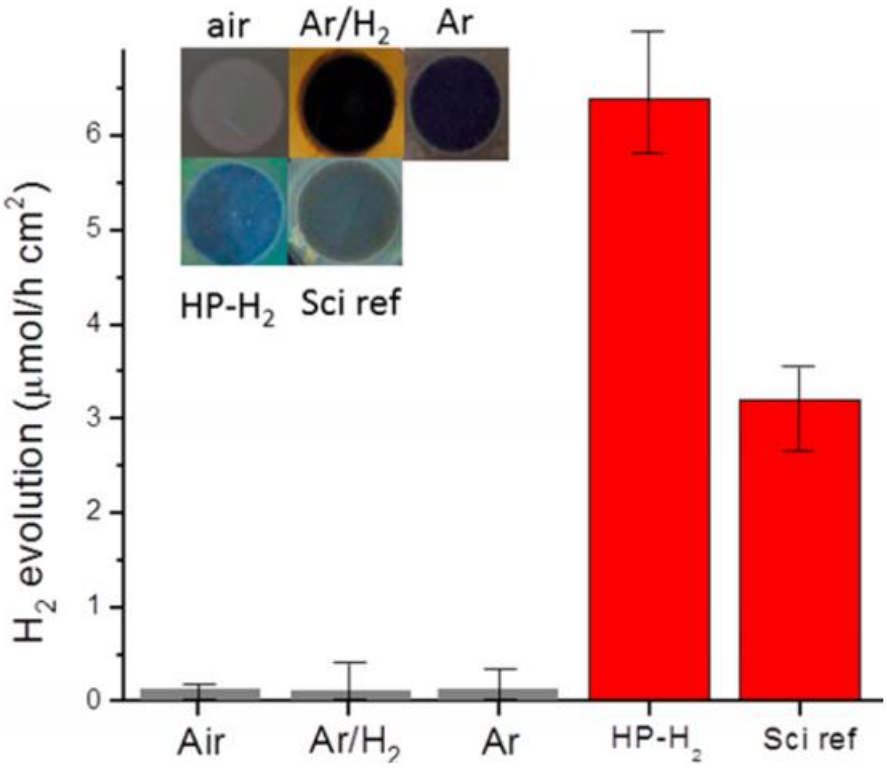

Figure 1.23. Photocatalytic hydrogen evolution under open circuit conditions in methanol/water (50/50 vol %) with TiO_2 nanotubes treated in different atmospheres under AM 1.5 (100 mW/cm^2) illumination. Air, heat treatment in air at 450℃; Ar, heat treatment in pure argon at 500℃; Ar/ H_2, heat treatment in H_2/Ar (5 vol %) at 500℃; HP-H_2, heat treatment in H_2 at 2 MPa at 500 °C; Sci ref, heat treatment in H_2 at 2 MPa at 200 °C for 5 days[95]. Reprinted with permission from ref. 95.

An ordered mesoporous black TiO_2 catalyst was prepared by Zhou and colleagues by hydrogenation at 500 °C for 3 hours[96]. They test its hydrogen evolution ability in methanol solution (20%, v/v) with 1% Pt loading. Figure 1.24 shows that ordered mesoporous black TiO_2 has H_2 evolution ability of near 30 μmol h^{-1} g^{-1} under only visible light irradiation. With solar irradiation, both black and pristine ordered mesoporous TiO_2 exhibit H_2 evolution ability. Comparing three different plots in Figure 1.24, it can be discovered that blackening treatment not only makes the catalyst have the ability to use visible light, but also enhances the performance of the catalyst in the UV region.

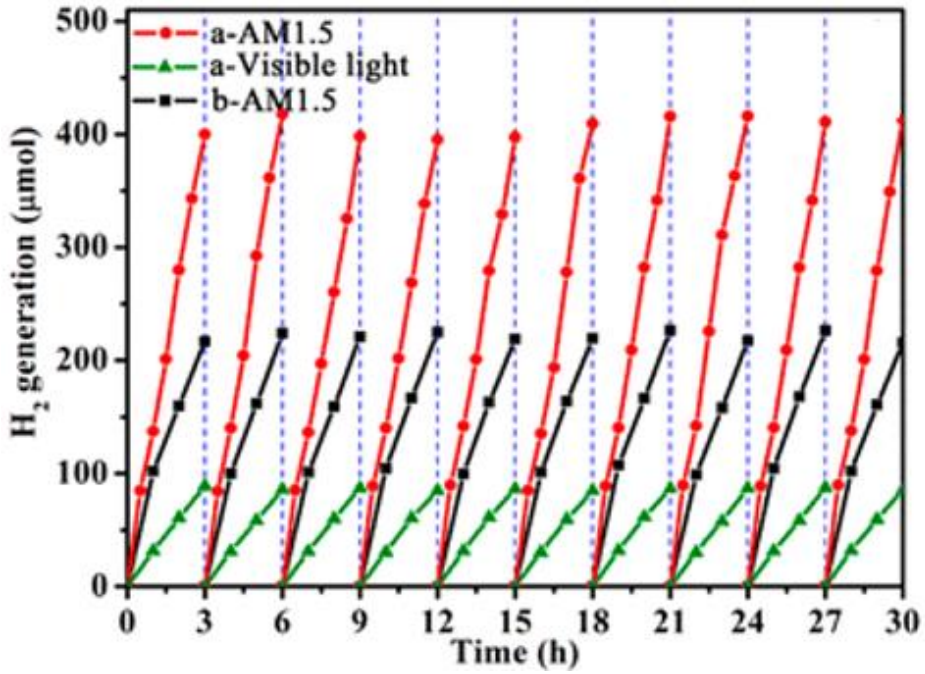

Figure 1.24. Photocatalytic hydrogen evolution of the ordered mesoporous black TiO_2 (a) and pristine ordered mesoporous TiO_2 materials (b)[96]. Reprinted with permission from ref. 96.

1.4.3.3 Other Applications

Black TiO_2 materials are also useful in many other areas. Li and coworkers used mesoporous hydrogenated TiO_2 microspheres in lithium battery to achieve the rate capability of 391 mAh/g[97] at 0.5 C. Lu et al developed a supercapacitor using hydrogenated TiO_2 nanotube arrays, which is 40 times better than its white counterpart[98]. Black TiO_2 is also applied in the fuel cell field. Zhang and colleagues hydrogenated TiO_2 nanotube arrays as the support for ternary tin–palladium–platinum catalysts in a fuel cell, which has a power of 1.21 kW/g_{Pt} when used as the cathode[99]. Other than examples mentioned above, black TiO_2 materials are used in field emission[100], microwave absorption[101], photothermal therapy[102], and other areas.

1.4.4 Summary

In summary, black TiO_2 materials are attracting researchers' attention due to their unique surface, band gap, and light absorption properties. Many methods were developed

in the past ten years varying from hydrogenation, reduction, to plasma and sonication. black TiO_2 materials are also applied in many fields such as photocatalysis, fuel cell, supercapacitor, and photothermal therapy. Especially in photocatalytic areas, black TiO_2 materials with/without cocatalyst, with/without support, and with different morphologies were vastly investigated for degradation of organic compound and hydrogen evolution. But for many regular TiO_2 catalyzed reactions such as Suzuki coupling, decarboxylation reaction has not been tested with black TiO_2 materials. In all, the current study state of black TiO_2 is still in a trial-and-error stage. There are still many theories and discoveries to be made in this research area.

1.5 Magnetic Nanoparticles

Although nanocatalysts such as TiO_2 and black TiO_2 have excellent catalytic activity in many reactions, the post-reaction process, especially the separation of catalyst from reaction media, is always a big challenge. The traditional separation methods like centrifugation, filtration, and sedimentation are either consisting multiple steps or time-consuming, sometimes even hard to completely separate due to their small size. To overcome such limitations, magnetic nanoparticles (MNPs) make it possible to separate catalyst from reaction mixture by only applying an external magnet, and then decant supernatant from the reaction container.

Common magnetic nanomaterials include alloys (Fe, Co, Ni), iron oxides (Fe_2O_3, Fe_3O_4), and ferromagnetic materials MFe_2O_4 (M = Mn, Mg, Zn, Co, Fe). Among them, magnetite (Fe_3O_4) is most studied.

1.5.1 Synthesis

There is a wide range of approaches have been developed to synthesize magnetic nanoparticles. The earliest method to produce MNPs was performed by Papell in 1965[103]. He milled Fe_3O_4 with oleic acid and heptane for 19 days to obtain MNPs with size around 135 nm. Nowadays, the most popular methods are sol-gel method, co-precipitation, hydrothermal method, and thermal decomposition.

1.5.1.1 Sol-gel Method

The sol-gel method is a universal method for making a huge range of chemicals including TiO_2 and many MNPs. The simplified procedure is described as follows: a basic solution is added to an iron precursor solution ($FeCl_3$ for example) under stirring. Then the mixture is agitated at 50-100 °C to form a $Fe(OH)_3$ gel. Finally, the gel is aged at 50 to 100 °C for several days to obtain the MNPs with size from 30-300 nm[104]. In order to enhance the stability of the gel, citric acid can be added into the reaction mixture to form the citric acid dry gel by evaporating the solvent upon agitation. Then the dry gel can be ground and then calcined at 100 °C to produce magnetic α- Fe_2O_3 particles[105].

The morphology, size, and size distribution can be controlled by changing precursor's concentration, solution pH, aging temperature and time, stirring speed, and adding another gel source[106].

The sol-gel method is also available for coating if needed. For example, silica-coated α- Fe_2O_3 nanoparticles can be made by simply heating tetraethylorthosilicate (TEOS) solution with iron precursor solution at 400 °C for 10 h[107].

1.5.1.2 Co-precipitation

Co-precipitation is the most facile and quickest way of making magnetic α- Fe_2O_3 and Fe_3O_4 nanoparticles. A strong basic solution is added into the solution of $FeCl_2$ and $FeCl_3$ to cause the reaction ($Fe^{2+} + 2Fe^{3+} + 8OH^- \rightarrow Fe_3O_4 + 4H_2O$) to form final magnetic Fe_3O_4 nanoparticles[108]. It is important to note that the precursor type (e.g., nitrate and chloride), solution pH[109], ferric/ferrous ratio[110], temperature[111], mixing order, mixing rate[112], and ionic strength of solution[113] can dramatically influence the morphology and size of the final MNPs. The method just introduced above usually produces negative-charged particles, which tend to agglomerate. To prevent agglomeration from happening, capping agents such as surfactant can be added to modify the surface electrochemical environment to stabilize and functionalize the MNPs[114].

1.5.1.3 Hydrothermal Method

Hydrothermal reaction involves Teflon-lined stainless-steel bomb with high temperature (higher than 150 °C) and high pressure (higher than 14 MPa), thus, it is often called bomb reaction. The basic chemistry in hydrothermal reaction is the oxidation and hydrolysis of iron salts.

Li and coworkers successfully prepared many nanoparticles including magnetic Fe_3O_4 nanoparticles with a narrow size distribution by heating a mixture of $FeCl_3$, ethylene glycol, sodium acetate, and polyethylene glycol in a bomb at 200 °C for 8-72 hours[115].

1.5.1.4 Thermal Decomposition

Thermal decomposition is the method that gives the best monodispersity and crystalline structure. Typically, iron precursors (normally it is $Fe(CO)_5$) are added into the mixture of oleic acid and octyl ester at 100℃. Then the mixture is refluxed at 100 °C for 1 hour while the color of the solution turns black from orange. After final dehydrated $(CH_3)_3NO$ treatment, the magnetic γ-Fe_2O_3 nanoparticles with fine structure and crystalline can be obtained (Figure 1.25)[116]. This method however has two drawbacks, which are the severe toxicity of $Fe(CO)_5$ and complicated procedure.

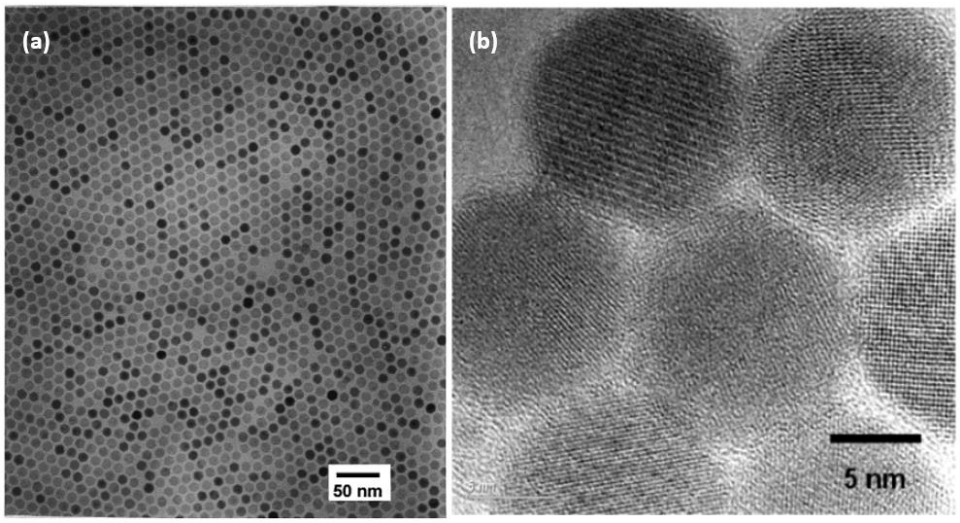

Figure 1.25. TEM (a) and high-resolution TEM (b) images of 11 nm magnetic γ-Fe_2O_3 nanoparticles[116]. Reprinted with permission from ref. 116.

1.5.1.5 Other Methods

Other than all methods discussed above, sonochemical processing[117], flow injection[118], microwave-assist method[119], spray pyrolysis[120], and many other methods are also implemented for synthesizing MNPs.

1.5.2 Applications

Magnetism of MNPs is not the only useful properties, the nanosize also gives them a good potential for acting as a good catalyst. On the other hand, MNPs are applied in medical imaging and drug delivery as well.

1.5.2.1 Magnetic Separation Component

Stein et al synthesized magnetic chemically-derived graphene-supported Fe NPs (Fe-NP/CDG) and used them for hydrogenation reactions[121]. Figure 1.26 shows that the catalyst can easily be separated by applying an external magnet. Fakri and coworkers prepared a new kind of magnetic Fe_3O_4@chitosan-based Cu complex for selective oxidation of sulfides to sulfoxides[122]. The catalyst can be removed simply by a magnet as well.

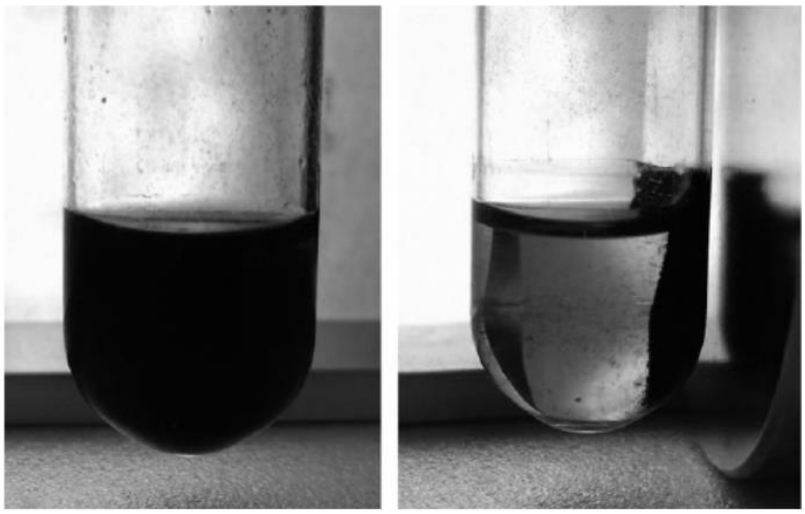

Figure 1.26. Magnetic separation of Fe-NP/CDG before and after applying an external magnet[121]. Reprinted with permission from ref. 121.

1.5.2.2 Catalyst

Lee's group synthesized magnetic porous α-Fe_2O_3 nanorods and tested their carbon monoxide oxidation activity at 25-600 °C in a CO (1.0%)/O_2 (2.5%)/N_2 gas flow (40 mL/min)[123]. It shows a great CO oxidation ability at higher temperature. A new magnetic $ZnFe_2O_4$–CuO–C_3N_4 ternary heterojunction photocatalyst was prepared by Rostami et al and examined its photodegradation ability for methylene blue[124]. Results show that degradation can be finished within 80 minutes, and the $ZnFe_2O_4$ not only acts as the

magnetic component, but also has catalytic activity through the Fenton reaction pathway. Kargar and coworkers established a method for oxidative desulfurization using Fe_3O_4/ZIF-8/TiO_2 catalyst[125]. The catalyst was synthesized by co-precipitation of $FeCl_3$ and $FeSO_4 \bullet 7H_2O$ in an acidic solution. Results indicate that the existence of Fe_3O_4 provides the magnetic separation ability and higher catalytic activity at the same time.

1.5.2.3 Biological Applications

Magnetic nanoparticles, especially Fe_3O_4, attract a lots attention in bioimaging, therapy, and drug delivery due to their low cell toxicity.

Chen and colleagues developed non-invasive IMTP- Fe_3O_4-PFH NPs for multimodal imaging of ischemic myocardium in rats[126]. The unique properties of Fe_3O_4 as the imaging agent have higher resolution in both photoacoustic and magnetic resonance imaging. Song's group successfully prepared a novel nano-contrast agent (CMR) containing Fe_3O_4 as an active component in both imaging and therapy[127]. Their CMR is able to target the breast tumor precisely and shows excellent MRI and fluorescence dual-model imaging property against orthotopic brain glioma tumor. It is also found that this CMR can inhibit the growth of breast tumors.

Anirudhan and Christa reported a pH/temperature-sensitive drug delivery system using Fe_3O_4 as the magnetic guidance component for delivering anticancer drug, 5FU[128]. This system can load a big amount of drug with an enantiomer excess of 93.5% and release the drug at target by magnetic guidance. The cytotoxicity towards cancer cells can be further improved by addition surface modification of the drug carrier.

1.5.3 Summary

In summary, numerous methods have already been established for making magnetic materials such as magnetic γ-Fe_2O_3, magnetic α-Fe_2O_3, and Fe_3O_4 nanoparticles. Among all methods, co-precipitation and sol-gel are the easiest to do, but the poor size distribution and difficulty of controlling reaction parameters hinder their usage. Thermal decomposition of $Fe(CO)_5$ gives the best crystalline and monodispersity, but the toxicity of the precursor and complicated procedure make it hard to be popularized. Hydrothermal method although takes relatively longer time and requires special bomb reactors, the

narrow size distribution can still be achieved. Comparing with other methods, it appears to be one of the best choices of make MNPs.

The applications of MNPs include but are not limited to all described in this section. For a chemist, the most interesting application of MNPs is their magnetic separation and unique catalytic activity towards certain reactions such and photo-Fenton reactions.

References

1. Navlani-García, M.; Verma, P.; Salinas-Torres, D.; Raja, R.; Mori, K.; Yamashita, H., Single-Site Heterogeneous Catalysts and Photocatalysts for Emerging Applications. In *Advanced Heterogeneous Catalysts Volume 2: Applications at the Single-Atom Scale*, American Chemical Society: **2020**; Vol. 1360, pp 151-188.
2. Scaiano, J. C.; Lanterna, A. E. *The Journal of Organic Chemistry* **2017,** 82, (10), 5011-5019.
3. Janice Gorzynski Smith, D., *Organic Chemistry*. McGraw-Hill Education: **2013**.
4. Zhang, Y.-Y.; Wei, Y.; Shi, M. *Chemical Communications* **2019,** 55, (29), 4210-4213.
5. Wan, N.; Zhou, X.; Ma, R.; Tian, J.; Wang, H.; Cui, B.; Han, W.; Chen, Y. *Advanced Synthesis & Catalysis* **2020,** 362, (5), 1201-1207.
6. Li, S.; Liu, Y.; Huang, B.; Zhou, T.; Tao, H.; Xiao, Y.; Liu, L.; Zhang, J. *ACS Catalysis* **2017,** 7, (4), 2805-2809.
7. Braia, N.; Merabet-Khelassi, M.; Aribi-Zouioueche, L. *Chirality* **2018,** 30, (12), 1312-1320.
8. Gaide, I.; Makareviciene, V.; Sendzikiene, E.; Kazancev, K. *Catalysts* **2021,** 11, (3), 384.
9. Akbari Gourdani, F.; Ghadam, P.; Heravi, M. M.; Malmir, M. *Journal of the Iranian Chemical Society* **2021**.
10. Pourcel, F.; Jomaa, W.; Puiggali, J. R.; Rouleau, L. *Drying Technology* **2007,** 25, (5), 759-766.
11. Maynard, A. D. *Nature* **2011,** 475, (7354), 31-31.
12. Buzea, C.; Pacheco, I. I.; Robbie, K. *Biointerphases* **2007,** 2, (4), MR17-MR71.
13. The Essential Chemical Industry – online. https://www.essentialchemicalindustry.org/materials-and-applications/nanomaterials.html (accessed April **2021**).
14. Kawamura, G. *Journal of the Ceramic Society of Japan* **2016,** 124, (7), 757-762.
15. Dragoman, M.; Dragoman, D. *Progress in Quantum Electronics* **2008,** 32, (1), 1-41.

16. Stamplecoskie, K. G.; Scaiano, J. C. *Journal of the American Chemical Society* **2010,** 132, (6), 1825-1827.

17. National Nanotechnology Initiative. https://www.nano.gov/nanotech-101/special (accessed April **2021**).

18. Hernando, A.; Crespo, P.; García, M. A. *TheScientificWorldJOURNAL* **2005,** 5, 353792.

19. Ibrahim, I.; Lim, H. N.; Mohd Zawawi, R.; Ahmad Tajudin, A.; Ng, Y. H.; Guo, H.; Huang, N. M. *Journal of Materials Chemistry B* **2018,** 6, (28), 4551-4568.

20. Ge Gao, Y.-W. J., Wei Sun, Fu-Gen Wu. *Chinese Chemical Letters* **2018,** 29, (10), 1475-1485.

21. Deng, Z.; Zhang, Y.; Yue, J.; Tang, F.; Wei, Q. *The Journal of Physical Chemistry B* **2007,** 111, (41), 12024-12031.

22. Zhang, L.; Moralejo, C.; Anderson, W. A. *The Canadian Journal of Chemical Engineering* **2020,** 98, (1), 263-273.

23. Anitha, B.; Khadar, M. A. *Solid State Sciences* **2020,** 108, 106392.

24. Di Paola, A.; Bellardita, M.; Palmisano, L. *Catalysts* **2013,** 3, (1), 36-73.

25. Ramamoorthy, M.; Vanderbilt, D.; King-Smith, R. D. *Physical Review B* **1994,** 49, (23), 16721-16727.

26. Mitsuhashi, T.; Kleppa, O. J. *Journal of the American Ceramic Society* **1979,** 62, (7-8), 356-357.

27. Hadjiivanov, K. I.; Klissurski, D. G. *Chemical Society Reviews* **1996,** 25, (1), 61-69.

28. Sclafani, A.; Palmisano, L.; Schiavello, M. *The Journal of Physical Chemistry* **1990,** 94, (2), 829-832.

29. Dolata, M.; Kedzierzawski, P.; Augustynski, J. *Electrochimica Acta* **1996,** 41, (7), 1287-1293.

30. Karakitsou, K. E.; Verykios, X. E. *The Journal of Physical Chemistry* **1993,** 97, (6), 1184-1189.

31. Li, K.; Peng, J.; Zhang, M.; Heng, J.; Li, D.; Mu, C. *Colloids and Surfaces A: Physicochemical and Engineering Aspects* **2015,** 470, 92-99.

32. Tutorial: Introduction to Solar Radiation. https://www.newport.com/t/introduction-to-solar-radiation (accessed April **2021**).

33. Anpo, M.; Takeuchi, M. *Journal of Catalysis* **2003,** 216, (1), 505-516.

34. Wang, Y. X.; Pan, Z. Y.; Ho, Y. K.; Xu, Y.; Du, A. J. *Nuclear Instruments and Methods in Physics Research Section B: Beam Interactions with Materials and Atoms* **2001,** 180, (1), 251-256.

35. Papp, J.; Shen, H. S.; Kershaw, R.; Dwight, K.; Wold, A. *Chemistry of Materials* **1993,** 5, (3), 284-288.

36. Nada, A. A.; Barakat, M. H.; Hamed, H. A.; Mohamed, N. R.; Veziroglu, T. N. *International Journal of Hydrogen Energy* **2005,** 30, (7), 687-691.

37. Tsydenov, D. E.; Parmon, V. N.; Vorontsov, A. V. *International Journal of Hydrogen Energy* **2012,** 37, (15), 11046-11060.

38. Liu, S. X.; Qu, Z. P.; Han, X. W.; Sun, C. L. *Catalysis Today* **2004,** 93-95, 877-884.

39. Adachi, K.; Ohta, K.; Mizuno, T. *Solar Energy* **1994,** 53, (2), 187-190.

40. Chen, X.; Liu, L.; Yu, P. Y.; Mao, S. S. *Science* **2011,** 331, (6018), 746-750.

41. Qiu, J.; Li, S.; Gray, E.; Liu, H.; Gu, Q.-F.; Sun, C.; Lai, C.; Zhao, H.; Zhang, S. *The Journal of Physical Chemistry C* **2014,** 118, (17), 8824-8830.

42. Boccaccini, A. R.; Zhitomirsky, I. *Current Opinion in Solid State and Materials Science* **2002,** 6, (3), 251-260.

43. Besra, L.; Liu, M. *Progress in Materials Science* **2007,** 52, (1), 1-61.

44. Narayan, M. R.; Raturi, A. *International Journal of Materials Engineering Innovation* **2012,** 3, (1), 17-31.

45. Chen, X. *Chinese Journal of Catalysis* **2009,** 30, (8), 839-851.

46. Yu, J. C.; Yu, J.; Ho, W.; Zhang, L. *Chemical Communications* **2001**, (19), 1942-1943.

47. Zhu, Y.-J.; Chen, F. *Chemical Reviews* **2014,** 114, (12), 6462-6555.

48. Jr, M. J. C. *Future Medicinal Chemistry* **2010,** 2, (2), 151-155.

49. Kim, C.-S.; Moon, B. K.; Park, J.-H.; Choi, B.-C.; Seo, H.-J. *Journal of Crystal Growth* **2003,** 257, (3), 309-315.

50. Feng, X.; Zhai, J.; Jiang, L. *Angewandte Chemie International Edition* **2005,** 44, (32), 5115-5118.

51. Alexandrescu, R.; Morjan, I.; Scarisoreanu, M.; Birjega, R.; Popovici, E.; Soare, I.; Gavrila-Florescu, L.; Voicu, I.; Sandu, I.; Dumitrache, F.; Prodan, G.; Vasile, E.; Figgemeier, E. *Thin Solid Films* **2007,** 515, (24), 8438-8445.

52. Livage, J.; Henry, M.; Sanchez, C. *Progress in Solid State Chemistry* **1988,** 18, (4), 259-341.

53. Tseng, T. K.; Lin, Y. S.; Chen, Y. J.; Chu, H. *International Journal of Molecular Sciences* **2010,** 11, (6), 2336-2361.

54. Ohtani, B.; Prieto-Mahaney, O. O.; Li, D.; Abe, R. *Journal of Photochemistry and Photobiology A: Chemistry* **2010,** 216, (2), 179-182.

55. Kuznetsov, V. N.; Serpone, N. *The Journal of Physical Chemistry C* **2009,** 113, (34), 15110-15123.

56. Choi, J.; Park, H.; Hoffmann, M. R. *The Journal of Physical Chemistry C* **2010,** 114, (2), 783-792.

57. Stakheev, A. Y.; Shulga, Y. M.; Gaidai, N. A.; Telegina, N. S.; Tkachenko, O. P.; Kustov, L. M.; Minachev, K. M. *Mendeleev Communications* **2001,** 11, (5), 186-188.

58. Mullins, L.; Sullivan, J. A. *Topics in Catalysis* **2020,** 63, 1434–1445.

59. Pongthawornsakun, B.; Kaewsuanjik, P.; Kittipreechakun, P.; Ratova, M.; Kelly, P.; Mekasuwandumrong, O.; Praserthdam, P.; Panpranot, J. *Catalysis Today* **2019,** 358, 51-59.

60. Nagaraj, G.; Mohammed, M. K. A.; Abdulzahraa, H. G.; Sasikumar, P.; Karthikeyan, S.; Tamilarasu, S. *Applied Physics A* **2021,** 127, (4), 269.

61. Saha, S.; Victorious, A.; Soleymani, L. *Electrochimica Acta* **2021,** 380, 138154.

62. Dadsetan, S.; Farshidfar, F.; Baghshahi, S.; Rezaei, M. *Asia-Pacific Journal of Chemical Engineering* **2020,** 15, (3), e2432.

63. Ren, L.; Li, Y.; Liu, H.; Mao, M.; Lan, L.; Zhao, X. *ACS Applied Energy Materials* **2020,** 3, (8), 7920-7930.

64. Tan, H.; Zhao, Z.; Niu, M.; Mao, C.; Cao, D.; Cheng, D.; Feng, P.; Sun, Z. *Nanoscale* **2014,** 6, (17), 10216-10223.

65. Cronemeyer, D. C. *Physical Review* **1959,** 113, (5), 1222-1226.

66. Leshuk, T.; Parviz, R.; Everett, P.; Krishnakumar, H.; Varin, R. A.; Gu, F. *ACS Applied Materials & Interfaces* **2013,** 5, (6), 1892-1895.

67. Lu, H.; Zhao, B.; Pan, R.; Yao, J.; Qiu, J.; Luo, L.; Liu, Y. *RSC Advances* **2014,** 4, (3), 1128-1132.

68. Lu, Z.; Yip, C.-T.; Wang, L.; Huang, H.; Zhou, L. *ChemPlusChem* **2012,** 77, (11), 991-1000.

69. Wei, S.; Wu, R.; Xu, X.; Jian, J.; Wang, H.; Sun, Y. *Chemical Engineering Journal* **2016,** 299, 120-125.

70. Kubaschewski, O.; Dench, W. A. *Acta Metallurgica* **1955,** 3, (4), 339-346.

71. Wang, Z.; Yang, C.; Lin, T.; Yin, H.; Chen, P.; Wan, D.; Xu, F.; Huang, F.; Lin, J.; Xie, X.; Jiang, M. *Energy & Environmental Science* **2013,** 6, (10), 3007-3014.

72. Zhu, G.; Lin, T.; Lü, X.; Zhao, W.; Yang, C.; Wang, Z.; Yin, H.; Liu, Z.; Huang, F.; Lin, J. *Journal of Materials Chemistry A* **2013,** 1, (34), 9650-9653.

73. Sinhamahapatra, A.; Jeon, J.-P.; Yu, J.-S. *Energy & Environmental Science* **2015,** 8, (12), 3539-3544.

74. Nguyen, T.-D.; Li, J.; Lizundia, E.; Niederberger, M.; Hamad, W. Y.; MacLachlan, M. J. *Advanced Functional Materials* **2019,** 29, (40), 1904639.

75. Wajid Shah, M.; Zhu, Y.; Fan, X.; Zhao, J.; Li, Y.; Asim, S.; Wang, C. *Scientific Reports* **2015,** 5, (1), 15804.

76. Kang, Q.; Cao, J.; Zhang, Y.; Liu, L.; Xu, H.; Ye, J. *Journal of Materials Chemistry A* **2013,** 1, (18), 5766-5774.

77. Chen, S.; Xiao, Y.; Wang, Y.; Hu, Z.; Zhao, H.; Xie, W. *Nanomaterials* **2018,** 8, (4), 245.

78. Yang, Y.; Liao, J.; Li, Y.; Cao, X.; Li, N.; Wang, C.; Lin, S. *RSC Advances* **2016,** 6, (52), 46871-46878.

79. Yan, Y.; Hao, B.; Wang, D.; Chen, G.; Markweg, E.; Albrecht, A.; Schaaf, P. *Journal of Materials Chemistry A* **2013,** 1, (46), 14507-14513.

80. Chen, X.; Zhao, D.; Liu, K.; Wang, C.; Liu, L.; Li, B.; Zhang, Z.; Shen, D. *ACS Applied Materials & Interfaces* **2015,** 7, (29), 16070-16077.

81. Wang, Z.; Yang, C.; Lin, T.; Yin, H.; Chen, P.; Wan, D.; Xu, F.; Huang, F.; Lin, J.; Xie, X.; Jiang, M. *Advanced Functional Materials* **2013,** 23, (43), 5444-5450.

82. Tian, M.; Mahjouri-Samani, M.; Eres, G.; Sachan, R.; Yoon, M.; Chisholm, M. F.; Wang, K.; Puretzky, A. A.; Rouleau, C. M.; Geohegan, D. B.; Duscher, G. *ACS Nano* **2015,** 9, (10), 10482-10488.

83. Cai, J.; Wang, Y.; Zhu, Y.; Wu, M.; Zhang, H.; Li, X.; Jiang, Z.; Meng, M. *ACS Applied Materials & Interfaces* **2015,** 7, (45), 24987-24992.

84. Haidry, A. A.; Schlosser, P.; Durina, P.; Mikula, M.; Tomasek, M.; Plecenik, T.; Roch, T.; Pidik, A.; Stefecka, M.; Noskovic, J.; Zahoran, M.; Kus, P.; Plecenik, A. *Central European Journal of Physics* **2011,** 9, (5), 1351-1356.

85. An, H. R.; Park, S. Y.; Kim, H.; Lee, C. Y.; Choi, S.; Lee, S. C.; Seo, S.; Park, E. C.; Oh, Y. K.; Song, C. G.; Won, J.; Kim, Y. J.; Lee, J.; Lee, H. U.; Lee, Y. C. *Scientific Reports* **2016,** 6.

86. Yuan, X.; Wang, X.; Liu, X.; Ge, H.; Yin, G.; Dong, C.; Huang, F. *ACS Applied Materials & Interfaces* **2016,** 8, (41), 27654-27660.

87. Teng, F.; Li, M.; Gao, C.; Zhang, G.; Zhang, P.; Wang, Y.; Chen, L.; Xie, E. *Applied Catalysis B: Environmental* **2014,** 148-149, 339-343.

88. Wang, H.; Lin, T.; Zhu, G.; Yin, H.; Lü, X.; Li, Y.; Huang, F. *Catalysis Communications* **2015,** 60, 55-59.

89. Wang, C.-C.; Chou, P.-H. *Nanotechnology* **2016,** 27, (32), 325401.

90. Zhang, X.; Cresswell, M., Chapter 1 - Materials for Inorganic Controlled Release Technology. In *Inorganic Controlled Release Technology*, Zhang, X.; Cresswell, M., Eds. Butterworth-Heinemann: Boston, **2016**; pp 1-16.

91. Zheng, J.; Liu, L.; Ji, G.; Yang, Q.; Zheng, L.; Zhang, J. *ACS Applied Materials & Interfaces* **2016,** 8, (31), 20074-20081.

92. Miao, Z.; Wang, G.; Li, L.; Wang, C.; Zhang, X. *Journal of Materials Science* **2019,** 54, (23), 14320-14329.

93. Bi, Q.; Huang, X.; Dong, Y.; Huang, F. *Catalysis Letters* **2020,** 150, (5), 1346-1354.

94. Wang, Y.; Qian, G.; Xu, Q.; Zhang, H.; Shen, F.; Luo, L.; Yin, S. *Applied Catalysis B: Environmental* **2021,** 286, 119881.

95. Liu, N.; Schneider, C.; Freitag, D.; Hartmann, M.; Venkatesan, U.; Müller, J.; Spiecker, E.; Schmuki, P. *Nano Letters* **2014,** 14, (6), 3309-3313.

96. Zhou, W.; Li, W.; Wang, J.-Q.; Qu, Y.; Yang, Y.; Xie, Y.; Zhang, K.; Wang, L.; Fu, H.; Zhao, D. *Journal of the American Chemical Society* **2014,** 136, (26), 9280-9283.

97. Li, G.; Zhang, Z.; Peng, H.; Chen, K. *RSC Advances* **2013,** 3, (29), 11507-11510.

98. Lu, X.; Wang, G.; Zhai, T.; Yu, M.; Gan, J.; Tong, Y.; Li, Y. *Nano Letters* **2012,** 12, (3), 1690-1696.

99. Zhang, C.; Yu, H.; Li, Y.; Fu, L.; Gao, Y.; Song, W.; Shao, Z.; Yi, B. *Nanoscale* **2013,** 5, (15), 6834-6841.

100. Zhu, W.-D.; Wang, C.-W.; Chen, J.-B.; Li, D.-S.; Zhou, F.; Zhang, H.-L. *Nanotechnology* **2012,** 23, (45), 455204.

101. Xia, T.; Zhang, C.; Oyler, N. A.; Chen, X. *Journal of Materials Research* **2014,** 29, (18), 2198-2210.

102. Ren, W.; Yan, Y.; Zeng, L.; Shi, Z.; Gong, A.; Schaaf, P.; Wang, D.; Zhao, J.; Zou, B.; Yu, H.; Chen, G.; Brown, E. M. B.; Wu, A. *Advanced Healthcare Materials* **2015,** 4, (10), 1526-1536.

103. Baker, I., 8 - Magnetic nanoparticle synthesis. In *Nanobiomaterials*, Narayan, R., Ed. Woodhead Publishing: **2018**; pp 197-229.

104. Sugimoto, T.; Wang, Y.; Itoh, H.; Muramatsu, A. *Colloids and Surfaces A: Physicochemical and Engineering Aspects* **1998,** 134, (3), 265-279.

105. Shakeel Akbar, S. K. H., Nasia Azmat, M. Nadeem. *Condensed Matter* **2004**.

106. Itoh, H.; Sugimoto, T. *Journal of Colloid and Interface Science* **2003,** 265, (2), 283-295.

107. Del Monte, F.; Morales, M. P.; Levy, D.; Fernandez, A.; Ocaña, M.; Roig, A.; Molins, E.; O'Grady, K.; Serna, C. J. *Langmuir* **1997,** 13, (14), 3627-3634.

108. LaMer, V. K.; Dinegar, R. H. *Journal of the American Chemical Society* **1950,** 72, (11), 4847-4854.

109. Lefebure, S.; Dubois, E.; Cabuil, V.; Neveu, S.; Massart, R. *Journal of Materials Research* **1998,** 13, (10), 2975-2981.

110. Iida, H.; Takayanagi, K.; Nakanishi, T.; Osaka, T. *Journal of Colloid and Interface Science* **2007,** 314, (1), 274-280.

111. Zhang, L.; Papaefthymiou, G. C.; Ying, J. Y. *Journal of Applied Physics* **1997,** 81, (10), 6892-6900.

112. Ali, A.; Zafar, H.; Zia, M.; Ul Haq, I.; Phull, A. R.; Ali, J. S.; Hussain, A. *Nanotechnol Sci Appl* **2016,** 9, 49-67.

113. Fortin, J.-P.; Wilhelm, C.; Servais, J.; Ménager, C.; Bacri, J.-C.; Gazeau, F. *Journal of the American Chemical Society* **2007,** 129, (9), 2628-2635.

114. Sousa, M. H.; Tourinho, F. A.; Depeyrot, J.; da Silva, G. J.; Lara, M. C. F. L. *The Journal of Physical Chemistry B* **2001,** 105, (6), 1168-1175.

115. Wang, X.; Zhuang, J.; Peng, Q.; Li, Y. *Nature* **2005,** 437, (7055), 121-124.

116. Hyeon, T.; Lee, S. S.; Park, J.; Chung, Y.; Na, H. B. *Journal of the American Chemical Society* **2001,** 123, (51), 12798-12801.

117. Pol, V. G.; Motiei, M.; Gedanken, A.; Calderon-Moreno, J.; Mastai, Y. *Chemistry of Materials* **2003,** 15, (6), 1378-1384.

118. Salazar-Alvarez, G.; Muhammed, M.; Zagorodni, A. A. *Chemical Engineering Science* **2006,** 61, (14), 4625-4633.

119. Wang, W.-W. *Materials Chemistry and Physics* **2008,** 108, (2), 227-231.

120. González-Carreño, T.; Morales, M. P.; Gracia, M.; Serna, C. J. *Materials Letters* **1993,** 18, (3), 151-155.

121. Stein, M.; Wieland, J.; Steurer, P.; Tölle, F.; Mülhaupt, R.; Breit, B. *Advanced Synthesis & Catalysis* **2011,** 353, (4), 523-527.

122. Fakhri, A.; Naghipour, A. *Materials Technology* **2016,** 31, (14), 846-853.

123. Lee, S. W.; Surabhi, S.; Kuchi, R.; Sohn, Y.; Jeong, J.-R. *Journal of Alloys and Compounds* **2019,** 771, 131-139.

124. Rostami, M.; Sharafi, P.; Mozaffari, S.; Adib, K.; Sobhani-Nasab, A.; Rahimi-Nasrabadi, M.; Fasihi-Ramandi, M.; Ganjali, M. R.; Badiei, A. *Journal of Materials Science: Materials in Electronics* **2021,** 32, (5), 5457-5472.

125. Kargar, H.; Ghahramaninezhad, M.; Shahrak, M. N.; Balula, S. S. *Microporous and Mesoporous Materials* **2021,** 317, 110992.

126. Chen, X.; Zhang, Y.; Zhang, H.; Zhang, L.; Liu, L.; Cao, Y.; Ran, H.; Tian, J. *Journal of Nanobiotechnology* **2021,** 19, (1), 82.

127. Song, R.; Ruan, M.; Dai, J.; Xue, W. *Journal of Materials Chemistry B* **2021,** 9, (10), 2494-2504.

128. Anirudhan, T. S.; Christa, J. *Journal of Drug Delivery Science and Technology* **2020,** 55, 101476.

Chapter 2
Catalyst Preparation

2.1 Black TiO_2 Photocatalysts

2.1.1 Introduction

As explained in the previous chapter, the ultimate goal of black TiO_2 catalyst is to harvest the visible light for useful applications[1-6]. Before using it, it must be synthesized. Black TiO_2 catalysts can be synthesized by many methods. Here, sodium borohydride and ethanol are selected as reducing agents for making black TiO_2 catalysts separately. Detailed experimental processes and conditions will be shown in this chapter.

Sodium borohydride and ethanol synthesis of black TiO_2 catalysts, were both characterized by an UV-vis diffuse reflectance spectrometer to evaluate light absorption ability and band gap. X-ray diffractometry was used to identify the crystalline type and size for ethanol reduced black TiO_2 only. X-ray photoelectron spectrometry was also utilized to determine the elemental oxidation state and relative abundance of each state on the surface of ethanol-reduced black TiO_2 catalysts. All characterization will be discussed in this chapter.

2.1.2 Experimental

2.1.2.1 Preparation of Rutile TiO_2

Rutile TiO_2 was obtained by heating Degussa P25 titanium dioxide (85% anatase and 15% rutile) in the muffle furnace at 700 °C for 3 hours under air. As-obtained rutile TiO_2 was directly used without any further treatment.

2.1.2.2 Preparation of Black TiO_2 by Sodium Borohydride

$NaBH_4$ (0.5 g) and P25 (1 g) were mixed and ground thoroughly in a stone mortar. Then the mixture was put into tubular furnace (OTF-1200X-5-III-SF) for blackening treatment under argon. Detailed sequence is as follows: initial temperature was set to 25 °C; then temperature increase to 500 °C with the rate of 5 °C/min, and then maintained at

500 °C for 8 hours during which the sample compartment was sealed. After heat treatment, sample cooled to room temperature naturally.

2.1.2.3 Preparation of Black TiO_2 by Ethanol

Black anatase and rutile TiO_2 made from ethanol reduction was prepared following Chen's method[7]. Absolute ethanol (10 mL) was mixed with 0.5 g of P25 or rutile 0.5 g of TiO_2 in two separate scintillation vials stirring 10 minutes by using magnetic stirrers to form a milky-white suspension. Then the mixtures were transferred into two quartz crucibles and put into a tubular furnace (OTF-1200X-III-SF), followed by purging system with argon. Detailed heat treatment is as follows: initial temperature was set to 25 °C; then temperature increase to 400 °C with the rate of 5 °C/min, and then maintained at 400 °C for 3 hours during which the sample compartment was sealed. After heat treatment, temperature cooled down to 50 °C with the rate of 5 °C/min. Finally, catalysts were cooled to room temperature naturally without any further treatment.

2.1.2.4 Preparation of Re-whited TiO_2

Re-whitening process is simple. Ethanol-reduced black TiO_2 (both anatase and rutile) was heated at 400 °C for 2 hours in a muffle under air to obtain re-whited anatase and rutile TiO_2.

2.1.2.5 Characterization

UV-vis diffuse reflectance (DR) spectra were collected using an Agilent Cary 100 Universal Measurement Spectrophotometer. A Rigaku Ultima IV Diffractometer with Cu Kα X-ray source (λ= 0.154 nm) was used to measure powder X-ray diffraction (XRD) patterns at room temperature. The X-ray photoelectron (XPS) spectra were collected at Queens University using Al Kα radiation at 1486.69 eV (150 W, 15 kV), charge neutralizer and a delay-line detector consisting of three multi-channel plates.

2.1.3 Results and Discussion

2.1.3.1 UV-vis Diffuse Reflectance Spectrum

The light absorption property of all black TiO_2 prepared from two different methods are compared by UV-vis DR spectra. As shown in Figure 2.1, P25 can only absorb the light in the ultraviolet region. But $NaBH_4$ and ethanol-reduced black TiO_2 both exhibit better light absorption ability in terms of visible and UV light absorption. Meanwhile,

ethanol reduced black TiO_2 have higher F(R) value than that of $NaBH_4$ reduced black TiO_2 of the light with the wavelength longer than 325 nm. Moreover, the synthetic procedure for $NaBH_4$ reduced black TiO_2 is more complicated than ethanol reduced black TiO_2's. Hence ethanol was selected as the reducing agent for making all black TiO_2 catalysts for the rest of this reseach.

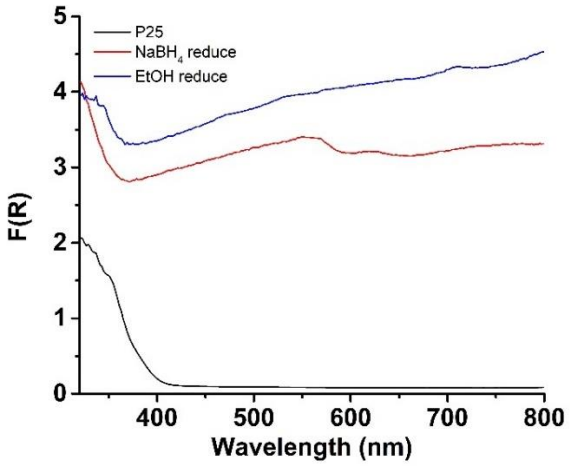

Figure 2.1. UV-vis diffuse reflectance spectra of P25, $NaBH_4$ and ethanol reduced black TiO_2.

In order to simplify the names of all black TiO_2 catalysts, a-Ti, r-Ti, ba-Ti, br-Ti, wa-Ti, and wr-Ti are applied to abbreviate white anatase TiO_2 (P25), white rutile TiO_2, black anatase TiO_2, black rutile TiO_2, re-whited anatase TiO_2, and re-whited rutile TiO_2, respectively. As can be seen in Figure 2.2 (a), all samples display great UV light absorption. But a-Ti is the weakest absorber, which indicate heat and blackening treatment can really enhance the UV light absorption properties of anatase and rutile TiO_2 catalysts. In terms of light absorption in the visible region, only ba-Ti, and br-Ti can absorb light in this region. Moreover, ba-Ti has higher F(R) value than br-Ti, indicating that ba-Ti can absorb more light than br-Ti in the visible region, which also can be confirm with the color of ba-Ti (black) and br-Ti (grey) in Figure 2.3. One interpretation of this phenomenon could be explained as different crystalline stability of anatase and rutile phases. During the blackening treatment, the more stable TiO_2 (rutile) is harder to be reduced by ethanol than anatase TiO_2, which makes anatase TiO_2 being reduced more, resulting in higher visible light absorption of black anatase TiO_2 than black rutile TiO_2. By comparing black and re-whited TiO_2, visible light absorption ability and black color of ba-Ti and br-Ti are eliminated by heating under air for just 2 h. The spectra of wr-Ti and r-Ti even overlap

with each other. This evidence shows that the blackening process is reversible and only occurs on the surface of the catalysts. It is interesting to note that the UV light absorption of anatase TiO_2 (from a-Ti to wa-Ti) change dramatically after blackening and re-whitening treatment. This is possibly due to the less thermal stability of anatase phase.

Tauc plots of all catalysts are also shown in the Figure 2.2 (b) and (c). a-Ti has the band gap of 3.10 eV, followed by wa-Ti with 3.06 eV, indicating that re-whitening treatment can partially restore the energy level structure from ba-Ti. Meanwhile, the low light reflectance of ba-Ti may result in the inaccuracy of Tauc plot, which makes the band gap of ba-Ti unable to be determined. But from Figure 2.2 (b), it is believed that ba-Ti has smaller band gap than both a-Ti and wa-Ti. As we can see in Figure 2.2 (c), r-Ti and wr-Ti have almost the same curve from 2 to 4 eV, resulting a band gap of 3.03 eV. While 3.09 eV is found to be the band gap of br-Ti. Generally, black TiO_2 should have smaller band gap than the white ones in order to absorb the light in the visible region. The reason why we a got larger value for br-Ti is possibly due to the different onsets of r-Ti and br-Ti curves.

This is also a direct evidence of proving our blackening treatment is reversible.

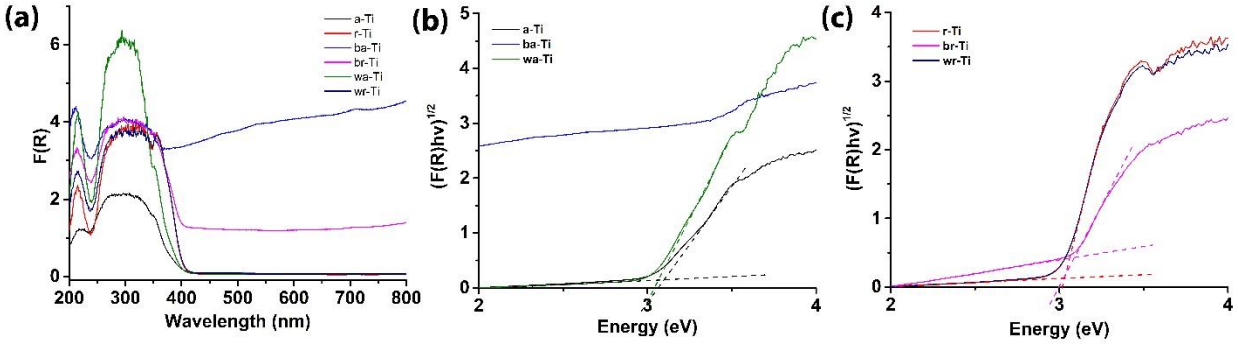

Figure 2.2. UV-vis diffuse reflectance spectra (a) and Tauc plots (b and c) of a-Ti, r-Ti, ba-Ti, br-Ti, wa-Ti, and wr-Ti.

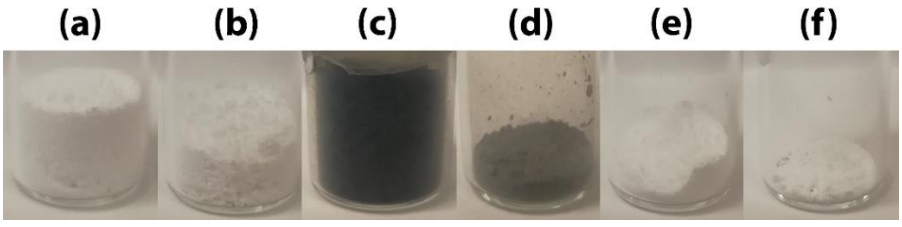

Figure 2.3. Photographs of a-Ti (a), r-Ti (b), ba-Ti (c), br-Ti (d), wa-Ti (e), and wr-Ti (f).

2.1.3.2 Powder X-ray Diffraction Pattern

The crystalline structures of all catalysts are characterized by XRD analysis. On the left side of Figure 2.4, the huge and sharp peak at 25.2 degree indicates that there is a strong signal of (101) plane from anatase TiO_2. Other planes from anatase TiO_2 like (004), (200), (105) and (204) can be also seen in the pattern[8]. Other than that, a peak at 27.4 degrees reveals that rutile phase also exists in a-Ti, ba-Ti, and wa-Ti. On the right side of Figure 2.4, the intensity of rutile (110) plane becomes much higher than that of anatase (101) plane[9], which means that the main part of the catalyst is successfully transformed into rutile phase from anatase phase after baking under air. All peaks' positions do not shift, and peak intensities merely change after blackening and re-whitening treatment indicating synthetic methods in this dissertation does not change the phase composition of the catalysts.

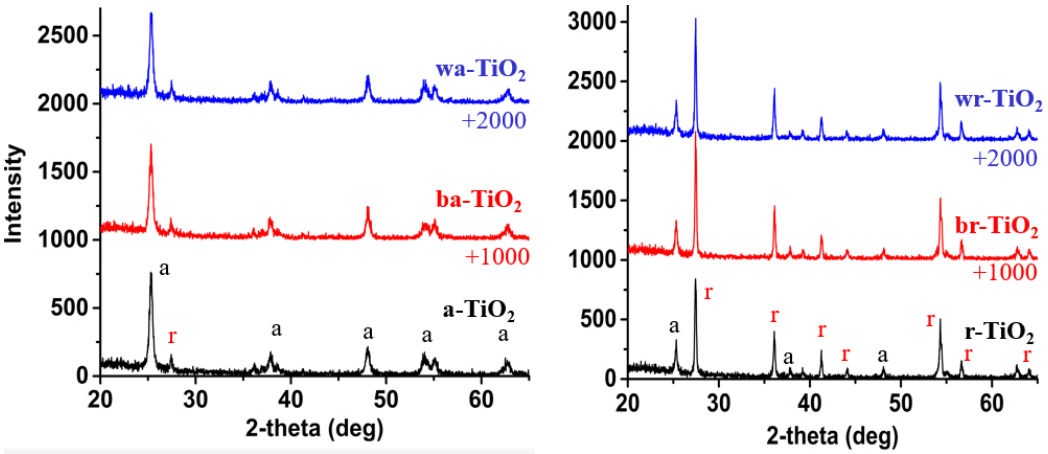

Figure 2.4. PXRD patterns of a-Ti, r-Ti, ba-Ti, br-Ti, wa-Ti, and wr-Ti. Letters a and r on the peaks represent anatase and rutile.

The precise phase compositions and crystalline sizes of all catalysts are also calculated using Scherer equation[10] and tabulated in Table 2.1. All anatase group or rutile group of TiO_2 have similar phase compositions and crystalline sizes. Although blackening treatment changes both parameters a little bit, the re-whitening process will turn them back to pristine a-Ti and r-Ti. These results further prevail that not only the treatment in our methods barely changes phase composition of catalyst, but also the blackening process is totally reversible.

Table 2.1. Phase compositions and crystalline sizes of all catalysts.

Sample	Anatase %	Rutile %	Anatase Size (nm)	Rutile Size (nm)
a-Ti	83.19	16.81	22.49	N/A
ba-Ti	78.74	21.26	43.49	N/A
wa-Ti	81.75	18.25	21.40	N/A
r-Ti	17.82	82.18	N/A	44.34
br-Ti	20.41	79.59	N/A	60.09
wr-Ti	18.54	81.46	N/A	47.52

Some crystalline sizes are not available because of low content of relative phase.

2.1.3.3 X-ray Photoelectron Spectrum

XPS spectra and CasaXPS software were chosen to analyze the oxidation state and the relative abundance of each element on the surface of catalyst. All binding energies are corrected to the C 1s peak at 284.8 eV. A Shirley baseline is also selected for fitting.

Figure 2.5, Figure 2.7 (a) and Figure 2.7 (b) show the XPS spectra of oxygen and titanium before and after blackening and re-whitening treatment of anatase TiO_2. There are 2 peaks in the oxygen 1s HR XPS spectra. The major one is attributed to the Ti^{4+}-O bond, and the broad peak is from surface -OH species. The major and broad peaks locate at 529.8 and 530.8 eV in both a-Ti and wa-Ti, but the peaks shifted to 530.6 eV and 531.6 in ba-Ti, which indicates the chemical environment of surface oxygen is changed after blackening treatment, and can be restored by re-whitening process. In titanium 2p XPS spectrum of a-Ti, three peaks located at 464.3, 458.5 and 457.0 eV are attributed from Ti^{4+} $2p_{1/2}$, Ti^{4+} $2p_{3/2}$, and Ti^{3+} $2p_{3/2}$, respectively. The spin orbit splitting (ΔBE) calculated from Ti^{4+} $2p_{1/2}$ and Ti^{4+} $2p_{3/2}$ (ΔBE = BE (Ti^{4+} $2p_{1/2}$) – BE (Ti^{4+} $2p_{3/2}$)) is 5.8 eV, which matches the regular spin orbit splitting in titanium oxides. The same spin orbit splitting can be obtained in Ti 2p XPS spectrum of wa-Ti. But for ba-Ti, peaks of Ti^{4+} $2p_{1/2}$, Ti^{4+} $2p_{3/2}$, and Ti^{3+} $2p_{3/2}$ shifted to 465.1, 459.3, and 457.8 eV with the same spin orbit splitting as a-Ti, which agrees with the change in the chemical environment detected also from the O1s HR XPS.

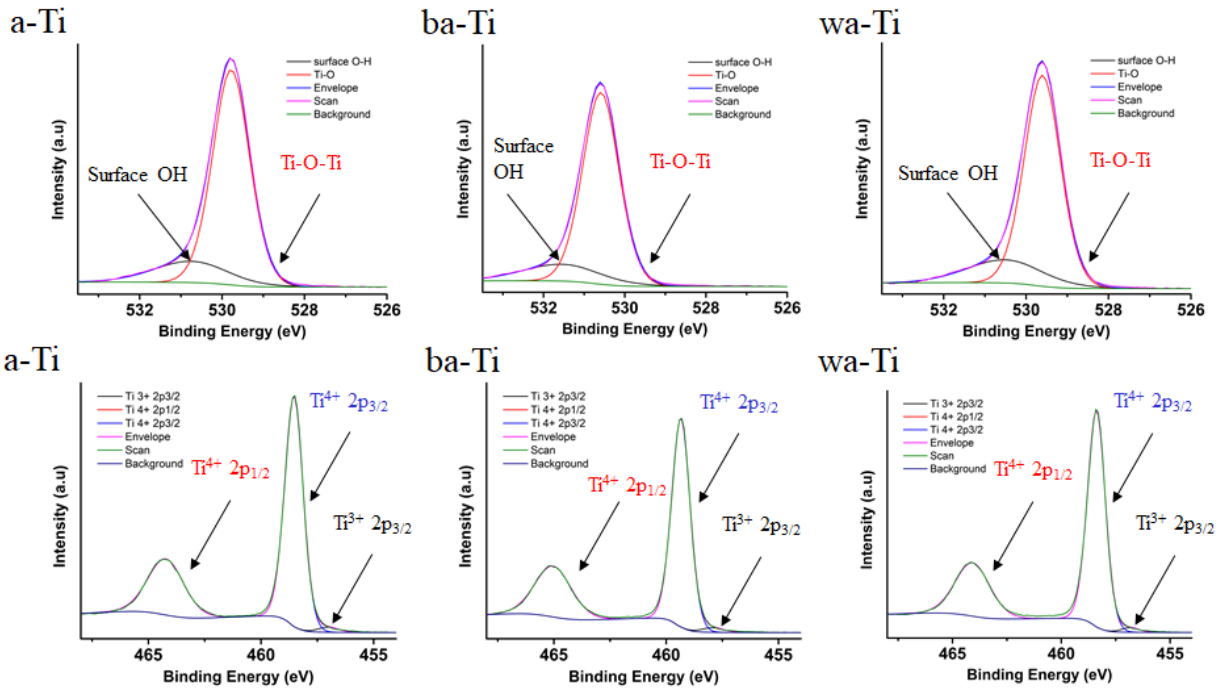

Figure 2.5. Oxygen 1s and titanium 2p HR XPS spectra of a-Ti, ba-Ti, and wa-Ti.

Similar results were found for all rutile TiO_2 samples. Same peak positions of all Ti 2p and OH peaks can be obtained in Figure 2.6, Figure 2.7 (c) and Figure 2.7 (d) for r-Ti and wr-Ti catalysts. Only the peak from Ti^{4+}-O bond shifted to lower binding energy of 529.7 eV. Then similar shift was also discovered in Liu's paper[11]. For O 1s peaks in br-Ti, peaks from Ti^{4+}-O bond and surface -OH species are found at 530.5 and 531.5 eV with the same shift value in anatase catalysts. And all Ti 2p peaks can be found at the same positions as those in anatase catalysts.

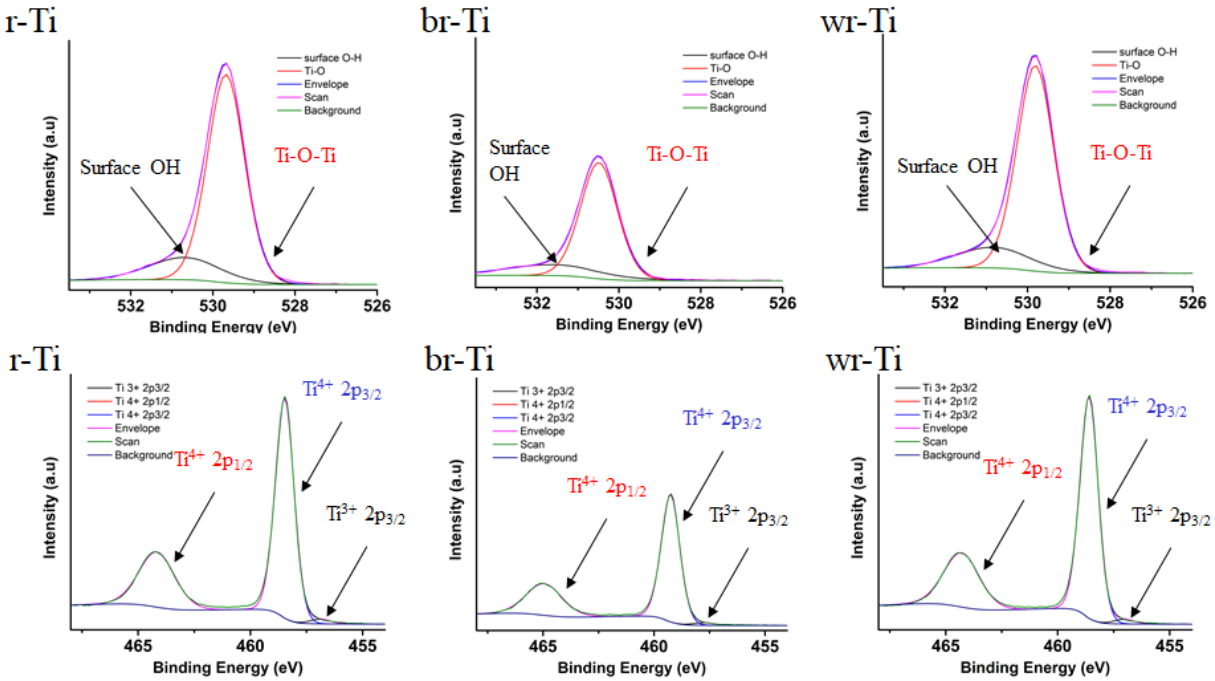

Figure 2.6. Oxygen and titanium HR XPS spectra of r-Ti, br-Ti, and wr-Ti.

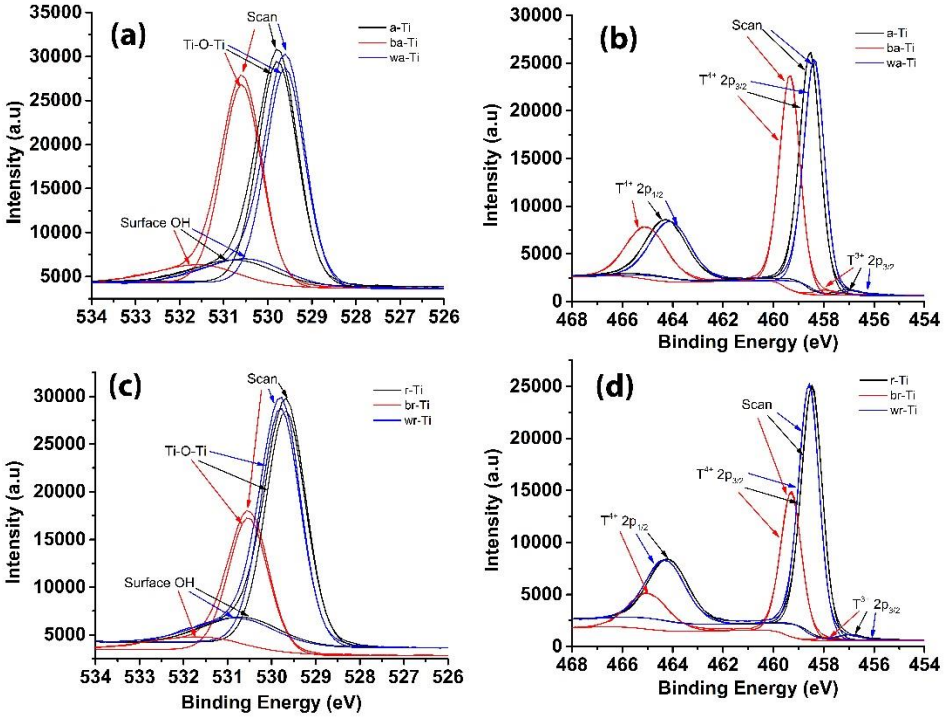

Figure 2.7. Overlapped oxygen (a and c) and titanium (b and d) XPS spectra fitting curves of a-Ti, ba-Ti, wa-Ti, r-Ti, br-Ti, and wr-Ti.

Surprisingly, the titanium 2p signals shifted to higher binding energy after blackening treatment. which is against common sense - 'higher charge results in higher binding energy' in XPS. In the white TiO_2, titanium ions are Ti^{4+}, while a tiny portion of Ti^{4+} is reduced to Ti^{3+} in the black TiO_2. This ideally should make binding energies in white TiO_2 higher than those in black TiO_2. But the reason why this unusual phenomenon appears remains unclear.

XPS is known as a surface characterization technology. From Figure 2.7, peak intensities of black TiO_2 catalysts can be found lower than those of white ones. This could be attributed from the larger size of black TiO_2 catalysts, which gives the smaller surface area of the catalyst resulting in the lower signal intensities in XPS spectra.

Relative abundance of each element on the surface was gained from software fitting results. As shown in Table 2.2, blackening treatment slightly enhanced the abundance of surface -OH and Ti^{3+} species, which agrees with the statement that surface -OH and Ti^{3+} species are the reason why black TiO_2 is black[12-16]. Furthermore, despite of the negligible differences between titanium 2p peak, black and white TiO_2 catalysts exhibit totally different colors. This shows that a very small surface modification can lead to dramatic property change in black TiO_2 materials.

Table 2.2. Relative abundance of each element on the surface of catalysts.

Sample	Ti-O Bond (%)	Surface -OH (%)	Ti^{4+} $2p_{3/2}$	Ti^{4+} $2p_{1/2}$	Ti^{3+} $2p_{3/2}$
a-Ti	83.4	16.6	66.9	31.5	1.6
ba-Ti	81.2	18.8	66.3	32.0	1.7
wa-Ti	84.1	15.9	66.7	31.9	1.4
r-Ti	82.9	17.1	66.6	31.9	1.5
br-Ti	80.4	19.6	66.6	31.8	1.6
wr-Ti	83.1	16.9	66.9	31.6	1.5

2.1.4 Conclusion

In this part, sodium borohydride and ethanol reduced black TiO_2 catalysts were successfully synthesized and characterized by UV-vis diffuse reflectance spectrum. Considering the better light absorption ability and facile synthetic route of ethanol reduced

black TiO_2, sodium borohydride was no longer used in later experiments. UV-vis DR spectra show that black TiO_2 has stronger UV and visible light absorption than white TiO_2, especially for anatase samples. XRD patterns and XPS spectra all show that the blackening treatment and re- whitening process can only change the surface of TiO_2. All three characterizations prove that the blackening process is reversible.

2.2 Metal oxide coupled Magnetic TiO_2 Catalyst

2.2.1 Introduction

The separation of catalyst from reaction matrix has been a big challenge for a long time. Although heterogeneous catalyst makes the separation possible by centrifugation, it still needs trained personnel to operate. The introduction of magnetic part into heterogeneous catalyst can enable the easy separation by an external magnetic field[17], which simplifies the separation process and lower the labor costs.

In this section, the sol-gel method was selected to make magnetic catalysts. Blackening treatment was also applied in this part to make the catalysts have better light absorption abilities. For characterization, UV-vis diffuse reflectance spectra, Raman spectra, scanning electron microscopy (SEM) images and energy-dispersive X-ray (EDS) elemental mapping analysis are used to determine the light absorption capability, crystalline type, structure, and elemental distribution of catalysts, respectively.

2.2.2 Experimental

2.2.2.1 Preparation of Magnetic Fe_2O_3 Catalyst

Shakeel's method[18] was selected after some small modifications: 25 ml of 0.1 M $Fe(NO_3)_3 \bullet 9H_2O$ (Aldrich 98%) was added dropwisely into 100 ml of 0.1 M monohydrated citric acid (Aldrich 98%) solution under vigorous magnetic stirring. Then the solution was heated to a temperature of 90 °C, while maintaining vigorous stirring until the gel was formed and the water contained was evaporated. The gel obtained was dried in an oven overnight followed by grinding into a fine powder before calcination. Finally, the dry gel was transferred into muffle furnace and heated at 400 °C for 3 hours to remove carbon residues. As-synthesized catalyst is called mFe (m represents magnetic).

2.2.2.2 Preparation of Magnetic Fe_2O_3@TiO_2 Catalyst

P25 (0.2 g) was added to the 0.1 M monohydrated citric acid solution prior to adding the iron precursor solution. Other steps are exact the same as magnetic Fe_2O_3 catalyst preparation. As-synthesized catalyst is called mFeTi (Fe:Ti=1:1 by mol).

2.2.2.3 Preparation of Iron/Copper oxide Magnetic TiO_2 Catalyst

A metal precursor solution was made by putting 2.5 mM $Fe(NO_3)_3 \cdot 9H_2O$ and 0.3125 mM $Cu(NO_3)_2 \cdot 2.5H_2O$ into 25 ml of water (final concentration for Fe^{3+} and Cu^{2+} are 0.1 and 0.0125 M, respectively). Replaced iron precursor solution with this metal precursor solution and then followed all steps in part 2.2.2.2 to make iron/copper oxide magnetic TiO_2 catalyst. As-synthesized catalyst is called mCuFeTi (Cu:Fe:Ti=1:8:8 by mol).

2.2.2.4 Preparation of Black Magnetic Catalyst

Magnetic catalyst (0.5 g) was thoroughly ground along with 0.25 g $NaBH_4$. The mixture was then transferred into tubular furnace, followed by heating at 500 °C under argon for 8 hours. Detailed sequence is as follows: initial temperature was set to 25 °C; then temperature increase to 500 °C with the rate of 5 °C/min, and then maintained at 500 °C for 8 hours. After heat treatment, temperature was allowed to cool to room temperature naturally to obtain black magnetic catalysts. As-synthesized catalysts are called b-Ti, b-mFeTi, and b-mCuFeTi.

2.2.2.5 Alternative Method of Preparing Black Magnetic Catalyst

To simplify procedure, dry gel obtained from oven was used to grind with $NaBH_4$ rather than final magnetic catalysts. All other steps are same as steps in part 2.2.2.5. As-synthesized catalysts are called *b-mFeTi and *b-mCuFeTi.

2.2.2.6 Characterization

UV-vis diffuse reflectance (DR) spectra were collected using an Agilent Cary 100 Universal Measurement Spectrophotometer with diluted sample (20% in silica gel). A HORIBA XploRATM Plus Raman Microscope was used to measure the Raman spectra of catalysts. JEOL JSM-7500F field emission scanning electron microscope with carbon tape was selected to collect the scanning electron microscope (SEM) image and energy-dispersive X-ray (EDS) elemental mapping for catalysts.

2.2.3 Results and Discussion

2.2.3.1 UV-vis Diffuse Reflectance Spectrum

UV-vis DR spectra of magnetic and black magnetic catalysts are shown is Figure 2.8. Introducing Fe_2O_3 (green line) and CuO (brown) to TiO_2 system can heavily increase the light absorption in the UV and visible region. Comparing with magnetic Fe_2O_3 alone, the presence of TiO_2 and CuO smooth the F(R) drop around 570 nm and decrease the light absorption in all analyzed range. The evidence confirms that adding Fe_2O_3 and CuO can give the composite TiO_2 catalyst better light absorption properties. Huge differences can also be seen before and after blackening treatment. For mFe and mFeTi, blackening treatment reduces the light absorption in shorter wavelength, but increases longer-wavelength light absorption. Meanwhile, light absorption from 350 to 800 nm is considerably increased by making P25 and mCuFeTi catalyst black. In addition to blackening process, the original color of iron oxide and copper oxide also contributes a lot in the light absorption of catalysts obtained in this chapter.

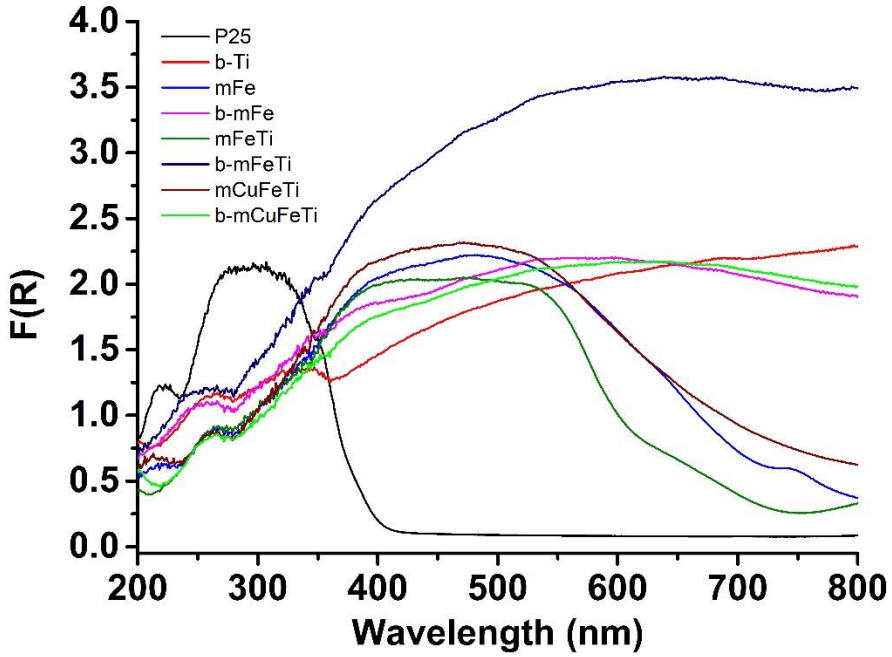

Figure 2.8. UV-vis diffuse reflectance spectra of pristine P25, black TiO_2 (b-Ti), magnetic Fe_2O_3 (mFe), black magnetic Fe_2O_3 (b-mFe), magnetic Fe_2O_3@TiO_2 (mFeTi), black magnetic Fe_2O_3@TiO_2 (b-mFeTi), magnetic CuO@Fe_2O_3@TiO_2 (mCuFeTi), and black magnetic CuO@Fe_2O_3@TiO_2 (b-mCuFeTi).

Two different blackening methods are evaluated using UV-vis DR spectra showing in the Figure 2.9. Both black mFeTi and black mCuFeTi are better than black TiO_2 alone in terms of light absorption ability. Also, both catalysts made from heating dry gel directly have stronger light absorption than catalysts acquired by blackening mFeTi and mCuFeTi. This could be due to the lack of oxygen in blackening process resulting forming carbon black rather than CO_2 when heating the dry gel in the tubular furnace under argon. This statement will also be confirmed by SEM and EDS mapping afterwards.

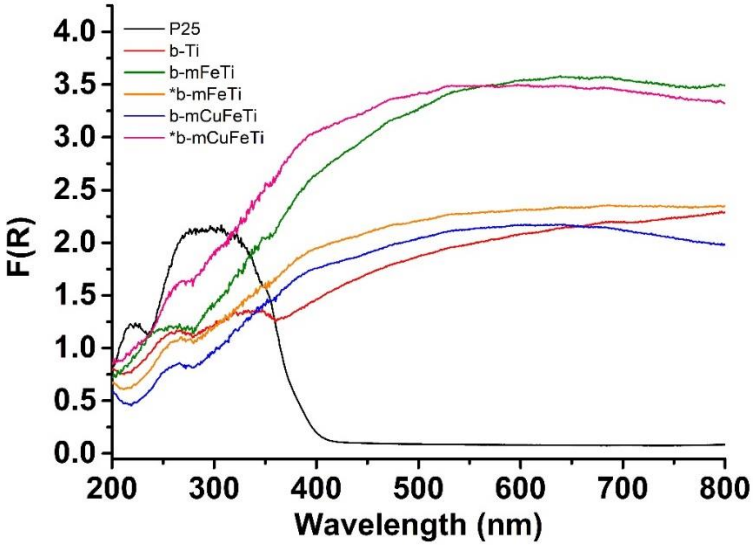

Figure 2.9. UV-vis diffuse reflectance spectra of pristine P25, black TiO_2 (b-Ti), black magnetic Fe_2O_3@TiO_2 (b-mFeTi), *black magnetic Fe_2O_3@TiO_2 (*b-mFeTi), black magnetic CuO@Fe_2O_3@TiO_2 (b-mCuFeTi), and *black magnetic CuO@Fe_2O_3@TiO_2 (*b-mCuFeTi).

The orange color of mFe, mFeTi, and mCuFeTi is attributed to Fe_2O_3, while the black color of b-mFe, b-mFeTi, and b-mCuFeTi can be mainly due to Fe_3O_4 which is reduced during blackening treatment. In the cases of *b-mFeTi and *b-mCuFeTi, the black color can also be from carbon black discussed before.

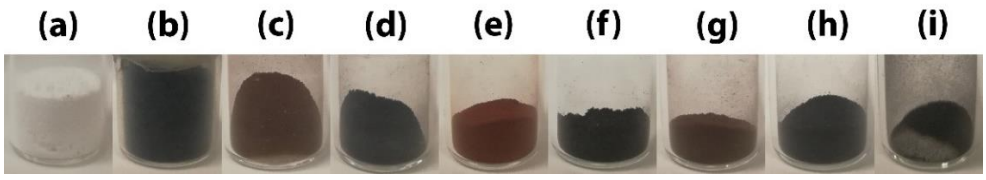

Figure 2.10. Photographs of P25 (a), b-Ti (b), mFe (c), b-mFe (d), mFeTi (e), b-mFeTi (f), mCuFeTi (g), b-mCuFeTi (h), and *b-mFeTi (i).

2.2.3.2 Raman Spectrum

To identify the TiO_2 crystalline phase, Fe and Cu oxides' oxidation states and crystal classes, Raman spectra were collected using 1% power of 768 nm laser with 10x objective lens. As shown in Figure 2.11, all peaks at 143 (E_g), 197 (E_g), 397 (B_{1g}), 516 (A_{1g}+B_{1g}), and 638 (E_g) cm^{-1} can be found in both P25 and b-Ti samples[19], indicating P25 consists mostly of anatase phase and blackening treatment does not change the crystalline phase of P25 TiO_2. Raman spectrum of magnetic Fe_2O_3 in figure 2.12 shows the iron oxide crystalline type is α- Fe_2O_3[20]. After introducing P25 into system, all characteristic peaks from anatase TiO_2 and magnetic Fe_2O_3 can be seen in the mFeTi sample, which means that both TiO_2 and Fe_2O_3 maintain the original phase after synthesis.

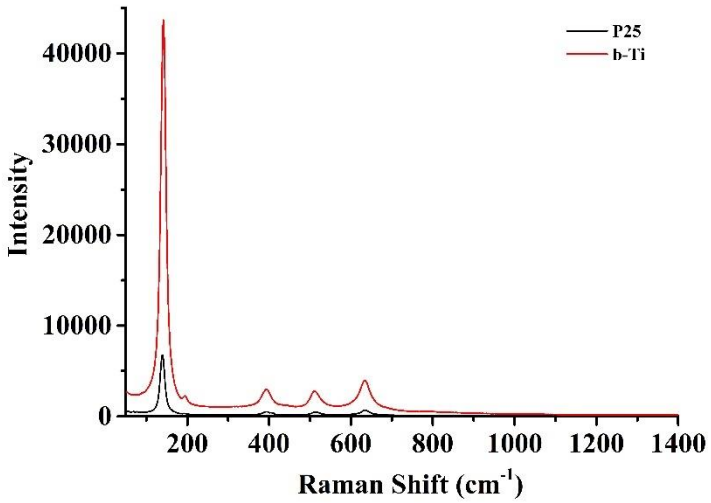

Figure 2.11. Raman spectra of P25 and b-Ti.

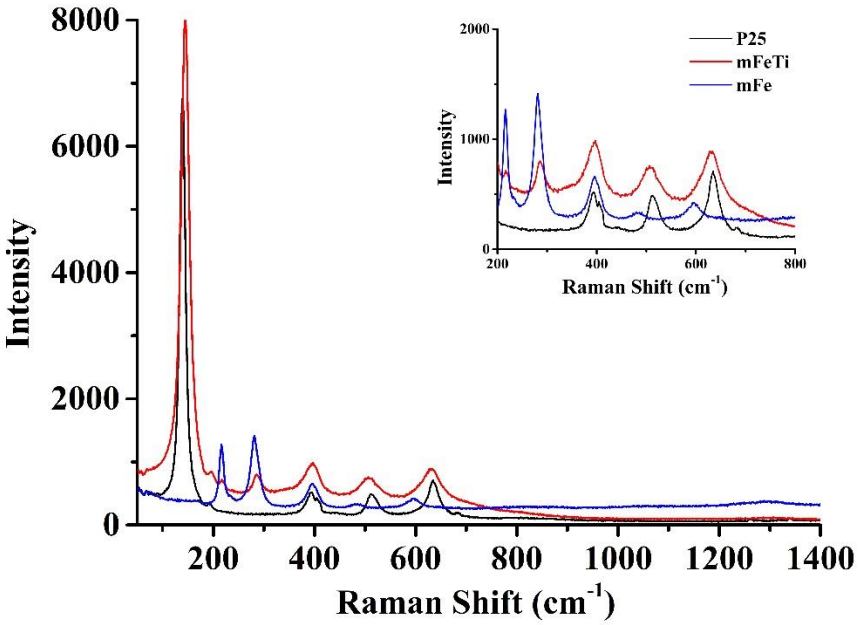

Figure 2.12. Raman spectra of P25, mFe, and mFeTi (inset shows the enlarged spectra from 200 to 800 cm^{-1}).

After doping Cu into mFeTi catalyst, Raman spectrum only shows part of the characteristic peaks from TiO_2 and α-Fe_2O_3 (Figure 2.13 and 2.14). Any characteristic peaks of Cu oxides cannot be found in the spectrum. Hence the presence of Cu could not be confirmed by Raman analysis. The same problem becomes severer in all black catalyst other than b-Ti (Figure 2.14). The reason why Raman spectra do not show characteristic peaks can be the strong light absorption (Figure 2.9) and deep black color (Figure 2.10) of the catalysts, which causes the absorption of Raman signal light by the samples.

The broad peak at around 1350 cm^{-1} can be attributed to Fe_3O_4 according to a published paper from Hatel[21].

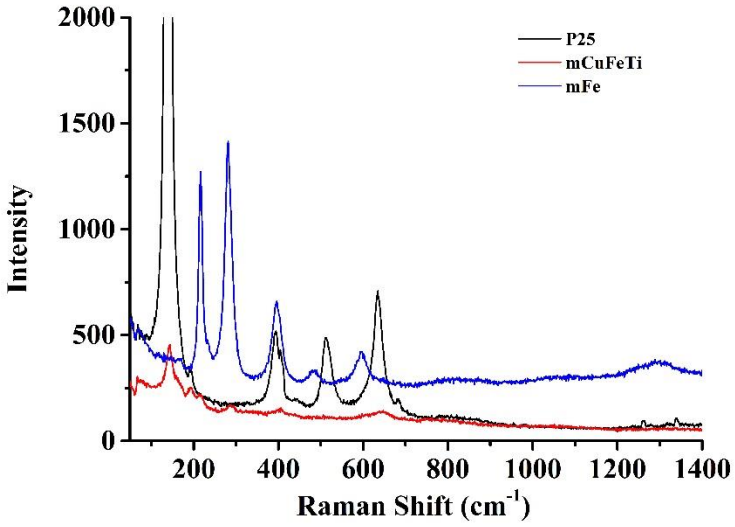

Figure 2.13. Raman spectra of P25, mFe, and mCuFeTi.

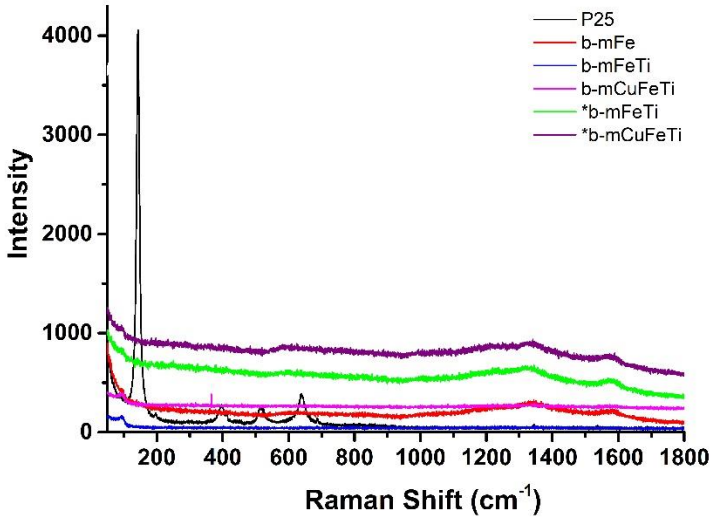

Figure 2.14. Raman spectra of P25, b-Ti, b-mFe, b-mFeTi, b-mCuFeTi, *b-mFeTi, and *b-mCuFeTi.

2.2.3.3 Scanning Electron Microscope and Energy-Dispersive X-ray Elemental Mapping Analysis

To better understand the structures and elemental composition in different area of synthesized catalysts, SEM and EDS elemental mapping will be discussed in this section. A severe agglomeration of pristine P25 can be found in Figure 2.15, which is not

surprisingly matching the results from published papers[22, 23]. Figure 2.16 shows magnetic CuFeTi catalyst has porous chunky structures with a random size distribution from few hundred nanometers to 40 micrometers. After blackening treatment, the size of the catalyst grows, but the porous structure inside of the aggregates is maintained (Figure 2.17). It is interesting to notice that bright spots are showing on the images of b-mCuFeTi catalyst, which will be further discussed in EDS elemental mapping. As a comparison of b-mCuFeTi, *b-mCuFeTi was also imaged by SEM. A covered surface can be found on *b-mCuFeTi catalyst in Figure 2.18, indicating the surface of the catalyst is changed by heating the dry gel directly in the tubular furnace.

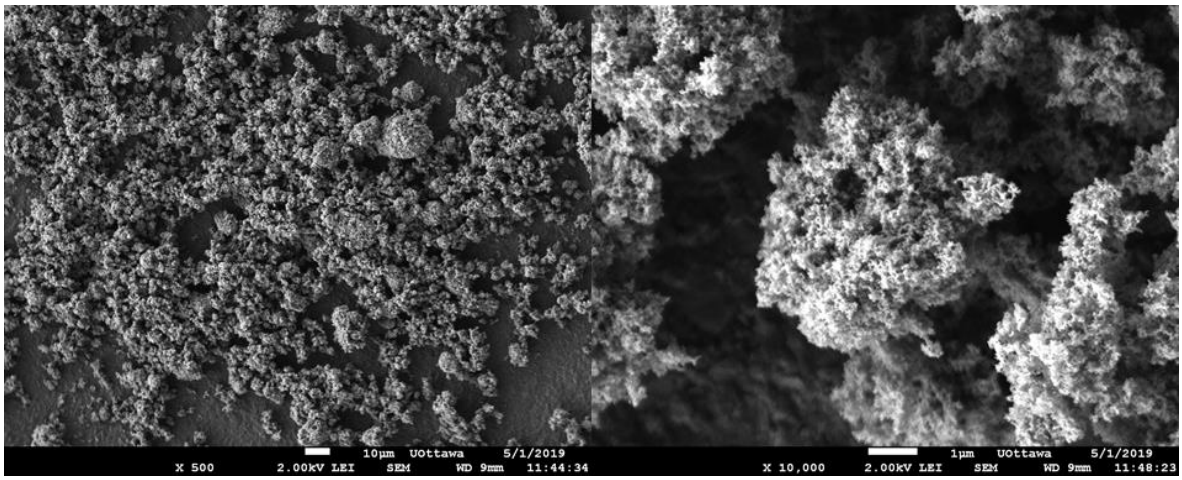

Figure 2.15. SEM images of pristine P25 with different scales.

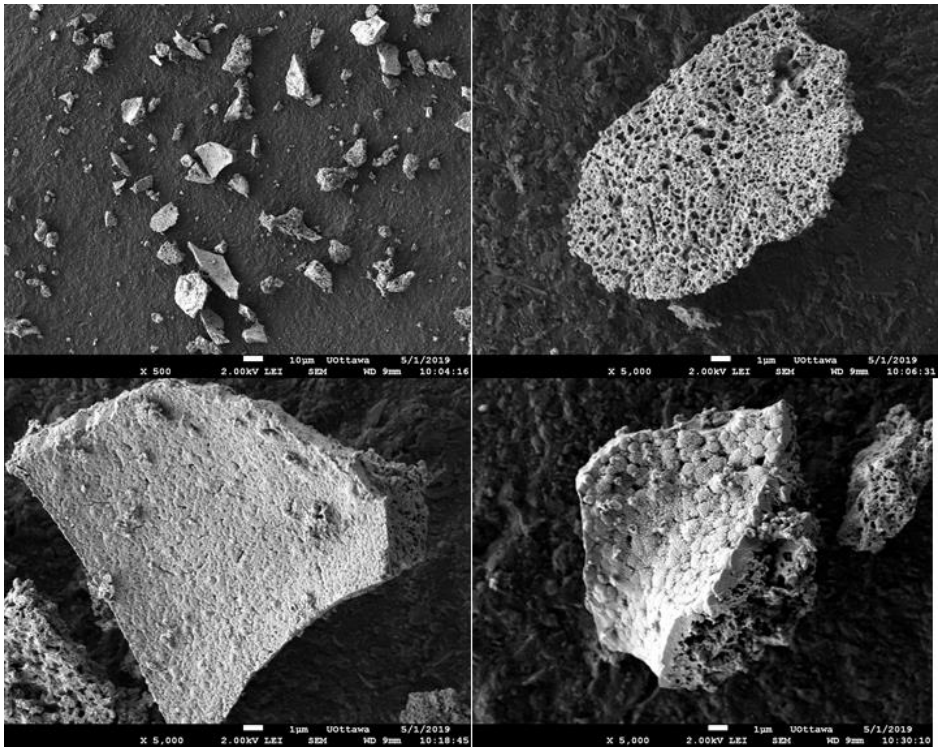

Figure 2.16. SEM images of mCuFeTi.

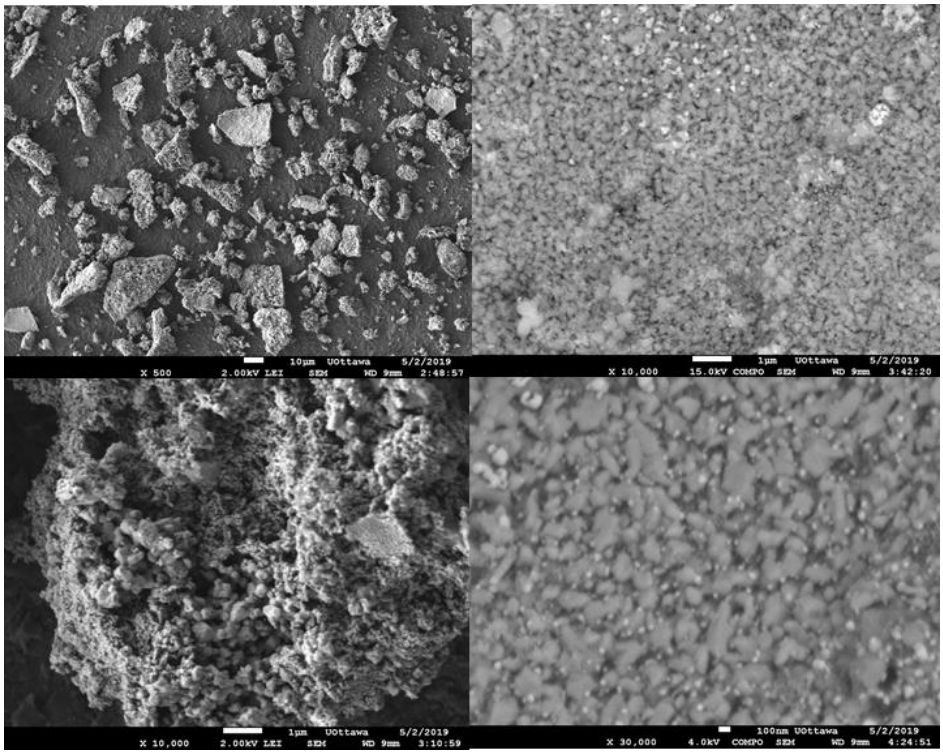

Figure 2.17. SEM images of b-mCuFeTi.

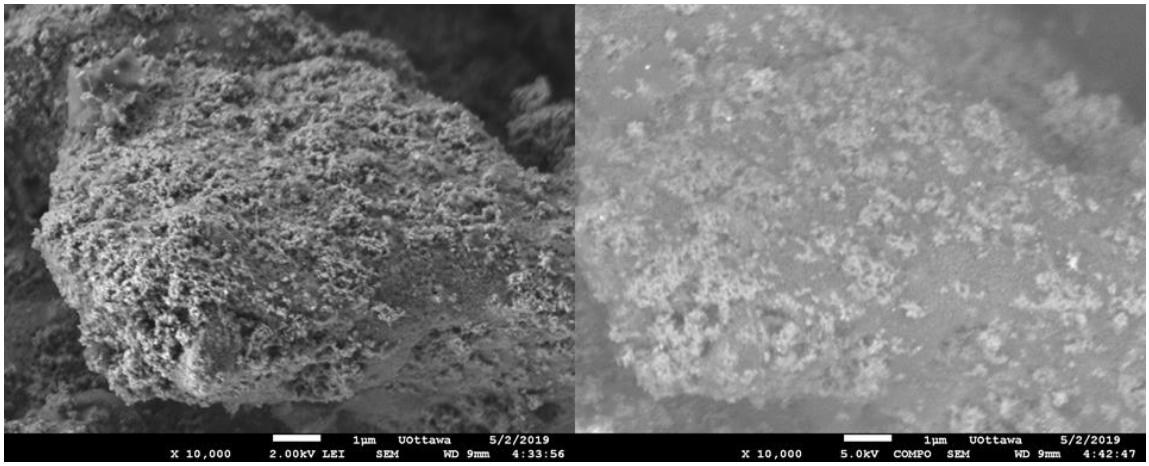

Figure 2.18. SEM images of *b-mCuFeTi.

Apart from P25, mCuFeTi, b-mCuFeTi, and *b-mCuFeTi were characterized by EDS elemental mapping. As shown in Figure 2.19, Cu, Fe, and Ti are uniformly distributed inside of the chunk. But on the surface of the chunk (Figure 2.20), site 3 shows no EDS Ti signal at all, which means that TiO_2 distribution is discrete. Furthermore, the higher content of carbon inside of the chunk can be explained as the solid surface of catalyst prevent the carbon inside from reacting with oxygen to generate carbon dioxide escaping from catalyst during calcination in muffle furnace under air. Comparing with mCuFeTi, TiO_2 inside of b-mCuFeTi chunks are more agglomerated (Figure 2.21). Especially at site 3 of area-1 of b-mCuFeTi, TiO_2 aggregates can be clearly observed, which explains why there is weak Fe signal and no Cu peak in the corresponding EDS spectrum. Meanwhile the surface of b-mCuFeTi is not as solid as the surface of mCuFeTi, which can be concluded from both SEM images and carbon signal intensity in EDS elemental mapping results (Figure 2.21 and 2.22). Figure 2.23 exhibits that the covered surface has low Cu, Fe and Ti signals but a high carbon peak in the EDS elemental mapping results, which is another evidence that the formation of carbon black during heating dry gel in the tubular furnace under argon.

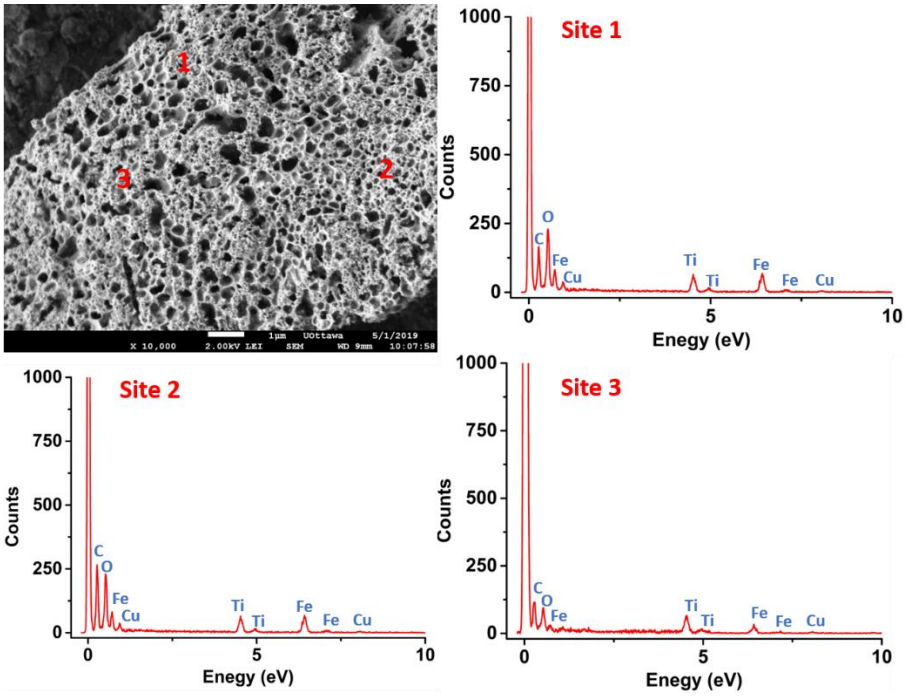

Figure 2.19. EDS elemental mapping on selected surface area-1 of mCuFeTi.

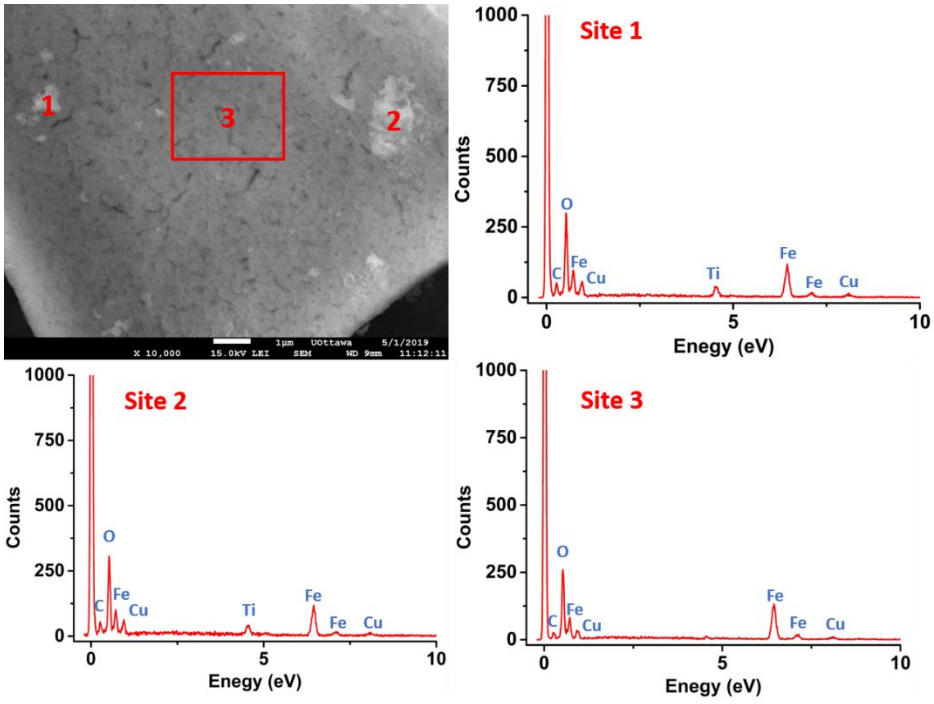

Figure 2.20. EDS elemental mapping on selected surface area-2 of mCuFeTi.

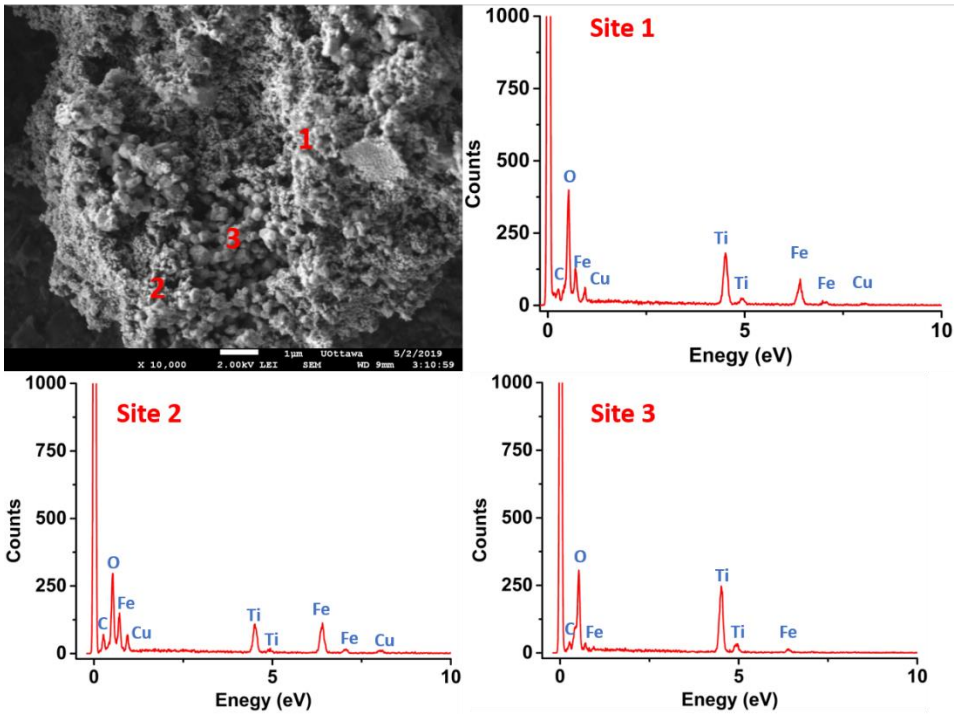

Figure 2.21. EDS elemental mapping on selected surface area-1 of b-mCuFeTi.

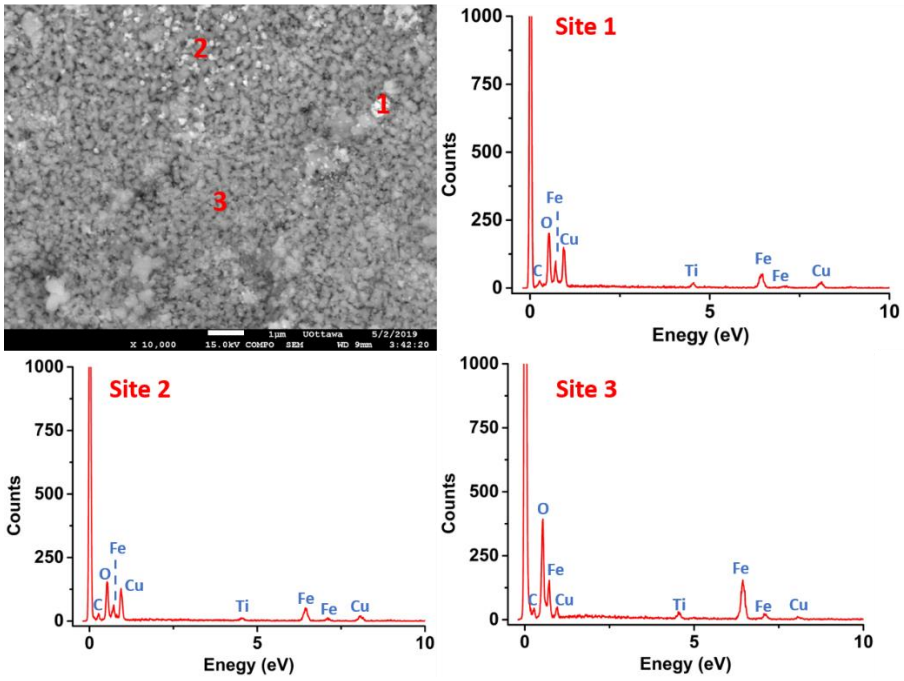

Figure 2.22. EDS elemental mapping on selected surface area-2 of b-mCuFeTi.

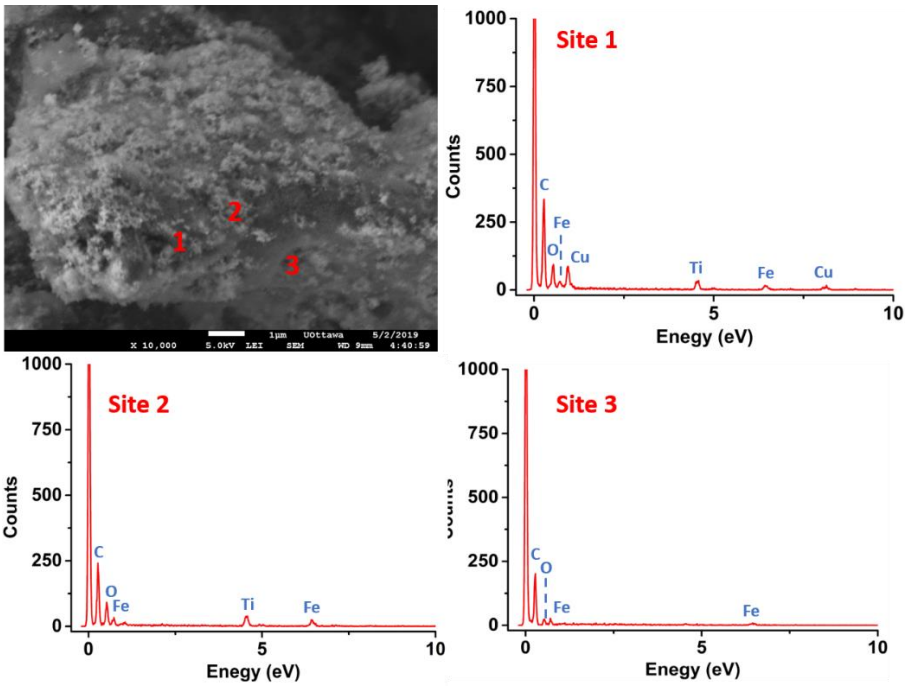

Figure 2.23. EDS elemental mapping on selected surface area of *b-mCuFeTi.

2.2.3.4 Magnetic Properties

The magnetic separation possibility can be illustrated in Figure 2.24. It shows the separation of supernatant (a) and catalyst (b) by simply decanting reaction mixture with the help of a strong magnet after half of a minute.

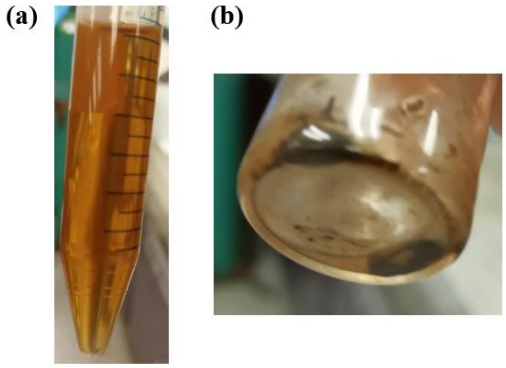

Figure 2.24. Magnetic separation of mFeTi catalyzed aromatic C-N coupling reaction.

2.2.4 Conclusion

In this part, magnetic and black magnetic catalyst were successfully synthesized using sol-gel methods and proved feasible in magnetic separation. Addition of Fe oxides and Cu/Fe oxides not only allows TiO_2 catalyst to be easily separated by a magnet after reaction, but also enhances the light absorption ability of TiO_2 catalyst in both UV and visible region. Raman results show that mFe is α- Fe_2O_3, P25 is anatase and blackening treatment will not change the crystalline of catalysts. The existence of Fe_3O_4 in black magnetic catalysts can be confirmed by Raman spectroscopy. But the crystalline of Cu oxide cannot be determined using Raman methods. SEM images display that all magnetic catalysts have porous chunky structures. mFeTi has a more solid shell than mCuFeTi resulting in higher carbon concentration inside of particles. A clear covered surface and high carbon signal on the surface of *b-CuFeTi reveal the formation of carbon black during blackening treatment of dry gel. To minimize the variables in the system and gain more reactive site on the surface of catalyst, *b-mCuFeTi will not be used in the reactions in next chapter.

Reference

1. Wang, W.; Ni, Y.; Lu, C.; Xu, Z. *Applied Surface Science* **2014,** 290, 125-130.
2. Khan, S. U. M.; Al-Shahry, M.; Ingler, W. B. *Science* **2002,** 297, (5590), 2243-2245.
3. Park, J. H.; Kim, S.; Bard, A. J. *Nano Letters* **2006,** 6, (1), 24-28.
4. Williams, G.; Seger, B.; Kamat, P. V. *ACS Nano* **2008,** 2, (7), 1487-1491.
5. Liu, Y.; Mu, K.; Yang, G.; Peng, H.; Shen, F.; Wang, L.; Deng, S.; Zhang, X.; Zhang, Y. *New Journal of Chemistry* **2015,** 39, (5), 3923-3928.
6. Zhao, Z.; Zhang, X.; Zhang, G.; Liu, Z.; Qu, D.; Miao, X.; Feng, P.; Sun, Z. *Nano Research* **2015,** 8, (12), 4061-4071.
7. Chen, S.; Xiao, Y.; Wang, Y.; Hu, Z.; Zhao, H.; Xie, W. *Nanomaterials* **2018,** 8.
8. Sangchay, W.; Sikong, L.; Kooptarnond, K. *Procedia Engineering* **2012,** 32, 590-596.
9. Ijadpanah-Saravy, H.; Safari, M.; Khodadadi-Darban, A.; Rezaei, A. *Analytical Letters* **2014,** 47, (10), 1772-1782.
10. Drits, V.; Środoń, J.; Eberl, D. D. *Clays and Clay Minerals* **1997,** 45, (3), 461-475.

11. Zhu, L.; Lu, Q.; Lv, L.; Wang, Y.; Hu, Y.; Deng, Z.; Lou, Z.; Hou, Y.; Teng, F. *RSC Advances* **2017,** 7, (33), 20084-20092.

12. Qiu, B.; Zhou, Y.; Ma, Y.; Yang, X.; Sheng, W.; Xing, M.; Zhang, J. *Scientific Reports* **2015,** 5, (1), 8591.

13. Liu, Y.; Mu, K.; Zhang, Y.; Wang, L.; Yang, G.; Shen, F.; Deng, S.; Zhang, X.; Zhang, S. *International Journal of Hydrogen Energy* **2016,** 41, (24), 10327-10334.

14. Li, K.; Gao, S.; Wang, Q.; Xu, H.; Wang, Z.; Huang, B.; Dai, Y.; Lu, J. *ACS Applied Materials & Interfaces* **2015,** 7, (17), 9023-9030.

15. Zhou, Y.; Chen, C.; Wang, N.; Li, Y.; Ding, H. *The Journal of Physical Chemistry C* **2016,** 120, (11), 6116-6124.

16. Zuo, F.; Wang, L.; Wu, T.; Zhang, Z.; Borchardt, D.; Feng, P. *Journal of the American Chemical Society* **2010,** 132, (34), 11856-11857.

17. Samira, B.; Nurhidayatullaili Muhd, J. *Reviews in Inorganic Chemistry* **2016,** 36, (3), 135-151.

18. Shakeel Akbar, S. K. H., Nasia Azmat, M. Nadeem. *Condensed Matter* **2004**.

19. Wypych, A.; Bobowska, I.; Tracz, M.; Opasinska, A.; Kadlubowski, S.; Krzywania-Kaliszewska, A.; Grobelny, J.; Wojciechowski, P. *Journal of Nanomaterials* **2014,** 2014, 124814.

20. Zhu, L.; Huang, W.; Rinehart, Z. S.; Tam, J.; Zhao, Y. *RSC Advances* **2016,** 6, (101), 98845-98853.

21. Hatel, R.; Majdoub, S. E.; Bakour, A.; Khenfouch, M.; Baitoul, M. *Journal of Physics: Conference Series* **2018,** 1081, 012006.

22. Abniel, M.; iacute; Mar; iacute; a, C.; Jos; eacute; Ducong; eacute; Juan, C. A.; Carmen, M.; Francisco, M.; aacute; rquez. *American Journal of Engineering and Applied Sciences* **2017,** 10, (2).

23. Kodom, T.; Rusen, E.; Călinescu, I.; Mocanu, A.; Şomoghi, R.; Dinescu, A.; Diacon, A.; Boscornea, C. *Journal of Nanomaterials* **2015,** 2015, 210734.

Chapter 3
TiO_2 Catalyst Application: Decarboxylation of 4-Methoxyphenylacectic Acid

3.1 Introduction

3.1.1 Decarboxylation

Decarboxylation is a fundamental and very important chemical reaction in chemistry, biology, and industry. For example, reactions such as decarboxylative cross coupling reactions[1-6] and decarboxylative polymerization reactions[7-9] require the intermediates generated from decarboxylation of precursors. In biology, decarboxylation of organic acids generates all carbon dioxide involved in respiration[10]. In industry, putting aside that the widely known tetrahydrocannabinol (THC) is the decarboxylation product of tetrahydrocannabinolic acid in the cannabis industry[11], decarboxylation is also applied in green energy field in order to reduce carbon emissions. Decarboxylases allow bio-based chemical production to operate at low temperature[12-14], rather than high energy-consuming temperature in the regular chemical industry.

To better use decarboxylation, we must know and study this powerful tool first. Decarboxylation is the reaction that removes carboxyl group from carboxylic acid to generate CO_2, and the corresponding alkanes or aryls (Equation 3.1). As shown in figure 3.1, the intermediates of decarboxylation can be electrophilic, nucleophilic, and radical depending on the reaction conditions and the catalyst employed[15]. The radical intermediate can be obtained from single electron transfer (SET), which will be intensively discussed in this chapter. As for the decarboxylation in living organism which is out of our scope, it will be left out of this dissertation.

$$R\text{-}COOH \rightarrow R\text{-}H + CO_2 \qquad (3.1)$$

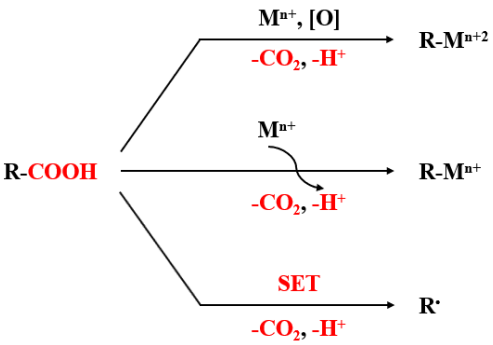

Figure 3.1. Possibilities of key decarboxylation intermediates.

3.1.2 Decarboxylation Mechanism

Although decarboxylation reactions are involved in many fields, the mechanism varies a lot by reaction conditions. In chemistry, the decarboxylation reaction, catalyzed by innovatively developed homogeneous and heterogeneous catalysts, attracts a lot of attention among researchers.

3.1.2.1 Homogeneous Catalysis

The key step in photocatalytic homogeneous catalysis in decarboxylation involves the chelating organic intermediates with a central metal ion to finish the electron transfer. Over several decades, heavy metal such as Ag[16-18], Pt[19-21], Fe[22], and Zn[23] are selected to be the central ion of the complex.

Figure 3.2 shows the decarboxylation mechanism summarized by Gwen and his colleagues using silver (I) salts and sodium peroxydisulfate[24]. First, a peroxydisulfate ion oxidize a silver (I) ion to silver (II) which can later chelate with a carboxylate ion to form a complex. Then the radical initiates the homolysis with the coordination bond, to form a silver (I) ion and an unstable carboxyl radical, which rapidly degrades into carbon dioxide and an alkyl radical. Finally, the alkyl radical finishes the reaction by abstracting hydrogen from solvent to form alkane. Due to the short lifetime of alkyl radicals, usually only alkane is observed in this reaction. The addition of copper (II) salts can stabilize the alkyl radical by forming a coordination complex, which can produce alkene by enabling the oxidative elimination.

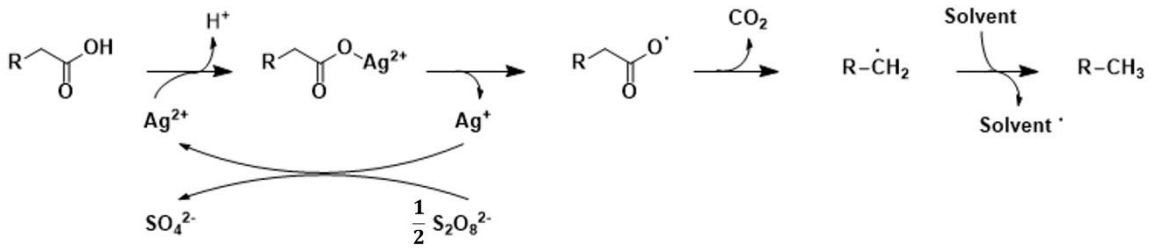

Figure 3.2. Mechanism of decarboxylation by silver (I) and peroxydisulfate.

The previous example is driven by the oxidation of silver (I) ions by peroxydisulfate, while light can also be the driving force. Yoshimi and his colleagues proposed the mechanism of aliphatic decarboxylation by photogenerated phenanthrene cation[25]. As shown in Figure 3.3, phenanthrene (Phen) is initially excited by UV light to form excited Phen, followed by electron transfer between Phen and 1,4-Dicyanobenzene (DCB) to generate Phen cation radicals and DCB anion radicals. Then a carboxylate ion dissociating from carboxylic acid transfer one electron to one Phen cation radical to form a carboxylic radical and a phenanthrene. This step can be done due to the negative Gibbs free energy (-0.34 V). The subsequential steps are the generation of carbon dioxide and alkane, which are the same as in the previous example. Although redox cycle is discussed in this paper, the role of oxidant (DCB) still remains unclear[26].

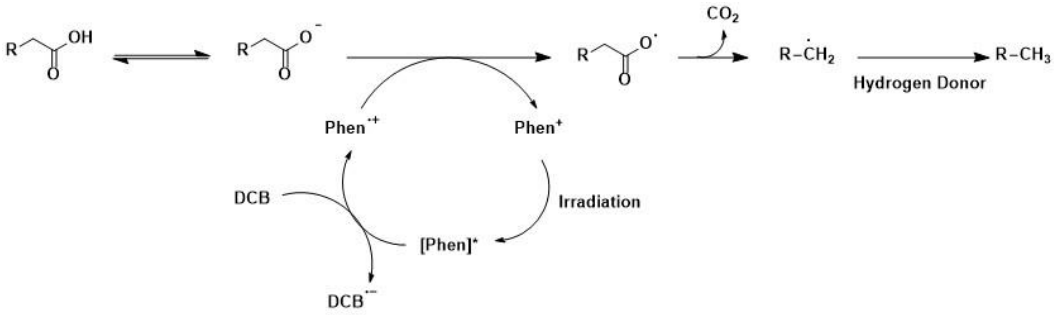

Figure 3.3. Mechanism of decarboxylation by photogenerated phenanthrene (Phen) cation and 1,4-Dicyanobenzene (DCB).

3.1.2.2 Heterogeneous Catalysis

As mentioned in the first chapter, the heterogeneous catalysts are under intensive research due to the high stability and easy separation after reaction. Heterogeneous catalysts, especially heterogeneous photocatalysts are also employed in decarboxylation reactions.

Titanium dioxide, as one of the most used photocatalytic semiconductor, is used in decarboxylation by David and his colleagues[27].They used TiO_2 as photocatalyst for $C(sp^3)$- $C(sp^3)$ decarboxylative homocoupling. From the mechanism shown in Figure 3.4, valence electrons are first excited to conduction band by UV light resulting in generating hot electrons and holes. Secondly, carboxylic acids are oxidized to alkyl radicals by the holes through single electron transfer. Carbon dioxide is also released in this step. The alkyl radicals then either undergo homocoupling pathway to form homocoupling (Kolbe coupling) products, or gain the hot electrons from TiO_2 and protons from reaction media to generate alkane.

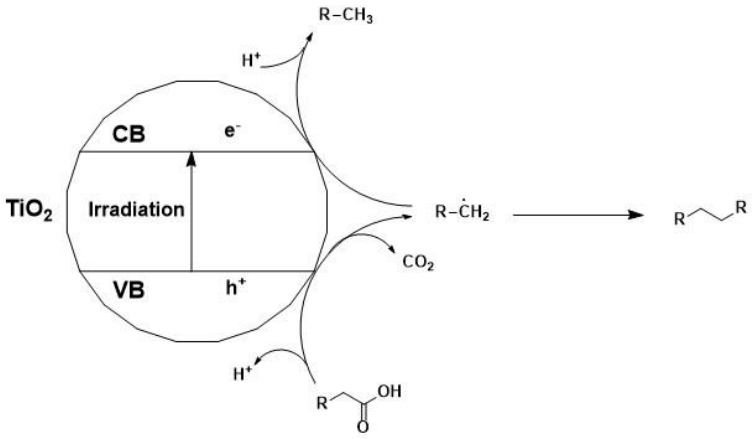

Figure 3.4. Mechanism of decarboxylative homocoupling by TiO_2 (VB - valence band, CB - conduction band).

Although TiO_2 is cheap and stable, its light absorption (only UV light) still limits TiO_2's catalytic activity. Graphitic carbon nitride (g-C_3N_4)[28, 29] and its derivatives[30] with their capability of visible-light absorption are used in decarboxylative reactions. So, here comes the question, can we achieve stability, low-cost and broad light absorption at the same time for one single catalyst? Black TiO_2 can be one candidate and will be discussed in detail in this chapter.

3.2 Decarboxylation Using White, Black, and Re-whited TiO_2

3.2.1 Introduction

In chapter 2, the both black anatase and rutile TiO_2 exhibit great UV-visible-light absorption. The re-whitening process is also able to change black TiO_2 back to white TiO_2.

In this part, anatase TiO_2 (a-Ti), rutile TiO_2 (r-Ti), black anatase TiO_2 (ba-Ti), black rutile TiO_2 (br-Ti), re-whited anatase TiO_2 (wa-Ti), and re-whited rutile TiO_2 (wr-Ti) are all tested their catalytic properties by decarboxylation of 4-methoxyphenylacetic acid.

3.2.2 Experimental

3.2.2.1 Chemicals

4-methoxyphenylacetic acid, dimethyl sulfone and tert-butylbenzene were purchased from Sigma-Aldrich and used without any further purification. Acetonitrile (MeCN), dioxane, tetrahydrofuran (THF) and toluene were all HPLC grade.

3.2.2.2 Instrumentation

LedEngin light-emitting diodes (LED)(10W) centered at 369 nm and 465 nm were used as the irradiation source for reactions. Luzchem LED illuminator (LEDi) equipped with seven powerful individual blue, red, green, and white LEDs with adjustable intensity at focal point were used for study. All ^1H NMR spectra were collected on a Bruker Avance 300 spectrometer (300 MHz) and a Bruker Avance II 400 (400 MHz) spectrometer with dimethyl sulfone as external standard. The concentration of alkyl product was measured on a GC-MS system with tert-butylbenzene as external standard. And the GC-MS spectra were collected on an Agilent 6890-N Gas Chromatograph with an Agilent 5973 mass selective detector calibrated with acetophenone.

3.2.2.3 General Procedure for Decarboxylation of 4-Methoxyphenylacetic Acid

4-Methoxyphenylacetic acid (50 mg, 0.3 mmol) and 20 mg of catalyst (a-Ti, r-Ti, ba-Ti, br-Ti, wa-Ti, or wr-Ti) were added into a 20-ml clean Pyrex tube with 5 ml of HPLC solvent (MeCN, dioxane, THF or toluene) and a magnetic stir bar. Then, the Pyrex tube was sealed by a rubber cap and sonicated for 1 min for better dispersion, followed by purging with ultrapure grade argon for 8 minutes. Purged reaction tube was then irradiated by a 369 nm LED with the power of 2600 W/m^2 (unless specified), while vigorously stirred by a magnetic stirrer for 17 hours. For quantification of alkane product, 40 μL of reaction mixture and 40 μL of tert-butylbenzene (10 mM in dichloromethane) were added in 1920 μL dichloromethane (DCM). Then, the mixture was filtered by a syringe filter (PTFE, 0.2 μm, Fisherbrand) and measured on the GC-MS system. The solid catalyst in the rest reaction mixture was separated by the same syringe filter and washed 3 times using 5 ml

of reagent grade acetone. After mixing all liquid, solvents were then removed by a rotary evaporator. Obtained solid was dissolved in d-chloroform with dimethyl sulfone (9.4 mg, 0.1 mmol) and finally ready for ^{1}H NMR measurement.

3.2.2.4 Irradiation Wavelength Influence Test

Two LEDs (369 nm and 465 nm) and one seven-headed LEDi were used to test the decarboxylation capability of a-Ti, ba-Ti, and br-Ti in MeCN. Two single LEDs were adjusted to 2600 W/m^2. The LEDi was set to white light only mode (W mode, 4156 W/m^2), red-green-blue light on mode (RGB mode, 2417 W/m^2) and red-green-blue-white on mode (RGBW mode, 4341 W/m^2) for the experiment. All other steps are the same as the general procedure.

3.2.2.5 Catalyst Amount Influence Test

Only changed the catalyst amount of 20 mg to 10 mg and solvent to dioxane in the general procedure to test the optimal usage of catalyst for the decarboxylation reaction in dioxane.

3.2.2.6 Kinetic Study

Reaction time of 1 h, 2 h, 3 h, 6 h, 17 h, and 20 h were chosen to analyze the kinetics of decarboxylation in dioxane. Every time spot was an individual experiment due to the sample amount required for ^{1}H NMR measurement.

3.2.2.7 Water Influence Test

The water influence test was done by adding extra 100 μL of Milli-Q water into reaction mixture or changing the solvent to Milli-Q water completely.

3.2.2.8 Reusability Test of Catalysts

In order to recycle the catalysts, centrifugation was utilized instead of syringe filter for the separation of reaction mixture. The catalysts were centrifuged at 10000 rpm for 10 min and washed 3 times with acetone. The recycled catalysts were then dried under air before second use. The reusability of all six catalysts was tested for 5 cycles.

3.2.3 Results and Discussion

3.2.3.1 Decarboxylation of 4-Methoxyphenylacetic Acid by TiO_2

The general chemical equation of decarboxylation of 4-methoxyphenylacetic acid by TiO_2 was shown in Figure 3.5. The reason why 4-methoxyphenylacetic acid was chosen as the substrate rather than phenylacetic acid is because the decarboxylation product of phenylacetic acid is toluene, which is impossible to be quantified when using toluene as the reaction solvent. As we can see in Figure 3.5, there are two different product: reduction (alkyl) product and homocoupling product. The reduction product: 4-methoxytoluene (or 4-methylanisole) can be perfectly quantified by the GC-MS that we possess with the help of external standard tert-butylbenzene. But the substrate left after reaction and the homocoupling product can only be identified, but not quantified by GC-MS, which makes it necessary to use ^{1}H NMR to monitor the concentration of substrate and homocoupling product. One important thing must be addressed here is that the concentrations of reduction product measured by GC-MS and ^{1}H NMR are not comparable. Because part of reduction product can be lost along with the solvent during rotary evaporation. Hence, all yield of reduction product is calculated from GC-MS results, while all conversion of substrate and yield of homocoupling product are calculated from ^{1}H NMR spectrum analysis in this chapter.

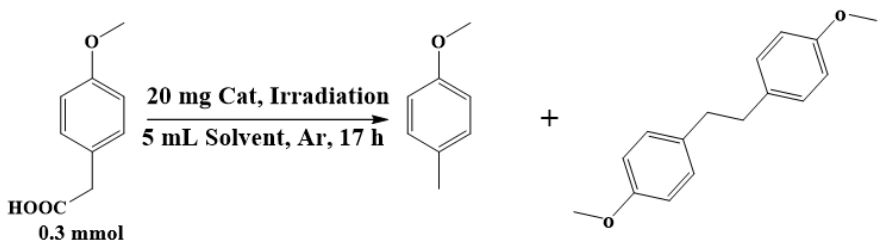

Figure 3.5. Decarboxylation of 4-methoxyphenylacetic acid by TiO_2.

3.2.3.2 Irradiation Wavelength Influence for 4-Methoxyphenylacetic Acid Decarboxylation by TiO_2

As mentioned in section 3.1.2.2, black TiO_2 catalysts have the potential to be able to use the energy from visible light to do the decarboxylation reaction. Here, one 369 nm LED, one 465 nm LED, and one seven-headed LEDi were chosen to test the idea we proposed. Unfortunately, as shown in Table 3.1, a-Ti, ba-Ti, and br-Ti only show their decarboxylation ability under UV irradiation in MeCN. No decarboxylative products were

found under blue LED irradiation, LEDi irradiations or without any irradiation. An explanation of these results could be that blackening process only modifies the very surface of TiO_2 nanoparticles, which makes the visible light be only absorbed by the modified layers, resulting in the very low intensity of hot electrons and holes for doing decarboxylation reaction. Meanwhile, the light-induced holes on the valence band of black TiO_2 catalysts may be short lived due to oxidizing Ti^{3+} into Ti^{4+}.

Table 3.1. Yield of reduction and homocoupling product under different irradiation and catalysts in MeCN.

Catalyst	Irradiation Source	Irradiance (W/m^2)	Reduction Yield %	Homocoupling Yield %
a-Ti	No light	0	0	0
a-Ti	369 nm LED	2600	17.2	18.2
a-Ti	465 nm LED	2600	0	0
ba-Ti	No light	0	0	0
ba-Ti	369 nm LED	2600	6.2	3.6
ba-Ti	465 nm LED	2600	0	0
br-Ti	369 nm LED	2600	7.5	2.3
br-Ti	465 nm LED	2600	0	0
ba-Ti	W (LEDi)	4156	0	0
ba-Ti	RGB (LEDi)	2417	0	0
ba-Ti	RGBW (LEDi)	4341	0	0

3.2.3.3 Solvent Influence Test for 4-Methoxyphenylacetic Acid Decarboxylation by TiO_2

MeCN, dioxane, THF, and toluene were chosen to be tested to find the best solvent for decarboxylation of 4-methoxyphenylacetic acid. From Figure 3.6 (a) and (c), Dioxane and THF exhibit excellent for reactant conversion and reduction product yield, while MeCN and toluene gave much worse overall results. This can be explained by the feasibility of proton abstraction from carboxylic acid by oxygen and nitrogen atoms. The two electron pairs and higher electronegativity of oxygen atoms on dioxane and THF stabilized the carboxylic ions, which accelerates the decarboxylation reaction. While nitrogen atom on the MeCN is a poor proton acceptor, followed by the least polar toluene that is unfavorable to the ionization of carboxylic acid. Homocoupling yield can be seen in

Figure 3.6 (b). Dioxane gave a relatively good homocoupling yield compared with other 3 solvents, but all homocoupling yields show that reduction product is the major product rather than the homocoupling one. The selectivity of reduction product over homocoupling product can be found in Figure 3.6 (d). Dioxane, again, exhibits good selectivity towards reduction product. Although MeCN also gives higher reduction/homocoupling ratio, the dioxane is finally chosen as the solvent for all following experiments due to its great overall performance.

From Figure 3.6, not only the solvent influence can be discussed, but catalysts also gave very different results under different conditions. Among all six catalysts, white anatase TiO_2 (a-Ti) shows the best catalytic ability for decarboxylation of 4-methoxyphenylacetic acid. After blackening treatment, the reaction conversion and yield dramatically dropped. But it is interesting that its catalytic ability in dioxane and toluene can be mostly recovered by re-whitening process. This is another evidence that the blackening treatment for our catalysts is reversible. For rutile TiO_2 catalysts, blackening and re-whitening treatment did not influence too much on decarboxylation ability.

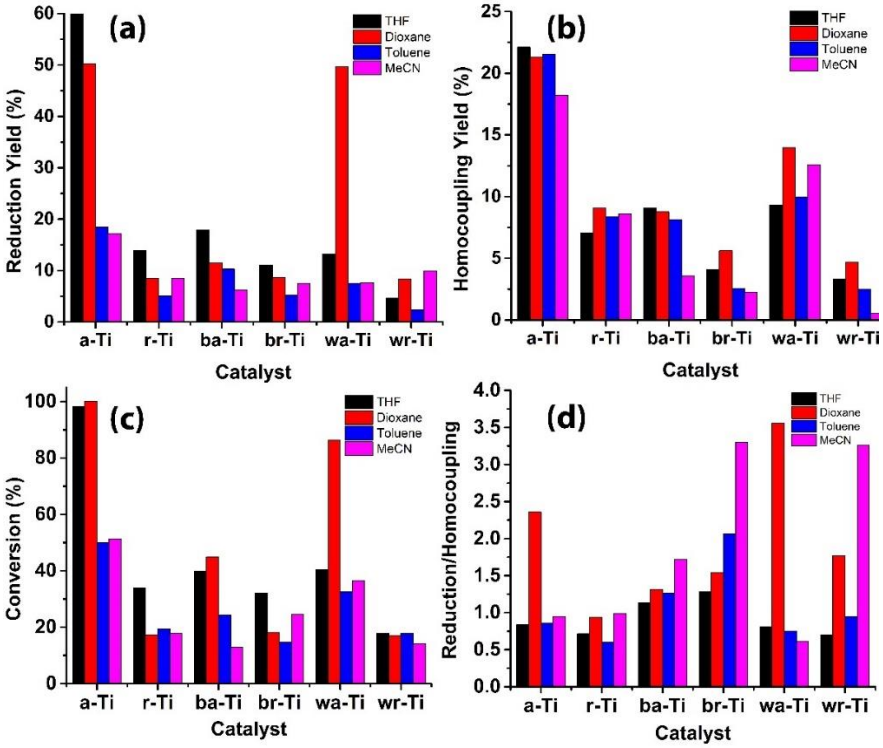

Figure 3.6. The reduction yield (a), homocoupling yield (b), substrate conversion (c) and product selectivity (d) of a-Ti, ba-Ti, wa-Ti, r-Ti, br-Ti, and wr-Ti in MeCN, dioxane, THF, and toluene after 17-hour 369-nm irradiation.

3.2.3.4 Optimization of Catalyst Amount

The catalyst amount is very important in many chemical reactions. The lack of catalyst will certainly lead to low yield, while putting excess catalyst into a reaction mixture can also have negative impact on the reaction outcome. For photocatalytic reactions, too much catalyst can cause severe light scattering resulting in low quantum yield. Hence it is not true that more catalyst we put, the better yield we get. Here, because putting 20 mg of a-Ti in 5 ml of reaction solution already makes the mixture milky, we only compare the results from the reaction with 10 mg and 20 mg of catalysts.

In Figure 3.7, it is clearly shown that when the catalyst amount was cut in half, the reduction yield, homocoupling yield and substrate conversion using a-Ti dropped around four fifths. Huge reaction yield falling off can also be observed in ba-Ti, wa-Ti, r-Ti, br-Ti, and wr-Ti. Only the homocoupling yield for ba-Ti remained the same, indicating that 10 mg of ba-Ti is enough for getting the homocoupling yield of 8.6%. Thus 20 mg of catalyst were always used in all experiments.

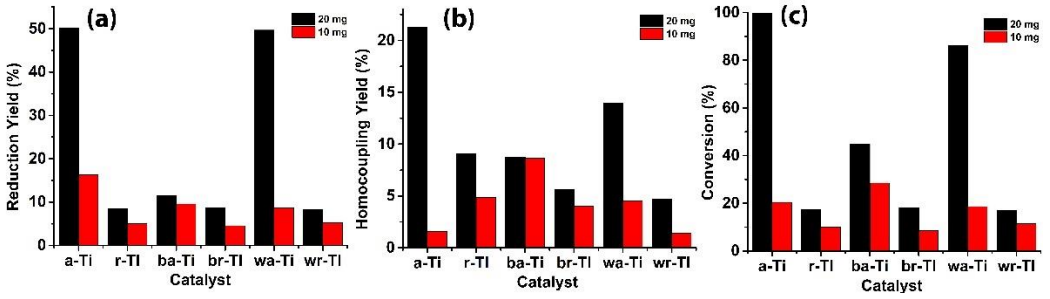

Figure 3.7. The reduction yield (a), homocoupling yield (b) and substrate conversion (c) using 10 mg or 20 mg of a-Ti, ba-Ti, wa-Ti, r-Ti, br-Ti, and wr-Ti after 17-hour 369-nm irradiation in dioxane.

3.2.3.5 Kinetic Study

In order to know how fast the decarboxylation reaction of 4-methoxyphenylacetic acid catalyzed by six different photocatalysts acid can be done, and understand the mechanism of this reaction, the reduction yield, homocoupling product yield, and substrate conversion were calculated after the reaction time of 1, 2, 3, 6, 17, and 20 hours. Figure 3.8 shows that substrate decarboxylated fast during first 6 hours, then slowed down and gradually reached the maximum conversion after 17 to 20 hours. Meanwhile reduction and homocoupling yields also followed the similar trend as substrate conversion. It is important

to note that the rate of homocoupling reaction is faster than reduction reaction in first 2 or 3 hours. This is because the concentration of benzyl radicals generated by light-induced holes is decreasing as the reaction progresses. Lower concentration of benzyl radicals on the catalyst's surface makes it hard for one radical to find another to form homocoupling products. White TiO_2 catalysts show better reactivities than their black counterparts, which may be due to the elimination of light-induced holes by oxidizing Ti^{3+} to Ti^{4+} species during the irradiation. The first-order reaction fitting was applied in fitting the kinetic data. As shown in Figure 3.9, there are good linear relationships between Ln(Yield) vs. time in all cases, which indicates the decarboxylation of 4-methoxyphenylacetic acid undergoes a Pseudo-first-order reaction pathway.

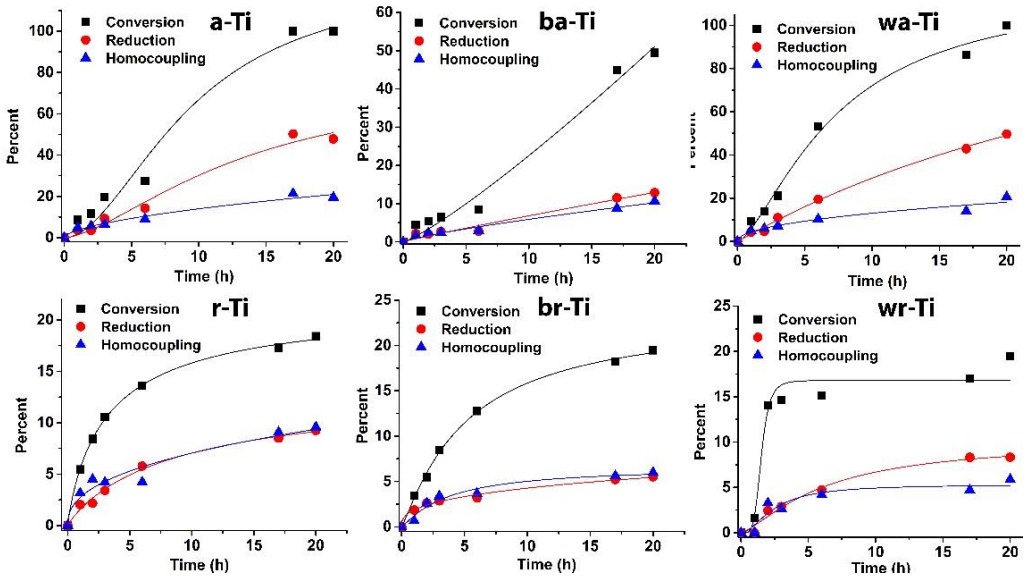

Figure 3.8. Kinetics of 4-methoxyphenylacetic acid decarboxylation kinetics using a-Ti, ba-Ti, wa-Ti, r-Ti, br-Ti, and wr-Ti.

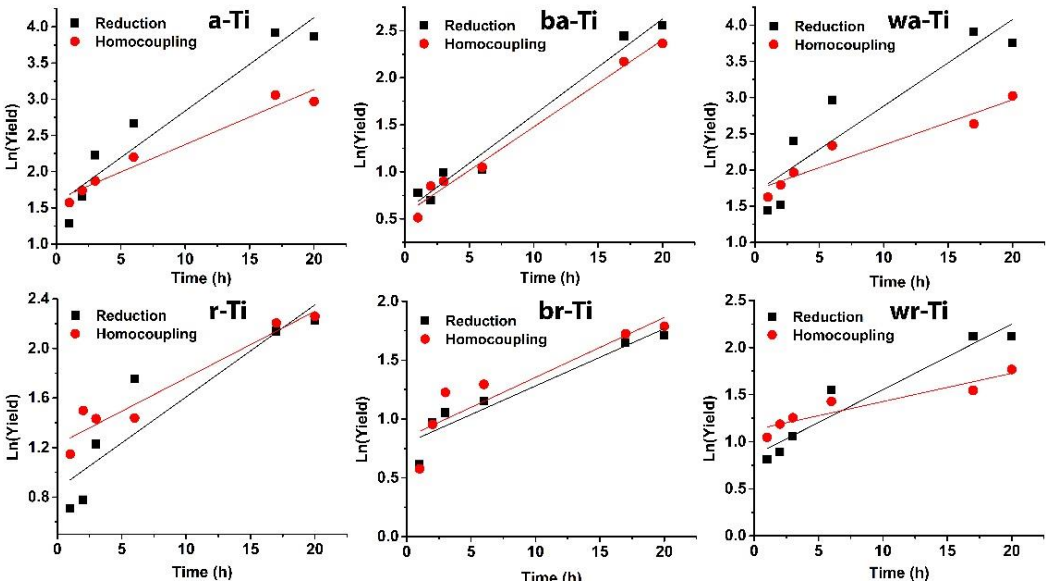

Figure 3.9. First-order reaction fitting of 4-methoxyphenylacetic acid decarboxylation kinetics using a-Ti, ba-Ti, wa-Ti, r-Ti, br-Ti, and wr-Ti.

3.2.3.6 Water Influence Test for 4-Methoxyphenylacetic Acid Decarboxylation by TiO_2

Hongna and her colleagues published a paper suggesting that water can change the gaseous carboxylic acid adsorption mode on anatase TiO_2 surface, which enhanced the decarboxylation yields[31]. So, in our case, it would be great if adding water can increase the decarboxylation yields or replacing organic solvent with water completely in the environmentally friendly viewpoint. Unfortunately, there is no reduction or homocoupling product was observed in the experiments of replacing solvent with water. But adding 100 μL of Milli-Q water into reaction mixture did enhance the reaction yield and conversion for rutile catalysts a lot, except the homocoupling reaction with r-Ti (Figure 3.10). Comparing with the Hongna's paper, adding water into our anatase-catalyst reactions can only hinder the decarboxylation of 4-methoxyphenylacetic acid.

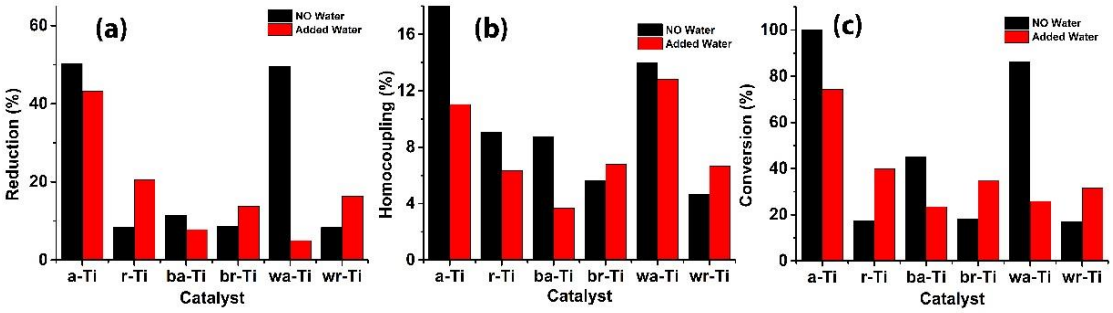

Figure 3.10. The reduction yield (a), homocoupling yield (b) and substrate conversion (c) using a-Ti, ba-Ti, wa-Ti, r-Ti, br-Ti, and wr-Ti with or without adding 100 μL of Milli-Q water in 5-mL reaction mixture after 17-hour 369-nm irradiation in dioxane.

3.2.3.7 Reusability of All 6 Catalysts in 4-Methoxyphenylacetic Acid Decarboxylation Reaction

To assess the stability of all 6 catalysts, reduction yield, homocoupling yield and substrate conversion were calculated and plotted after 5 catalytic cycles for decarboxylation of 4-methoxyphenylacetic acid. As shown in Figure 3.11, both a-Ti and wa-Ti lost 60% of catalytic activity after 3 cycles, while ba-Ti exhibited good catalytic stability over 5 cycles. This can be explained that the catalyst lost between different cycles and the sensitivity of catalyst amount of the reactions with a-Ti and wa-Ti (Figure 3.7). Also, one important phenomenon observed was that reaction mixtures of a-Ti and wa-Ti turned to blue after reaction. This can be explained that an anaerobic environment in the Pyrex tube and UV irradiation makes it possible to generate traces of 'black' TiO_2 along with the ongoing reaction. After 2 or 3 catalytic cycles, part of a-Ti and wa-Ti turned to black TiO_2, which significantly decreases the catalytic activity of the original catalysts. Due to the higher thermal stability, the color of rutile catalysts remained after reaction, which makes them maintain the catalytic activity after 5 catalytic cycles (Figure 3.12).

Looking at reduction and homocoupling yields during 5 catalytic cycles, only the yield of reduction product dropped a lot after first cycle, and then remained at the similar levels after other 4 cycles. This could indicate that reduction reaction favors the fresh catalyst surface.

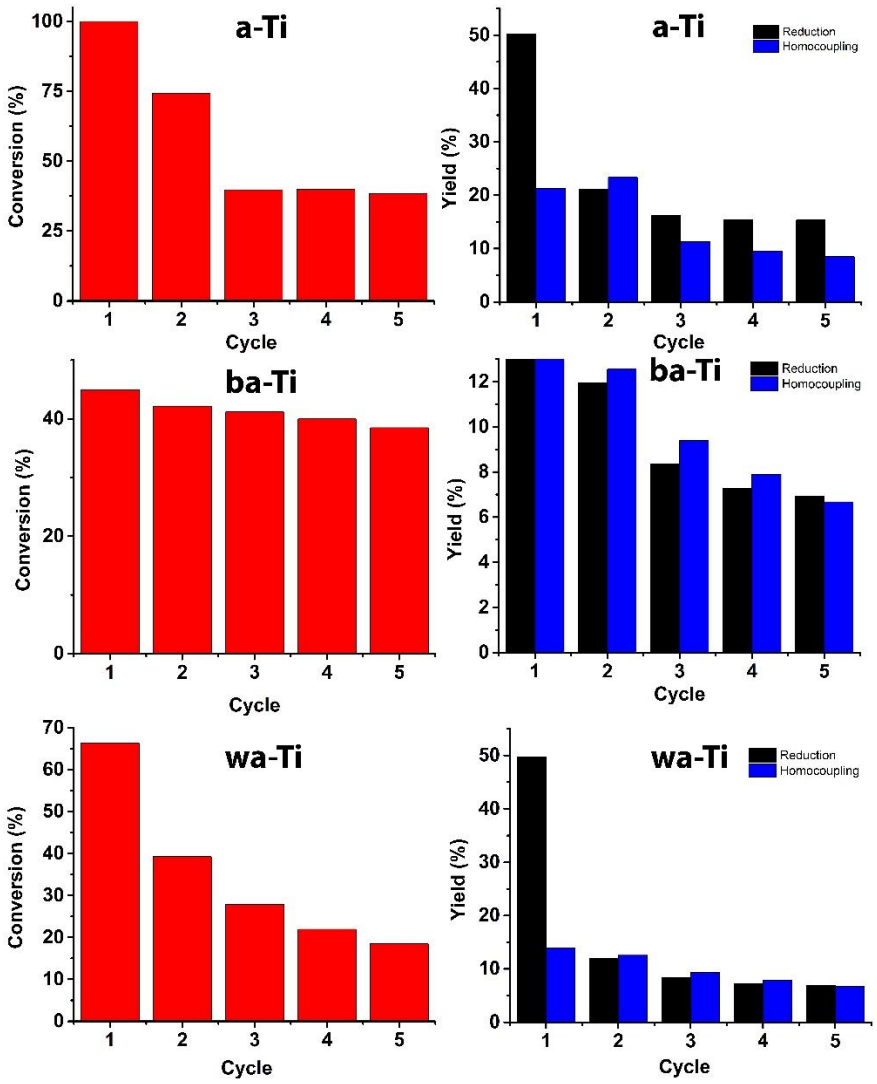

Figure 3.11. The reduction yield, homocoupling yield and substrate conversion using a-Ti, ba-Ti, and wa-Ti after 5 catalytic cycles for decarboxylation of 4-methoxyphenylacetic acid.

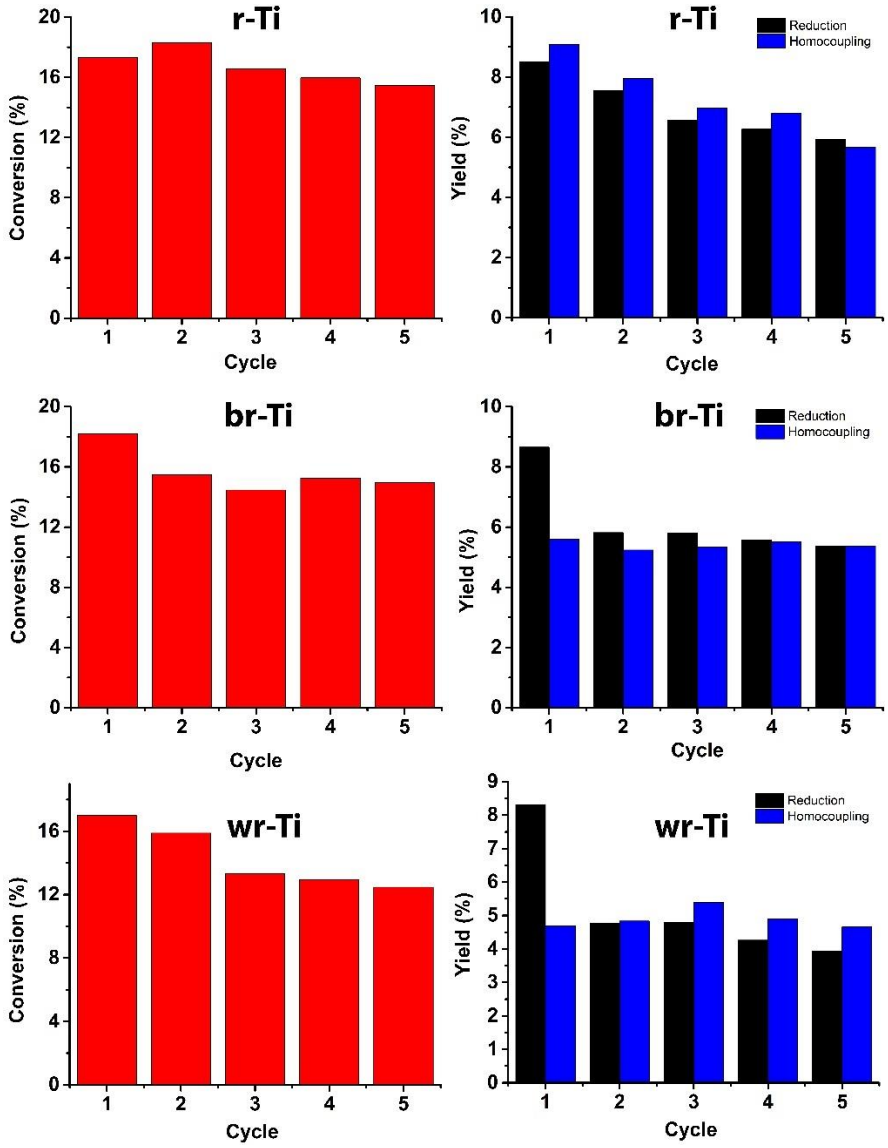

Figure 3.12. The reduction yield, homocoupling yield and substrate conversion using r-Ti, br-Ti, and wr-Ti after 5 catalytic cycles for decarboxylation of 4-methoxyphenylacetic acid.

3.2.4 Conclusion

In this part, dioxane was found as the best solvent for the decarboxylation reaction of 4-methoxyphenylacetic acid. The optimal catalyst amount and reaction time were determined as 10 mg and 17 h, respectively. Anatase catalysts were also found having higher catalytic activity than rutile TiO_2 for 4-methoxyphenylacetic acid decarboxylation. Adding water can significantly increase the reaction conversion and yield for rutile catalysts, but have negative impact on anatase counterparts. Reusability of ba-Ti, r-Ti, br-

Ti, and wr-Ti was good after 5 catalytic cycles, while a-Ti and wa-Ti were deactivated a lot due to generating black TiO_2 in first 2 cycles. The original idea of using visible light in the decarboxylation reaction failed. But the similar catalytic activity of a-Ti and wa-Ti, as well as ba-Ti's poor catalytic activity both proved that the blackening treatment is reversible, and the catalytic activity of anatase TiO_2 can be restored by the re-whitening process.

Reference

1. Lang, S. B.; O'Nele, K. M.; Tunge, J. A. *Journal of the American Chemical Society* **2014,** 136, (39), 13606-13609.

2. Lackner, G. L.; Quasdorf, K. W.; Pratsch, G.; Overman, L. E. *The Journal of Organic Chemistry* **2015,** 80, (12), 6012-6024.

3. Qin, T.; Cornella, J.; Li, C.; Malins, L. R.; Edwards, J. T.; Kawamura, S.; Maxwell, B. D.; Eastgate, M. D.; Baran, P. S. *Science* **2016,** 352, (6287), 801-805.

4. Kolarovič, A.; Fáberová, Z. *The Journal of Organic Chemistry* **2009,** 74, (18), 7199-7202.

5. Gigant, N.; Chausset-Boissarie, L.; Gillaizeau, I. *Organic Letters* **2013,** 15, (4), 816-819.

6. Wang, Y.; Li, X.; Leng, F.; Zhu, H.; Li, J.; Zou, D.; Wu, Y.; Wu, Y. *Advanced Synthesis & Catalysis* **2014,** 356, (16), 3307-3313.

7. Liao, W.; Ni, X. *Photochemical & Photobiological Sciences* **2017,** 16, (8), 1211-1219.

8. Du, N.; Dal-Cin, M. M.; Robertson, G. P.; Guiver, M. D. *Macromolecules* **2012,** 45, (12), 5134-5139.

9. Chapman, R.; Melodia, D.; Qu, J.-B.; Stenzel, M. H. *Polymer Chemistry* **2017,** 8, (43), 6636-6643.

10. Li, T.; Huo, L.; Pulley, C.; Liu, A. *Bioorganic Chemistry* **2012,** 43, 2-14.

11. Perrotin-Brunel, H.; Buijs, W.; Spronsen, J. v.; Roosmalen, M. J. E. v.; Peters, C. J.; Verpoorte, R.; Witkamp, G.-J. *Journal of Molecular Structure* **2011,** 987, (1), 67-73.

12. Könst, P. M.; Franssen, M. C. R.; Scott, E. L.; Sanders, J. P. M. *Green Chemistry* **2011,** 13, (5), 1167-1174.

13. Könst, P. M.; Franssen, M. C. R.; Scott, E. L.; Sanders, J. P. M. *Green Chemistry* **2009,** 11, (10), 1646-1652.

14. Lammens, T. M.; De Biase, D.; Franssen, M. C. R.; Scott, E. L.; Sanders, J. P. M. *Green Chemistry* **2009,** 11, (10), 1562-1567.

15. Patra, T.; Maiti, D. *Chemistry – A European Journal* **2017,** 23, (31).

16. van der Klis, F.; van den Hoorn, M. H.; Blaauw, R.; van Haveren, J.; van Es, D. S. *European Journal of Lipid Science and Technology* **2011,** 113, (5), 562-571.

17. Anderson, J. M.; Kochi, J. K. *Journal of the American Chemical Society* **1970,** 92, (6), 1651-1659.

18. House, D. A. *Chemical Reviews* **1962,** 62, (3), 185-203.

19. Goossen, L. J.; Linder, C.; Rodríguez, N.; Lange, P. P. *Chemistry – A European Journal* **2009,** 15, (37), 9336-9349.

20. Goossen, L. J.; Rodríguez, N.; Melzer, B.; Linder, C.; Deng, G.; Levy, L. M. *Journal of the American Chemical Society* **2007,** 129, (15), 4824-4833.

21. Gooßen, L. J.; Rodríguez, N. *Chemical Communications* **2004**, (6), 724-725.

22. Maetani, S.; Fukuyama, T.; Suzuki, N.; Ishihara, D.; Ryu, I. *Chemical Communications* **2012,** 48, (19), 2552-2554.

23. Pan, T.; Deng, J.; Xu, Q.; Zuo, Y.; Guo, Q.-X.; Fu, Y. *ChemSusChem* **2013,** 6, (1), 47-50.

24. Dawes, G. J. S.; Scott, E. L.; Le Nôtre, J.; Sanders, J. P. M.; Bitter, J. H. *Green Chemistry* **2015,** 17, (6), 3231-3250.

25. Yoshimi, Y.; Itou, T.; Hatanaka, M. *Chemical Communications* **2007**, (48), 5244-5246.

26. Bhattacherjee, A.; Sneha, M.; Lewis-Borrell, L.; Tau, O.; Clark, I. P.; Orr-Ewing, A. J. *Nature Communications* **2019,** 10, (1), 5152.

27. Manley, D. W.; Walton, J. C. *Organic Letters* **2014,** 16, (20), 5394-5397.

28. Cai, Y.; Tang, Y.; Fan, L.; Lefebvre, Q.; Hou, H.; Rueping, M. *ACS Catalysis* **2018,** 8, (10), 9471-9476.

29. Guo, J.; Wang, Y.; Li, Y.; Lu, K.; Liu, S.; Wang, W.; Zhang, Y. *Advanced Synthesis & Catalysis* **2020,** 362, (18), 3898-3904.

30. Wang, L.; Wang, Y.; Chen, Q.; He, M. *Tetrahedron Letters* **2018,** 59, (15), 1489-1492.

31. Zhang, H.; Zhou, P.; Ji, H.; Ma, W.; Chen, C.; Zhao, J. *Applied Catalysis B: Environmental* **2018,** 224, 376-382.

Chapter 4
Magnetic Catalyst Application: Aldehyde-alkyne-amine (A^3) Coupling Reaction

4.1 Introduction

4.1.1 Propargylamine

It has been approved that ladostigil, 1-deprenile, and rasagiline (Figure 4.1 a, b, and c, respectively) are anti-Parkinson active compounds[1-4]. They are all in a versatile group of compounds called propargylamines (Figure 4.1 d), which is deeply involved in pharmaceutical and pharmacological chemistry. It has been discovered that molecules containing propargylamine skeleton are not only anti-Parkinson active, but useful for antidiabetic, antitumor, vasodilator, and bronchodilator field[5-8]. Meanwhile, propargylamines are also important precursors in synthesizing other organic compounds, drugs, and natural products[9-16].

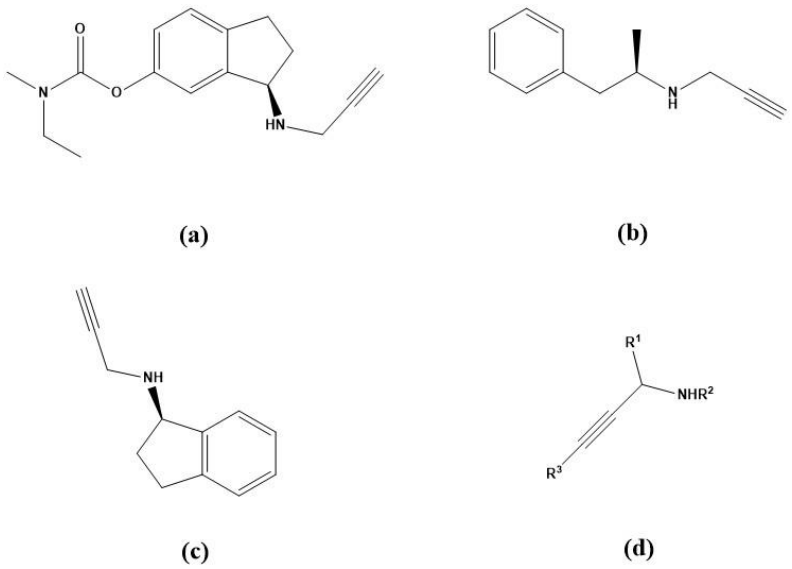

Figure 4.1. The structure of ladostigil (a), 1-deprenile (b), and rasagiline (c). (d) shows the general structure of propargylamine.

As shown in Figure 4.1, propargylamine (d) contains a β-amine group linked to a carbon-carbon triple bond. The lone-pair electrons on the amine moiety make propargylamines able to act as nucleophiles, while the alkyne group enables the propargylamine to undergo the characteristic alkyne reaction pathways. Together, these two groups broaden the application of propargylamine in organic synthesis.

The synthesis of propargylamines mainly includes aldehyde-alkyne-amine coupling (A^3 coupling)[16-23], alkynylation of imines[24], amination of propargylic halides[25], propargylic phosphates[26], or propargylic triflates[27, 28], and anti-Markovnikov hydroamination[29]. Among all synthetic routes, A^3 coupling stands out due to its overall convenience.

4.1.2 A^3 Coupling Reaction

The aldehyde-alkyne-amine coupling (A^3 coupling) reaction, as a multicomponent reaction, enables the synthesis of relatively complicated propargylamine compounds through a simple one-pot reaction from a variety of aldehydes, amines, and alkynes[30]. It is important to note that the alkynes must be terminal alkynes in regular A^3 coupling reactions because the reaction involves C-H activation[30, 31].

Most reported A^3 coupling reactions use metal and metal oxides (such as Cu[32-36], Ru[32], Ni[37, 38] and Fe[35, 36, 39]) to activate the C-H bond of terminal alkynes. Concerning the concept of green chemistry, metal-free A^3 coupling reactions are developed through decarboxylative pathways[40] or microwave-assisted treatment[41]. To simplify the post-reaction processing, heterogeneous catalysts are also introduced into A^3 coupling reactions. Examples will be discussed in the following sections.

4.1.3 Regular A^3 Coupling Reaction

The first Ru (III)/Cu (I) catalyzed imine alkylation A^3 coupling reactions were introduced by Li and colleagues in 2002[42]. As shown in Figure 4.2, the nucleophilic Ru (III) salts first react with alkyne molecules forming Ru (IV)-acetylides to activate the C-H

bonds. Then the CuBr-activated imines react with Ru (IV)-acetylides and subsequently generate the final product.

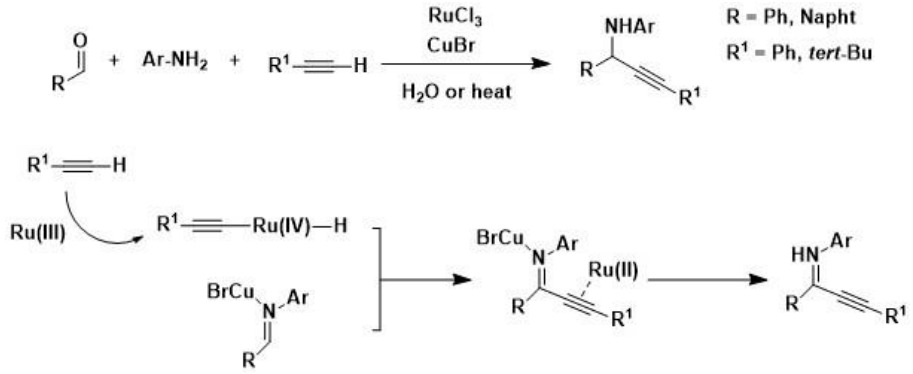

Figure 4.2. Schematic of Ru/Cu catalyzed A^3 coupling reaction.

Knochel's group intensively investigated and optimized the alkylation of enamines using CuBr[43]. In their reactions, CuBr activates the C-H bond rather than N-H bond to form the Copper acetylides, and the (+)-QUINAP was added as stereoselective ligand. The results are shown in Table 4.1. A variety of propargylamines were successfully synthesized using different enamines and alkynes with high yield and enantiomeric excess.

Table 4.1. Results of stereoselective A^3 coupling reaction by Knochel's group.

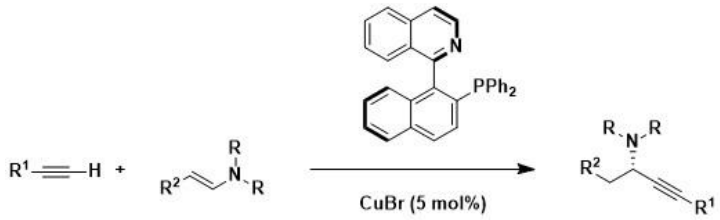

Entry	R^1	R^2	R^3	yield %	enantiomeric excess %
1	Ph	Pr	Bn	78	83
2	CH_2OMe	Pr	Bn	76	55
3	1-c-hexenyl	Pr	Bn	84	74
4	CH_2CH_3CN	Pr	Bn	50	54
5	CH_2CH_3Cl	Pr	Bn	58	60
6	$CH_2OTBDPS$	Pr	Bn	85	72
7	TMS	Pr	Bn	73	86
8	Ph	Pr	Allyl	99	77
9	3-pyridyl	Pr	Bn	57	70

4.1.3.1 Metal-free Catalyzed A^3 Coupling Reaction

A^3 coupling reactions can also be done under metal-free conditions. Using decarboxylative A^3 coupling reactions as an example (Figure 4.3)[8], with the help of propiolic acid or its derivatives, iminium intermediates and carboxylates can be produced. Then the reaction undergoes a nucleophilic addition pathway and subsequently releases carbon dioxide to form the final propargylamine products.

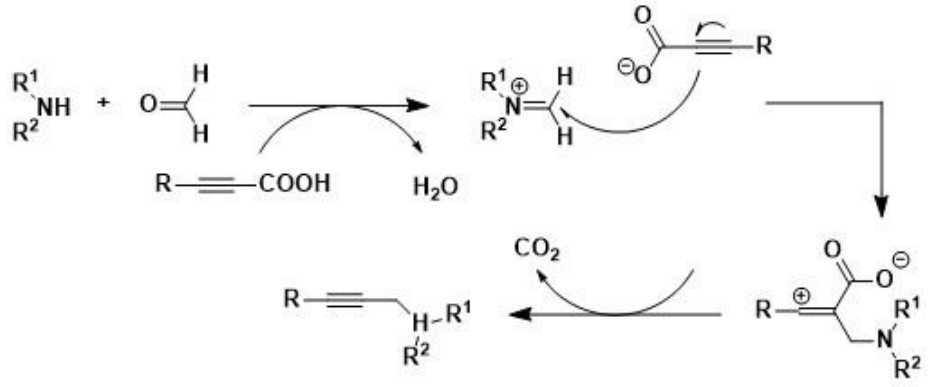

Figure 4.3. Reaction mechanism of metal-free decarboxylative A^3 coupling reaction.

4.1.3.2 Magnetic Catalyst A^3 Coupling Reaction

Although the stereoselectivity and metal-free condition can be achieved in homogeneous catalytic reactions, the post-reaction processing can be complicated and hinder its applications in large-scale synthesis. Thus, the magnetic heterogeneous catalysts provide a route lowering the product separation cost[8].

Sreedhar and colleagues developed a new route of A^3 coupling reaction using Ni-functionalized ferrite (Fe_3O_4) nanoparticles[39]. As shown in Figure 4.4, magnetic nanoparticles interact with alkynes and amines to form the metal-acetylides and ammonium ions. Then, the intermediates generated from ammonium ions and aldehydes react with metal-acetylides to produce the final propargylamine product. The paper does not mention which part of the nanoparticle (Fe_3O_4 or NiO) activates the C-H bond, but from Gajengi's paper[37], it is believed that NiO is the functional part that is activating C-H bond. Meanwhile, Fe_3O_4 surely acts as the magnetic separation support, but its role in the coupling reaction remains unclear.

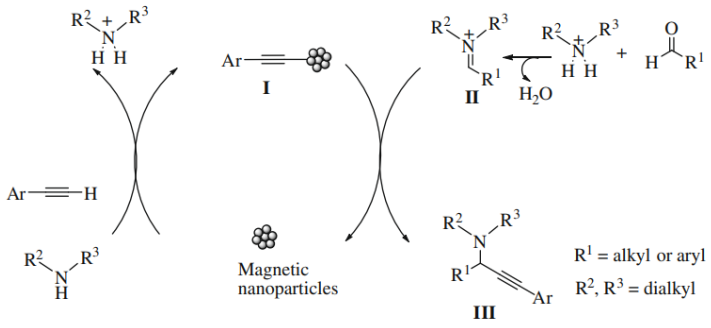

Figure 4.4. Reaction mechanism of NiO/Fe_3O_4 catalyzed A^3 coupling reaction. Reprinted with permission from ref. 39.

To prevent the catalyst from aggregation, Marzieh and coworkers synthesized NiO-functionalized oleic acid-coated $CuFe_2O_4$ ($NiO/OA\text{-}CuFe_2O_4$) nanoparticles[38]. The non-toxic oleic acid coating not only protects and stabilize the magnetic core, but also acts as bridge between NiO and $CuFe_2O_4$. The A^3 coupling reaction yield of this catalyst was found 95% after 5 hours in toluene. The catalytic activity also well sustains at least for 5 reaction cycles. The reaction mechanism they proposed is illustrated in Figure 4.5. Unlike Sreedhar's mechanism mentioned above, Marzieh and coworkers catalyst not only activates the alkyne C-H bonds, but also promotes the formation of iminium ion. The discussions of the formation of water molecules and surface hydroxyl groups are missing in the paper.

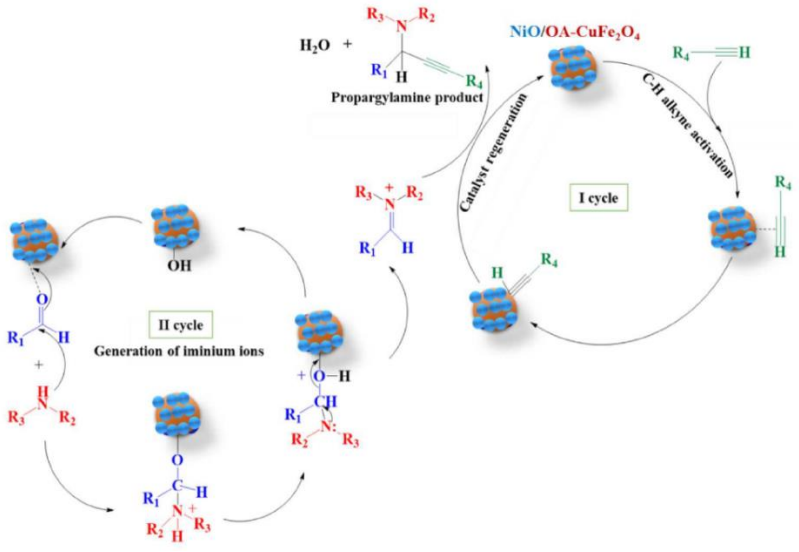

Figure 4.5. Reaction mechanism of $NiO/OA\text{-}CuFe_2O_4$ catalyzed A^3 coupling reaction. Reprinted with permission from ref. 38.

4.2 A^3 Coupling Reaction using Magnetic Catalysts

4.2.1 Introduction

Knowing the importance of propargylamines (A^3 coupling product) in medical, drug, and organic synthesis research, developing a facile way of making propargylamines becomes valuable to research and industry. By introducing TiO_2, magnetic Fe_2O_3, and their derivative catalysts into consideration brings a great potential of changing the reaction pathway from traditional thermal pathway into light irradiated, as well as the easy catalyst separation after reaction compared to regular homogeneous reactions.

In this part, magnetic Fe_2O_3 (mFe), magnetic Fe_2O_3@TiO_2 (mFeTi), black magnetic Fe_2O_3@TiO_2 (b-mFeTi), copper-doped magnetic Fe_2O_3@TiO_2 (mCuFeTi), and black copper-doped magnetic Fe_2O_3@TiO_2 (b-mCuFeTi) are tested for their catalytic properties in the aldehyde-alkyne-amine coupling reaction.

4.2.2 Experimental

4.2.2.1 Chemicals

Benzaldehyde, phenylacetylene, piperidine, and tert-butylbenzene were purchased from Sigma-Aldrich and used without any further purification. Acetonitrile (MeCN), dioxane, tetrahydrofuran (THF), and toluene were all HPLC grade.

4.2.2.2 Instrumentation

LedEngin light-emitting diodes (LED)(10W) centered at 369 nm and 465 nm were used as the irradiation source for reactions. A Thermal Scientific speed-and-temperature controllable stirring hot plate was used to perform thermal catalytic reactions. The concentrations of all reactants and products were measured on a GC-MS system with tert-butylbenzene as an external standard. GC-MS spectra were collected on an Agilent 6890-N Gas Chromatograph with an Agilent 5973 mass selective detector calibrated with acetophenone.

4.2.2.3 General Procedure of A^3 Coupling Reactions

The reactants were added sequentially as benzaldehyde (106 mg, 1 mmol), phenylacetylene (153 mg, 1.5 mmol), and piperidine (102 mg, 1.2 mmol) into 2 ml of

solvent (THF, dioxane, MeCN, water, or toluene) with a magnetic stir bar and 10 mg of catalyst. Then, the reaction vial was sealed and purged with argon for 8 minutes if needed (only for irradiation reactions, all thermal reactions are under air). For irradiation reactions, the reaction vial was irradiated by a 369 nm or a 465 nm LED with the irradiance of 2600 W/m^2, while vigorously stirred by a magnetic stirrer underneath and cooled down by compressed airflow for 5 hours. For thermal reactions, the reaction mixture was continuously stirred for 6 hours in a 120 °C sand bath, then naturally cooled down to room temperature for post-reaction processing.

After reaction, the catalysts in all reaction mixtures were simply separated using an external magnet. Concentrations of reactants and products were determined on the GC-MS system by mixing 20 μL of reaction liquid (for reaction in water, reaction mixture was extracted by 0.5 mL of ethyl acetate for 4 times (2 mL in total)) and 20 μL of tert-butylbenzene (10 mM in DCM) in 1 mL DCM.

4.2.2.4 Catalyst Amount Influence Test

20 mg, 10 mg, and 5 mg were selected as the amounts of catalyst to test the optimal usage of catalyst for the A^3 coupling reaction in toluene.

4.2.2.5 Kinetic Study

Reaction time of 1 h, 2 h, 3 h, 4 h, 6 h, 8 h, 12 h, 16 h, 20 h, and 24 h were chosen to analyze the kinetics of A^3 coupling reaction in dioxane. To minimize the error, reactions from 1h to 4h, 6 h to 12 h and 16 h to 24 h were performed in three different vials. For determining chemical concentrations, 100 μL of reaction mixture was taken out by a 1 mL syringe from the vial and processed following the steps in the general procedure.

4.2.2.6 Stability and Reusability Test of Catalysts

Recycling of the catalysts was simply done by removing them by applying an external magnetic field and washing with 2 mL of toluene for 3 times. The recycled catalysts were then dried under air before their second use. The reusability of the catalysts was tested for 3 cycles. After 3 cycles, the catalyst coated by gold was characterized using SEM and EDS mapping elemental mapping with carbon tape.

4.2.3 Results and Discussion

4.2.3.1 A^3 Coupling Reaction by Magnetic Catalyst

The general chemical equation of aldehyde-alkyne-amine coupling reaction from benzaldehyde, phenylacetylene, and piperidine is shown in Figure 4.6. First, three reactants couple together to form the desired A^3 coupling product and release water as a side product. If the reaction is allowed to proceed, the water molecules react with A^3 coupling product to produce chalcones, which is not what we want. Thus, the reaction time is very vital to this reaction. The kinetic study shows that the optimal reaction time is 6 h (details will be discussed in section 4.2.3.6), therefore all subsequent thermal A^3 coupling reactions were set to 6 h.

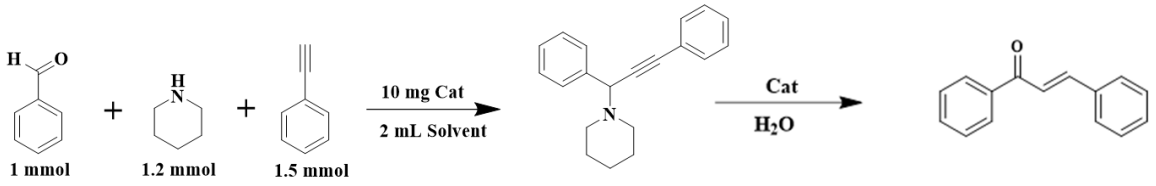

Figure 4.6. A^3 coupling reaction by magnetic catalysts, also showing the formation of chalcone if the reaction is allowed to react for a long time.

Benzaldehyde, phenylacetylene, A^3 coupling product, and chalcone can be easily quantified by GC-MS using tert-butylbenzene as an external standard. Piperidine cannot be monitored by GC-MS due to its instability, which can be proved by the strong ammonia smell when opening the reaction vial.

4.2.3.2 A^3 Coupling Reaction Using 369 nm and 465 nm Irradiations

The goal of combining black TiO_2 with magnetic Fe_2O_3 together is to let the reaction benefit from the light absorption of black TiO_2, and the magnetic separation as well as the visible-light absorption of magnetic Fe_2O_3. To investigate the light-induced A^3 coupling performance of b-mFeTi, mCuFeTi, and b-mCuFeTi in toluene and MeCN, reactions were performed under 369 nm or 465 nm LED irradiation and cooled by compressed air to terminate the influence of heat. All results are shown in Table 4.2.

Table 4.2. Results of light irradiation test for b-mFeTi, mCuFeTi, and b-mCuFeTi under different conditions.

Catalyst	Irradiation wavelength (nm)	Solvent	condition	A^3 Product %	Note
b-mFeTi	369	toluene	Ar	0	
b-mFeTi	369	toluene	air	0	
b-mFeTi	465	toluene	Ar	0	
b-mFeTi	465	toluene	air	0	
mCuFeTi	369	toluene	Ar	0	trace alkyne homocoupling
mCuFeTi	369	toluene	air	0	
mCuFeTi	369	MeCN	Ar	0	
mCuFeTi	369	MeCN	air	0	
mCuFeTi	465	toluene	Ar	0	trace alkyne homocoupling
mCuFeTi	465	toluene	air	0	
mCuFeTi	465	MeCN	Ar	0	
mCuFeTi	465	MeCN	air	0	
b-mCuFeTi	369	toluene	Ar	0	
b-mCuFeTi	369	toluene	air	0	
b-mCuFeTi	465	toluene	Ar	0	
b-mCuFeTi	465	toluene	air	0	

Unfortunately, Table 4.2 clearly shows that the chosen catalysts cannot work under 369 nm or 465 nm irradiation regardless of whether the systems are argon-purged or not. But interestingly, a trace of phenylacetylene homocoupling product was found in argon purged mCuFeTi catalyzed reaction mixture with both 369 nm and 465 nm irradiation. Copper as a great alkyne homocoupling catalyst has been reported in the literature[44-46], thus, it is not abnormal to find it in our reaction. Further experiments also found that phenylacetylene homocoupling product can only be observed with the addition of piperidine. The role of piperidine acts as a base to be proton acceptor. This is out of the scope of the chapter so it will not be discussed any further.

4.2.3.3 A^3 Coupling Reaction by Thermal Reaction Using Different Catalysts

Given that the light irradiation does not work in our A^3 coupling system, the traditional thermal reaction was also tested. In this section, three reactants were added in 2 mL of toluene for 6 hours at 120 °C with mFe, mFeTi, mCuFeTi, b-mFeTi, and b-mCuFeTi individually, or without any catalyst. Experimental results are tabulated in Table 4.3.

Table 4.3. A^3 coupling reaction results by using different catalyst in MeCN.

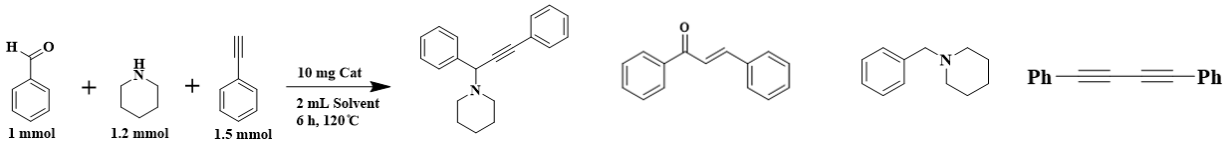

A B C D E F G

Catalyst	Conversion		Yield				
	A %	C %	D %	E %	F %	G %	Other product
No catalyst	54.5	21.7	0	0	trace	0	Many
mFe	43.4	19.5	0	0	trace	0	None
mFeTi	42.2	20.9	0	0	trace	0	None
b-mFeTi	40.6	17.7	0	0	trace	0	None
mCuFeTi	92.5	72.8	52.4	16.7	0	12.5	None
b-mCuFeTi	99.6	79.2	62.7	21.3	0	14.9	None

From Table 4.3, one obvious conclusion can be drawn as that the A^3 coupling reaction (product D) needs copper. Without copper, only trace amount of coupling product of benzaldehyde and piperidine (product F) can be found in the reaction mixture. Here, copper's affinity towards alkyne makes it a good dock for phenylacetylene to be adsorbed and activated on copper's surface waiting for reaction. It is also important to note that if no catalyst is added to the reaction, more than 5 products can be found in gas chromatography. But once iron is present in the system, all other side products are eliminated and only product F remains. All results illustrate the great importance of the existence of iron and copper in this reaction. But the role of TiO_2 in thermal A^3 coupling reaction still remains unclear.

Comparing all 6 entries in Table 4.2, b-mCuFeTi was selected as the best catalyst for our A^3 coupling reaction and used as the only catalyst for all subsequent experiments.

4.2.3.4 Solvent Optimization for A^3 Coupling Reaction Using b-mCuFeTi

THF, dioxane, MeCN, water, and toluene were chosen to be tested to find the most suitable solvent for thermal A^3 coupling reaction. As shown in Figure 4.7, in the perspective of reactant conversion, toluene, water and MeCN exhibit good benzaldehyde conversion. Water gives the best phenylacetylene conversion among all 5 solvents, followed by toluene as the second-best one. THF and dioxane both perform relatively poorly in the reactant conversion. Looking at product yields, toluene still shows great overall yield to every single product, while water, in contrast, gives nothing at all. An adequate yield can be found for MeCN, but it is not as good as that of toluene. Dioxane still shows poor yield towards products. THF, as the worst solvent in terms of percentage, yields pure A^3 coupling product after 6-hour reaction. It is easy to discover that yields are becoming poorer as the polarity of solvent increases, which shows that the A^3 coupling reaction favors nonpolar solvents.

By considering conversion, yield, and ease of reaction mixture process, toluene was selected as the best solvent for our A^3 coupling reaction and used as the only solvent for all subsequent experiments.

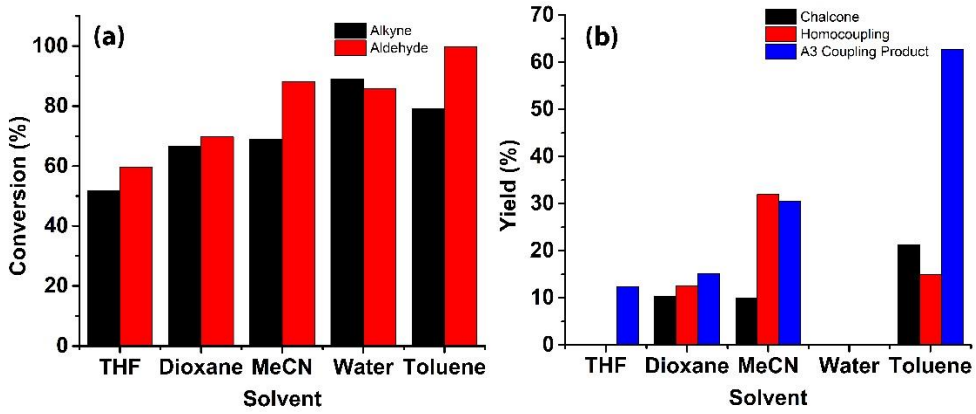

Figure 4.7. Conversions (a) and yields (b) of thermal A^3 coupling reaction with b-mCuFeTi in THF, dioxane, MeCN, water, and toluene after 6 hours at 120℃.

4.2.3.5 Optimization of Catalyst Amount

In the green chemistry's view, a desired reaction should be done using as few resources as possible. So, the catalyst amount also needs to be optimized. Here, by considering work done in published papers[47, 48], 5 mg, 10 mg, and 20 mg of b-mCuFeTi were tested in the A^3 coupling reaction.

In Figure 4.8, all three different amounts of catalyst exhibit near full conversion of benzaldehyde, while phenylacetylene conversion drops more from 10 mg to 5 mg than that from 20 mg to 10 mg. In terms of eliminating side reactions (phenylacetylene homocoupling reaction), 5 mg and 10 mg catalyst both are twice as good as 20 mg catalyst. In the meantime, 5 mg catalyst gives only half of chalcone as 10 mg and 20 mg do. For the yield of desired A^3 coupling product, 20 mg performs the best and 5 mg is the worst, but the differences between three individual are only around 7 percent.

Because the ease of magnetic separation and reusability of catalyst is also of importance to our catalyst, 10 mg was chosen as the optimal catalyst amount instead of 5 mg. Furthermore, the reaction only requires 10 mg of our catalyst comparing to 50 mg for Marzieh's[38], which shows the better activity of b-mCuFeTi catalyst.

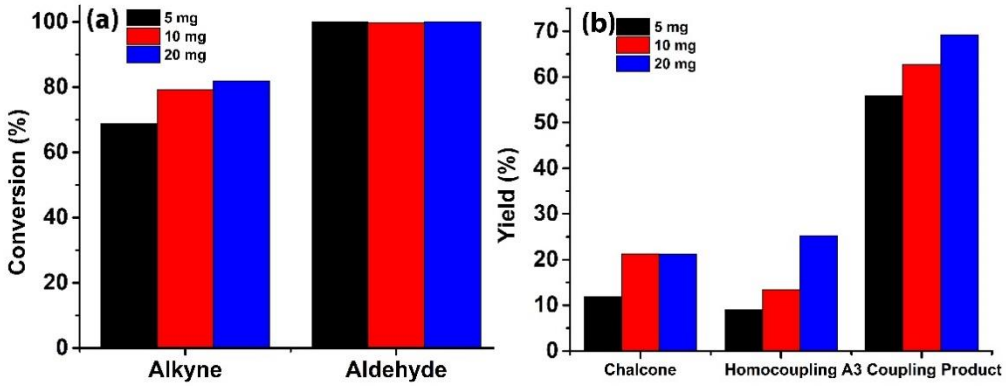

Figure 4.8. The conversions (a) and yields (b) of thermal A^3 coupling reaction in toluene with 5 mg, 10 mg, or 20 mg b-mCuFeTi after 6 hours at 120℃.

4.2.3.6 Kinetic Study

As discussed in section 4.2.3.1, the A^3 coupling product can be hydrolyzed and turned into chalcone if the reaction time is too long, it is crucial to obtain the kinetics of our A^3 coupling reaction in order to maximize the yield of the A^3 coupling product. The conversions and yields were calculated after the reaction time of 0, 1, 2, 3, 4, 6, 8, 12, 16 20, and 24 hours. Figure 4.9 shows that as heating starts, the A^3 coupling product already started forming. More than 94 percent of benzaldehyde and 68 percent of phenylacetylene were consumed within first 4 hours. Meanwhile, the yield of phenylacetylene homocoupling also got 13.8 percent and only slightly increased after 4 hours. The yield of

A^3 coupling product reached the peak of 62.7 percent at 6 hour and started dropping after 6 hours. The benzaldehyde was also fully reacted after 6 hours. Chalcone appeared after 2-hour reaction and increased with the increase of A^3 coupling product. It is important to note that after 6 hours, when the benzaldehyde was used out, the concentration of A^3 coupling product started dropping at the same speed as the chalcone product increases. The yields finally reached 9 and 71 percent for A^3 coupling product and chalcone, respectively. This indicates that A^3 coupling product was only hydrolyzed into chalcone other than any other product. The conversion of phenylacetylene and yield of its homocoupling was also interestingly increasing following the same pattern after 6 hours, which again shows that the optimal reaction time is 6 hours.

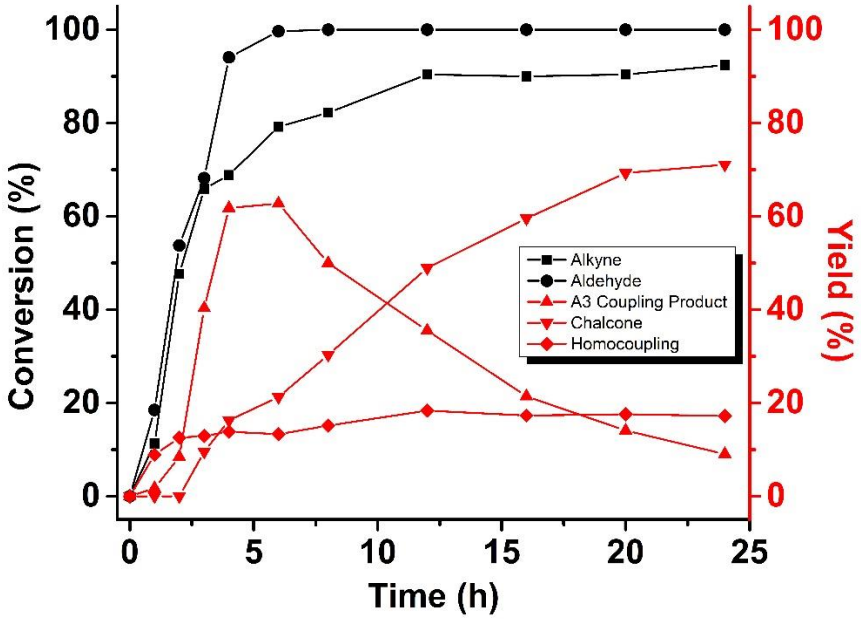

Figure 4.9. Kinetics of A^3 coupling reaction in toluene with 10 mg b-mCuFeTi at 120 °C from 0 to 24 hours.

4.2.3.7 Stability and Reusability of b-mCuFeTi in A^3 Coupling Reaction

To evaluate the stability and reusability of b-mCuFeTi, SEM and EDS elemental mapping were applied to determine the change of morphology and element composition of the catalyst after 3 catalytic cycles. Conversions and yields were also calculated and plotted in 3 catalytic cycles for A^3 coupling reaction.

Figure 4.10 shows the SEM images comparing b-mCuFeTi before and after 3 catalytic cycles. From Figure 4.10 (a) and (b), the chunky structure remains after 3 reaction

cycles. Small TiO_2 aggregates can also be found in (c) and (d). This evidence shows the good structural stability of b-mCuFeTi. On the other hand, the EDS elemental mapping shown in Figure 4.11 does not include any copper peak in three different selected areas, which indicates that most copper was leached out during these 3 catalytic cycles. This proves that the chemical stability of b-mCuFeTi still needs to be improved.

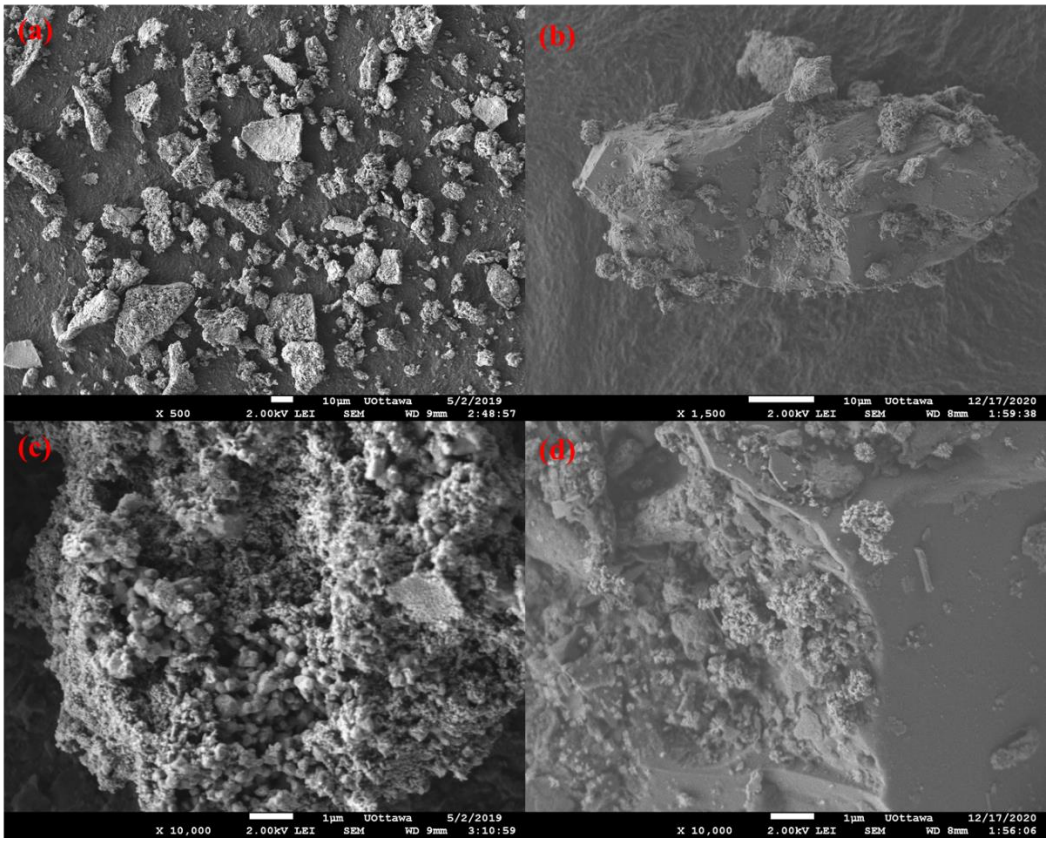

Figure 4.10. The SEM imagines of b-mCuFeTi before (a and c) and after (b and d) 3 catalytic cycles.

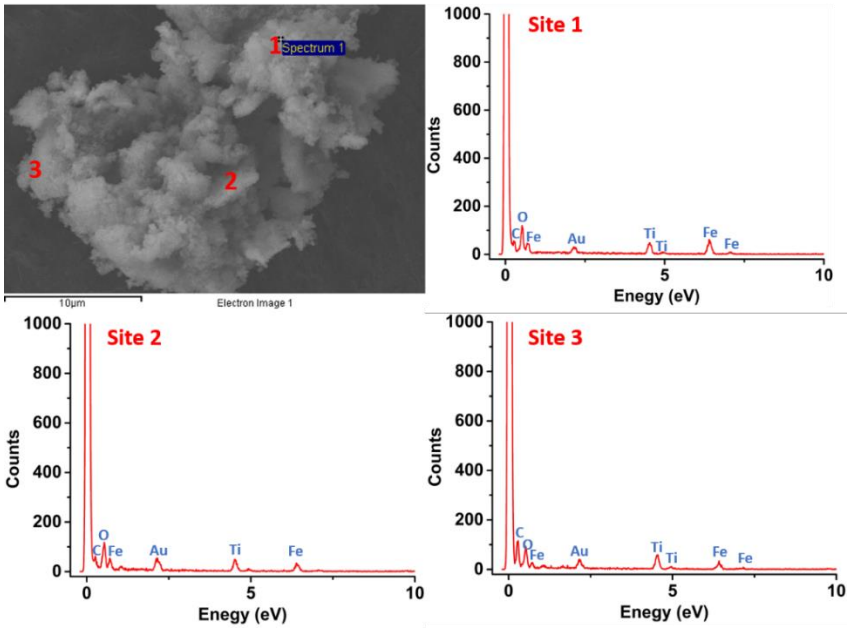

Figure 4.11. The EDS elemental mapping of b-mCuFeTi after 3 catalytic cycles.

The conversions and yields in Figure 4.12 visually show the performance of b-mCuFeTi in three catalytic cycles. From Figure.12 (a), only a small decrease in benzaldehyde's conversion can be observed, while phenylacetylene's conversion dropped around 15 percent. A similar drop can also be found in Figure.12 (b). the yields of two products related to phenylacetylene both decrease a lot after 3 catalytic cycles. The yield of chalcone is not influenced much because of the abundance of A^3 coupling product at 6 hours. All results indicate that b-mCuFeTi has good structural stability but poor chemical stability of copper in the catalyst.

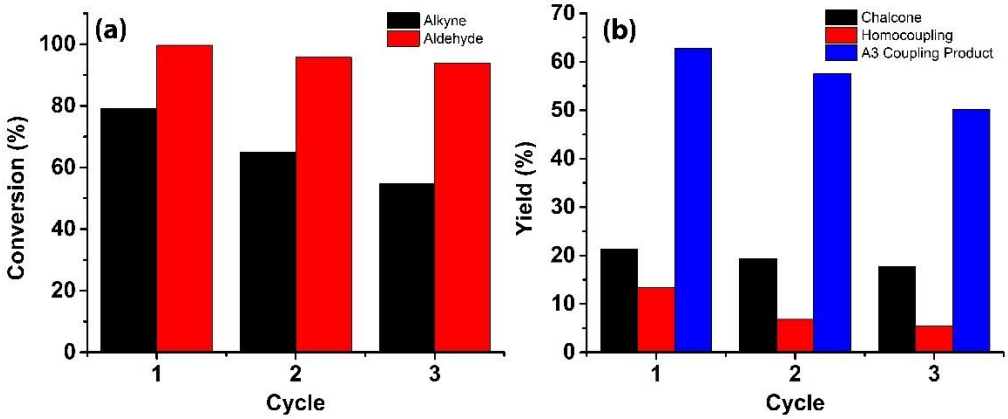

Figure 4.12. The conversions (a) and yields (b) of thermal A^3 coupling reaction in toluene 10 mg of b-mCuFeTi in 3 catalytic cycles.

4.2.3.8 Mechanism of b-mCuFeTi catalyzed A^3 Coupling Reaction

Based on fundamental organic chemistry knowledge and mechanisms hypothesized in other literature, the mechanism of our b-mCuFeTi catalyzed A^3 coupling reaction was illustrated in Figure 4.13. Phenylacetylene molecules are first attracted and docked onto the surface of the catalyst to form π-alkyne-metal complexes to activate the C-H bond. Then, the activated C-H bonds in π-alkyne-metal complexes break into copper-acetylides and protons, which are further abstracted by piperidine molecules. Now, benzaldehyde molecules react with piperidine ions to produce the key intermediate iminium ions and release H_2O as side product. Finally, the iminium intermediates and copper-acetylides subsequently undergo a nucleophilic addition pathway to form the final product propargylamine and regenerate the catalyst for the next catalytic cycle.

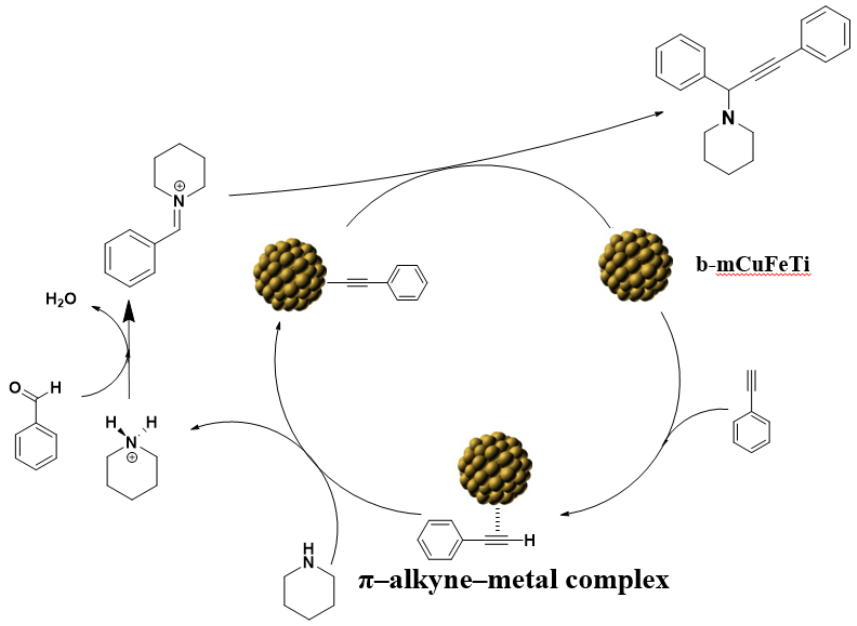

Figure 4.13. Reaction mechanism of b-mCuFeTi catalyzed A^3 coupling reaction.

4.2.4 Conclusion

In this part, the A^3 coupling reaction in our experimental system was found that it only works through the traditional thermal route, and not the 369-nm or 465-nm irradiation pathway with mCuFeTi and b-mCuFeTi. The catalyst screening indicates the importance of iron and copper existence in the A^3 coupling reaction. The A^3 coupling product is not the only product in the reaction, it can be hydrolyzed into chalcone as the reaction continues. Meanwhile, phenylacetylene also formed its homocoupling product. To optimize the A^3

coupling reaction, the best solvent is determined as the least polar solvent – toluene, and the optimal catalyst amount is 10 mg. The kinetic study also gives us the best reaction duration as 6 hours. The SEM, EDS elemental mapping, and reusability test all shows the good structural and poor copper stability of b-mCuFeTi.

Reference

1. Gawande, M. B.; Monga, Y.; Zboril, R.; Sharma, R. K. *Coordination Chemistry Reviews* **2015,** 288, 118-143.

2. Zhang, M.; Lu, J.; Zhang, J.-N.; Zhang, Z.-H. *Catalysis Communications* **2016,** 78, 26-32.

3. Maleki, B.; Reiser, O.; Esmaeilnezhad, E.; Choi, H. J. *Polyhedron* **2019,** 162, 129-141.

4. Patil, A.; Ganguly, S.; Surana, S. *Journal of Chemical Sciences* **2010,** 122, (3), 443-450.

5. Kazemi, M.; Shiri, L.; Kohzadi, H. *Phosphorus, Sulfur, and Silicon and the Related Elements* **2015,** 190, (9), 1398-1409.

6. Kazemi, M.; Shiri, L.; Kohzadi, H. *Phosphorus, Sulfur, and Silicon and the Related Elements* **2015,** 190, (7), 978-1003.

7. Kazemi, M. *Synthetic Communications* **2020,** 50, (14), 2114-2131.

8. Abedi, M.; Hosseini, M.; Arabmarkadeh, A.; Kazemi, M. *Synthetic Communications* **2021,** 51, (6), 835-855.

9. Boulton, A. A.; Davis, B. A.; Durden, D. A.; Dyck, L. E.; Juorio, A. V.; Li, X.-M.; Paterson, I. A.; Yu, P. H. *Drug Development Research* **1997,** 42, (3‐4), 150-156.

10. Zindo, F. T.; Joubert, J.; Malan, S. F. *Future Medicinal Chemistry* **2015,** 7, (5), 609-629.

11. Marco-Contelles, J.; Unzeta, M.; Bolea, I.; Esteban, G.; Ramsay, R. R.; Romero, A.; Martínez-Murillo, R.; Carreiras, M. C.; Ismaili, L. *Frontiers in Neuroscience* **2016,** 10, (294).

12. Bar-Am, O.; Amit, T.; Weinreb, O.; Youdim, M. B. H.; Mandel, S. *Journal of Alzheimer's Disease* **2010,** 21, 361-371.

13. Ermolat'ev, D. S.; Bariwal, J. B.; Steenackers, H. P. L.; De Keersmaecker, S. C. J.; Van der Eycken, E. V. *Angewandte Chemie International Edition* **2010,** 49, (49), 9465-9468.

14. Arshadi, S.; Vessally, E.; Edjlali, L.; Hosseinzadeh-Khanmiri, R.; Ghorbani-Kalhor, E. *Beilstein Journal of Organic Chemistry* **2017,** 13, 625-638.

15. Zhao, X.-B.; Ha, W.; Jiang, K.; Chen, J.; Yang, J.-L.; Shi, Y.-P. *Green Chemistry* **2017,** 19, (5), 1399-1406.

16. Ghosh, S.; Biswas, K. *RSC Advances* **2021,** 11, (4), 2047-2065.

17. Feng, H.; Peng, F.; Xi, H.; Zhong, L.; Huang, L. *Asian Journal of Organic Chemistry* **2021**, 4, (10), 762-765.

18. Singha, R.; Brahman, D.; Sinha, B.; Ghosh, P. *Asian Journal of Green Chemistry* **2021,** 5, (1), 91-110.

19. Sampani, S. I.; Zdorichenko, V.; Devonport, J.; Rossini, G.; Leech, M. C.; Lam, K.; Cox, B.; Abdul-Sada, A.; Vargas, A.; Kostakis, G. E. *Chemistry – A European Journal* **2021,** 27, (13), 4394-4400.

20. Thakur, K.; Khare, N. K. *Carbohydrate Research* **2020,** 494, 108053.

21. Ongaro, A.; Ribaudo, G.; Zagotto, G.; Memo, M.; Gianoncelli, A. *ChemistrySelect* **2019,** 4, (45), 13138-13142.

22. Wang, F.; Feng, H.; Li, H.; Miao, T.; Cao, T.; Zhang, M. *Chinese Chemical Letters* **2020,** 31, (6), 1558-1563.

23. Jesin, I.; Nandi, G. C. *European Journal of Organic Chemistry* **2019,** 2019, (16), 2704-2720.

24. Lu, Y.; Johnstone, T. C.; Arndtsen, B. A. *Journal of the American Chemical Society* **2009,** 131, (32), 11284-11285.

25. Mao, F.; Li, J.; Wei, H.; Huang, L.; Li, X. *Journal of enzyme inhibition and medicinal chemistry* **2015,** 30, (6), 995-1001.

26. Kopka, I. E.; Fataftah, Z. A.; Rathke, M. W. *The Journal of Organic Chemistry* **1980,** 45, (23), 4616-4622.

27. Hennion, G. F.; Hanzel, R. S. *Journal of the American Chemical Society* **1960,** 82, (18), 4908-4912.

28. Czernecki, S.; Valéry, J.-M. *Journal of Carbohydrate Chemistry* **1990,** 9, (5), 767-770.

29. Takano, S.; Kochi, T.; Kakiuchi, F. *Chemistry Letters* **2017,** 46, (11), 1620-1623.

30. Peshkov, V. A.; Pereshivko, O. P.; Van der Eycken, E. V. *Chemical Society Reviews* **2012,** 41, (10), 3790-3807.

31. Lauder, K.; Toscani, A.; Scalacci, N.; Castagnolo, D. *Chemical Reviews* **2017,** 117, (24), 14091-14200.

32. Yoo, W.-J.; Zhao, L.; Li, C. *ChemInform* **2012,** 43.

33. Wei, C.; Li, C.-J. *Journal of the American Chemical Society* **2002,** 124, (20), 5638-5639.

34. Wei, C.; Mague, J. T.; Li, C.-J. *Proceedings of the National Academy of Sciences of the United States of America* **2004,** 101, (16), 5749-5754.

35. Zhang, J.-Y.; Huang, X.; Shen, Q.-Y.; Wang, J.-Y.; Song, G.-H. *Chinese Chemical Letters* **2018,** 29, (1), 197-200.

36. Amini, M.; Kafshdouzsani, M. H.; Akbari, A.; Gautam, S.; Shim, C.-H.; Chae, K. H. *Applied Organometallic Chemistry* **2018,** 32, (9), e4470.

37. Gajengi, A. L.; Sasaki, T.; Bhanage, B. M. *Catalysis Communications* **2015,** 72, 174-179.

38. Daryanavard, M.; Ataei, A.; Sheykhabadi, P. G.; Rafiee, E.; Joshaghani, M. *ChemistrySelect* **2020,** 5, (1), 18-27.

39. Sreedhar, B.; Kumar, A. S.; Reddy, P. S. *Tetrahedron Letters* **2010,** 51, (14), 1891-1895.

40. Feng, H.; Jia, H.; Sun, Z. *Advanced Synthesis & Catalysis* **2015,** 357, (11), 2447-2452.

41. Safaei-Ghomi, J.; Nazemzadeh, S. H.; Shahbazi-Alavi, H. *Main Group Metal Chemistry* **2017,** 40, (5-6), 129-135.

42. Li, C.-J.; Wei, C. *Chemical Communications* **2002**, (3), 268-269.

43. Koradin, C.; Polborn, K.; Knochel, P. *Angewandte Chemie International Edition* **2002,** 41, (14), 2535-2538.

44. Yin, C.; Liu, S.; Qin, Z.; Zhang, Y.; Li, G.; Zhao, Z. *European Journal of Inorganic Chemistry* **2021,** 2021, (4), 392-397.

45. Holganza, M. K.; Trigoura, L.; Elfarra, S.; Seo, Y.; Oiler, J.; Xing, Y. *Tetrahedron Letters* **2019,** 60, (17), 1179-1181.

46. Sgrolli, N.; Imlyhen, N.; Volkman, J.; Raspolli-Galletti, A. M.; Serp, P. *Molecular Catalysis* **2017,** 438, 143-151.

47. Mohamed, A.; Nasser, W. S.; Kamel, B. M.; Hashem, T. *European Polymer Journal* **2019,** 113, 192-196.

48. Hainer, A.; Marina, N.; Rincon, S.; Costa, P.; Lanterna, A. E.; Scaiano, J. C. *Journal of the American Chemical Society* **2019,** 141, (11), 4531-4535.

Chapter 5
Future Research and Perspectives

In chapter 3, the experimental results show that although black TiO_2 catalysts are able to absorb visible light, the decarboxylation reactions can only proceed under UV light, and the Degussa P25 work better than their black counterparts. The reason is explained as the deficiency of hole generation, which is due to the oxidation of Ti^{3+} species to Ti^{4+} under light irradiation. It indicates that reactions involving positive holes are not favorable while using black TiO_2 catalysts. But the light-induced electrons are still open for future study and utilization. In our group, Sara has successfully synthesized black TiO_2 strips from white ones by using the same blackening treatment. Strips with 6-cm and 20-cm length are shown in the Figure 5.1 (a) and (b). The desired black color can be seen in the 6-cm strips, but only part of 20-cm strip turned into black. The synthesized black TiO_2 strips were also functional in degradation methylene blue in the flow system shown in Figure 5.1 (c) under visible light irradiation.

For example, the reductive photodegradation of contaminants (such as the test methylene blue) using anatase or rutile black TiO_2 can be evaluated. Black TiO_2 catalysts still have the possibility to lead to sunlight potential application for water treatment in the future.

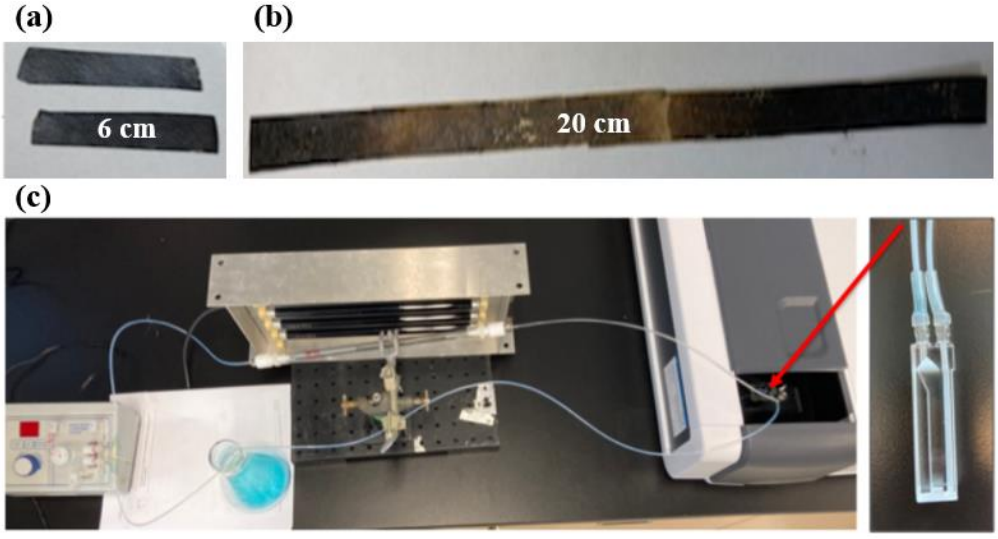

Figure 5.1. The photographs of the synthesized 6-cm (a) and 20-cm (b) black TiO_2strips, and the flow reaction system for methylene blue degradation (c) by Sara.

Chapter 4 shows the catalytic capabilities of b-mCuFeTi catalyst in A^3 coupling reaction. But there is also more room for evaluation and improvement. Especially, the roles of TiO_2 in the reaction, the influence of Cu mole ratio in the catalyst and the enhancement of stability of the catalyst are still worth examining.

Considering combining improving the ease of catalyst separation and expanding light source utilization, new kinds of supports for black TiO_2 are worthy to be tested or synthesized. Our group has broad experience in various of reactions using TiO_2 on different supports. Replacing regular TiO_2 with black TiO_2 on known supports might be a good and facile way of improving catalytic abilities. Also, new kinds of supports such as magnetic Fe_3O_4@SiO_2 core-shell nanoparticles that have great potential acting as a universal magnetic-functional support, may be more valuable materials. Soheil and colleagues successfully prepared TiO_2/SiO_2/Fe_3O_4 nanoparticles for the removal of Cd(II), Hg(II), and Ni(II) in water[1]. The magnetic core was made by coprecipitation from ferric chloride, ferrous chloride, and ammonia solution under ultrasonication instead of magnetic stirring. Then, the SiO_2 shell was grown onto Fe_3O_4 particles by dropwisely adding tetraethyl orthosilicate into the mixture of magnetic cores, EtOH and ammonia under ultrasonication. Finally, the TiO_2 nanoparticles were synthesized from titanium butoxide. The corresponding TEM images are shown in Figure 5.2. Comparing Figure 5.2 (a) and (b), a 3-nm SiO_2 shell can be clearly seen on the 70-nm Fe_3O_4 cores. Meanwhile, the 9-nm TiO_2 shell is also able to be observed after TiO_2 deposition. It is really interesting to test if this material can be blackened by the method we developed in this thesis. By varying the phase and morphology of TiO_2 on this magnetic support, many other potential catalysts might be discovered and synthesized.

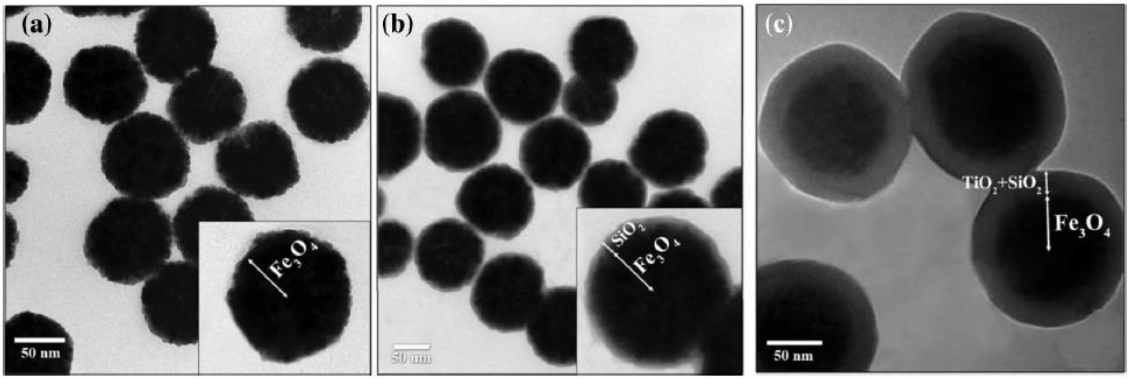

Figure 5.2. TEM images of Fe_3O_4 (a), SiO_2/Fe_3O_4 (b) and TiO_2/SiO_2/Fe_3O_4 nanoparticles (c)[1]. Reprinted with permission from ref. 1.

Reference

1. Sobhanardakani, S.; Zandipak, R. Clean Technologies and Environmental Policy **2017**, 19, (7), 1913-1925.